Associations of White Matter Microstructure to Memory Processes: Insights for Neuroplasticity and Cognitive Decline

By

Austin M. Bazydlo

A dissertation submitted in partial fulfillment of the requirements for the degree of

Doctor of Philosophy

(Medical Physics)

at the

UNIVERSITY OF WISCONSIN-MADISON 2021

Date of final oral examination: 6/4/2021

The dissertation is approved by the following members of the Final Oral Committee:

Andrew L. Alexander, Professor, Medical Physics and Psychiatry

Rasmus Birn, Professor, Psychiatry

Bradley T. Christian, Professor, Medical Physics and Psychiatry

C. Shawn Green, Associate Professor, Psychology

Barbara B. Bendlin, Associate Professor, Alzheimer's Disease Research Center

Nagesh Adluru, Associate Scientist, Waisman Center Brain Imaging Core

The Road goes ever on and on

Out from the door where it began.

Now far ahead the Road has gone,

Let others follow it who can!

Let them a journey new begin,

But I at last with weary feet

Will turn towards the lighted inn,

My evening-rest and sleep to meet.

-*Bilbo Baggins upon the Hobbits' return to Rivendell following the War of the Ring*

J. R. R. Tolkien

Dedication and Acknowledgements

I don't know that anyone will ever read this section and that is okay. Much of the writing process of a dissertation is reflective and deeply personal, doing so in the worst pandemic in 100 years has made this even more insular and pensive. Moreover, quarantine has made for a long, slow goodbye to my time at UW – like a period drawn with a heavy hand at the end of a chapter. Naturally, this has given me time to reflect on my journey and the events of my life that have led to this point.

To prosper in a world that was not made for you, is to be like a seed cast on rocks that takes root. The wind is bitter; the rain is cold; the sun hot and unforgiving; the water and comforts scarce; and many of your friends don't make it. Despite the odds, you hang on. Your roots twist and contort to find a grip and you become a grotesque form between rock and tree, born of necessity and conformity to the fate dealt to you. Your bark becomes thick, hardened, and gray. But time wears on and, slowly, by luck or divine providence, the world changes around you to be a little gentler. The time comes to take stock and prune the thick hide and extraneous branches that no longer serve or define you – a time to discover and nurture the real you that was buried so long ago.

Grad school has been this time of healing for me, although it did not take the form I expected. I began this journey on a promise I made to an Austin from a far more disparaging time in my life, who sought escape from burdens too big for him to understand in the wonder that books of science, art, and far off lands could provide. Much of my life has followed this trend – placing my hopes in the promise of books and science that things would get better. If I could make it down this path, I might finally find freedom. This work of some 120 pages, roughly 300 credits of coursework, my publications, too many late labs and all-nighters, and some million cups of coffee

are me making good on this promise. *We made it*. And the peace I found on the other side is far greater than I ever imagined.

My greatest supporters, loudest critics, most loyal friends, and greatest comfort are my corgis, Charlie and Hashbrown, who have been a greater support to me than they will ever comprehend. Charlie came into my life in one of its darkest chapters and brought me the peace and strength to keep going. I think Charlie knew that he had a second dad (Dad 2) he had to find, and thank goodness for both of us, he did. Joe, my best friend and husband, has been my rock, inspiration, and catalyst for self-discovery and healing to love myself, which is a gift I will spend the rest of my life trying to repay. Love got us through our first chapter, and I can't wait to see what the next one holds.

Joe came as part of a box set, which I loved so much that I took their name as my own. Busia, Ken, Chris, Kenny, Sarah, Jack, and Grant, you are the family I needed but never expected. Your unfaltering support, boundless love, and encouragement have seen Joe and I through our hardest moments and you have celebrated our triumphs louder than anyone. I truly could not have done this without you.

I am so grateful for my mother, Dr. Beth Patrick, a first-generation college student and single mother who sacrificed and worked tirelessly to make a better life for us. It is her example of hard work and determination that showed me that anything is possible and her scientific acumen that first instilled within me a love for science and knowing things. I am eternally grateful for her love and support, as well as that of my grandparents, Maw and Paw, who have always encouraged me and beamed with pride each step of the way. I love you.

I could not have done this without the support of my lifelong friends, Roan and Isaac. Our constant laughter and coffee breaks gave me the peace to face the next day. I am also grateful to

my friends here in Madison who I will value forever for their kindness and support. Jason and Katie Moody, Ben and Ashlee Yeske, Jose Guerrero, Autumn Walter, Matt Zammit, Lindsay Bodart, Leah Turner, and Nagesh and Anusha Adluru thank you for being a part of this journey.

Knowing science and being a scientist are very different things, and I did not come by the latter naturally. I am especially grateful to my advisor, Dr. Andy Alexander, who had the patience and grace to allow me to learn to be a scientist in my own way, but the mentorship and direction to see that I finished. Thank you for allowing me this opportunity that has permanently shaped my life and I have so enjoyed. I am also thankful for my mentors and collaborators who have given me so much insight and made me a better scientist. Thank you, Doug Dean, Nagesh Adluru, Steve Kecskemeti, Brad Christian, Shawn Green, Rasmus Birn, Greg Kirk, Sigan Hartley, and Barb Bendlin.

Thank you to NIH and the UW T32 Radiological Sciences Training Grant for my funding sources.

In memory of Ross Luo and Dr. Edward Jackson, far greater scientists than I will ever be and gone far too soon.

Abstract

Diffusion-based magnetic resonance imaging (dMRI) methods have rapidly gained popularity for both diagnostic and research purposes since their advent in the early 1990s. Advances in hardware and analysis infrastructure have greatly accelerated the advent of ever more advanced models and applications of diffusion imaging. The sensitivity of diffusion imaging to small changes of the movement of water within the brain has made it the mainstay for imaging the restricted movement of water in white matter.

Learning and memory are essential parts of the human experience and key to our survival. To this end, research is actively ongoing to study these phenomena in the near fully matured brain and in the declining brain. Recent studies have shown cross-sectional diffusion MRI indications of neuroplastic response in a variety of tasks, including juggling, learning an instrument, and playing video games; however, none of these studies have provided both short-term and long-term changes, nor have they tested the ability of dMRI to discriminate between task-related changes. In this work, the ability of dMRI to detect both short-term and long-term brain changes in a cohort of young adults playing either *Guitar Hero* or *Need-for-Speed* was tested, as well as microstructural differences between the two video games.

In contrast to the evolving adult brain, it is important to understand the microstructure of the declining brain and its effects on cognitive ability. A key population to study is aging adults with Down syndrome (DS) brain which, due to trisomy of the 21st chromosome, experience early and elevated amounts of amyloid accumulation and increased Alzheimer's dementia (AD) prevalence. To provide a wholistic understanding of WM microstructure in adult DS, this work explores differences of microstructure between adults with DS with and without significant

amyloid accumulation, as well as the relationship of WM microstructure to episodic memory performance.

1. Dissertation Objectives and Outline

The goal of this dissertation is to provide insights into the evolution and degradation of brain microstructure and the resulting changes to memory and cognition. This goal is achieved using microstructural magnetic resonance imaging (MRI) of two populations: 1) adults with Down syndrome (DS) who are at a heightened risk of developing Alzheimer's Disease and 2) typically developing adults subjected to a videogame training battery. This work aims to provide meaningful imaging biomarkers for DS populations and to bridge the DS-AD imaging and cognitive literature. Further, this work seeks to further understand the suitability and sensitivity of MRI to detect neuroplastic processes in the adult brain.

Chapter 2 of this work provides the physical background of the imaging techniques employed. Particular emphasis is placed on the diffusion process and its contribution to signal evolution in MRI, as well as the nuclear magnetic resonance phenomenon, the Bloch and Bloch Torrey Equations, the spin-echo experiment, and the Stejskal-Tanner Equation. The diffusion tensor imaging (DTI) and neurite orientation dispersion and density imaging (NODDI) models are derived, and practical model fitting techniques are explored. Common artifacts observed in diffusion MRI and practical means to mitigate their effects are discussed. Chapter 2 concludes with a discussion of R1 relaxometry, which is known to be sensitive to myelin content in the brain, although, other factors like iron content and axonal packing may also affect R1.

Chapter 3 presents the neuroanatomical, physiological, and pathophysiological processes of concern to this work. A summary of white matter anatomy and physiology is presented, with particular emphasis on function and organization. The degenerative processes and pathophysiological hallmarks of dementia and DS are also discussed, as well as current findings

in DS and AD imaging literature. A discussion of physiological underpinnings of neuroplasticity and an imaging literature review are also presented in Chapter 3.

Chapters 4 and 5 are derived from data collected as part of the Alzheimer's Biomarkers Consortium – Down syndrome (ABC-DS) study, which is a multi-site study of imaging, CSF, and cognitive biomarkers in the aging DS population. People with DS are at an increased risk of developing and AD and typically at an early age. For these reasons, DS populations are particularly insightful for studying the physiological and neuroanatomical processes occurring in preclinical AD. Chapter 4 explores the relationship between diffusion MRI measures of white matter microstructure with a global amyloid-β measure derived using [^{11}C] Pittsburgh Compound-B positron emission tomography and provides evidence for a possible link between amyloid burden and white matter neurodegeneration. Chapter 5 explores the relationship between white matter microstructure and episodic memory performance and serves as a link between imaging and cognitive findings in the DS-AD literature.

Chapter 6 explores the evolution of brain microstructure, as opposed to the degenerative processes explored in Chapters 4 and 5. Chapter 6 exams the sensitivity of diffusion MRI methods and R1 relaxometry to microstructural brain changes evoked using repeated video game training. These microstructural changes are thought to be related to neuroplasticity, which is the brain's ability to produce, prune, and reinforce connections to optimize task performance or comprehension. Active learning participants played either *Guitar Hero* (GH) or *Need for Speed* (NFS). The GH task targeted motor planning areas by never repeating a song within a training session, thus requiring participants to continuously adapt. NFS participants, on the other hand, performed the same task on the same virtual map during each training session to target spatial-route learning.

The findings of Chapters 4, 5, and 6 are summarized in Chapter 7. Chapter 7 addresses possible limitations and confounds specific to imaging DS populations and brain plasticity, as well as brain imaging as a whole. Future directions for the presented work are also discussed in Chapter 7.

2. Physical Background

2.1. Brownian Motion and the Diffusion Process

This work largely focuses on imaging methods reliant on the principle of diffusion and requires a step back to the quantum mechanical *Gold Rush* of the early 20th century. Though descriptions of the phenomenon that would become known as Brownian motion predate its namesake, Robert Brown is commonly credited with the process' discovery. Brown, a botanist, observed in 1827 that pollen in water ejected tiny particles from the grains that moved completely at random (Brown, 1828). Brown repeated his experiment with inorganic matter and observed the same motion, thus ruling out the motion as a life-driven process, yet he could not derive an explanation for the cause of such motion. An answer would not be provided for almost one hundred years.

The telling of the quantum story of diffusion begins long before the writing of this manuscript, beginning with Einstein's description of particles moving via Brownian motion in 1905. Published originally in German as *Über die von der molekularkinetischen Theorie der Wärme geforderte Bewegung von in ruhenden Flüssigkeiten suspendierten Teilchen* and published in English in 1956 (Einstein, 1905; Einstein et al., 2006). Einstein (1905) posited that Brownian particles moved in a stochastic manor, i.e., a random walk, where the net displacement (mean squared displacement) was related to a diffusion coefficient. Figure 1A shows the path taken by a particle over three walks with net displacement, $\vec{r}$. Figure 1B shows walks of three

different diffusion times, τ, and the linear relationship of the mean squared displacement and the diffusion time.

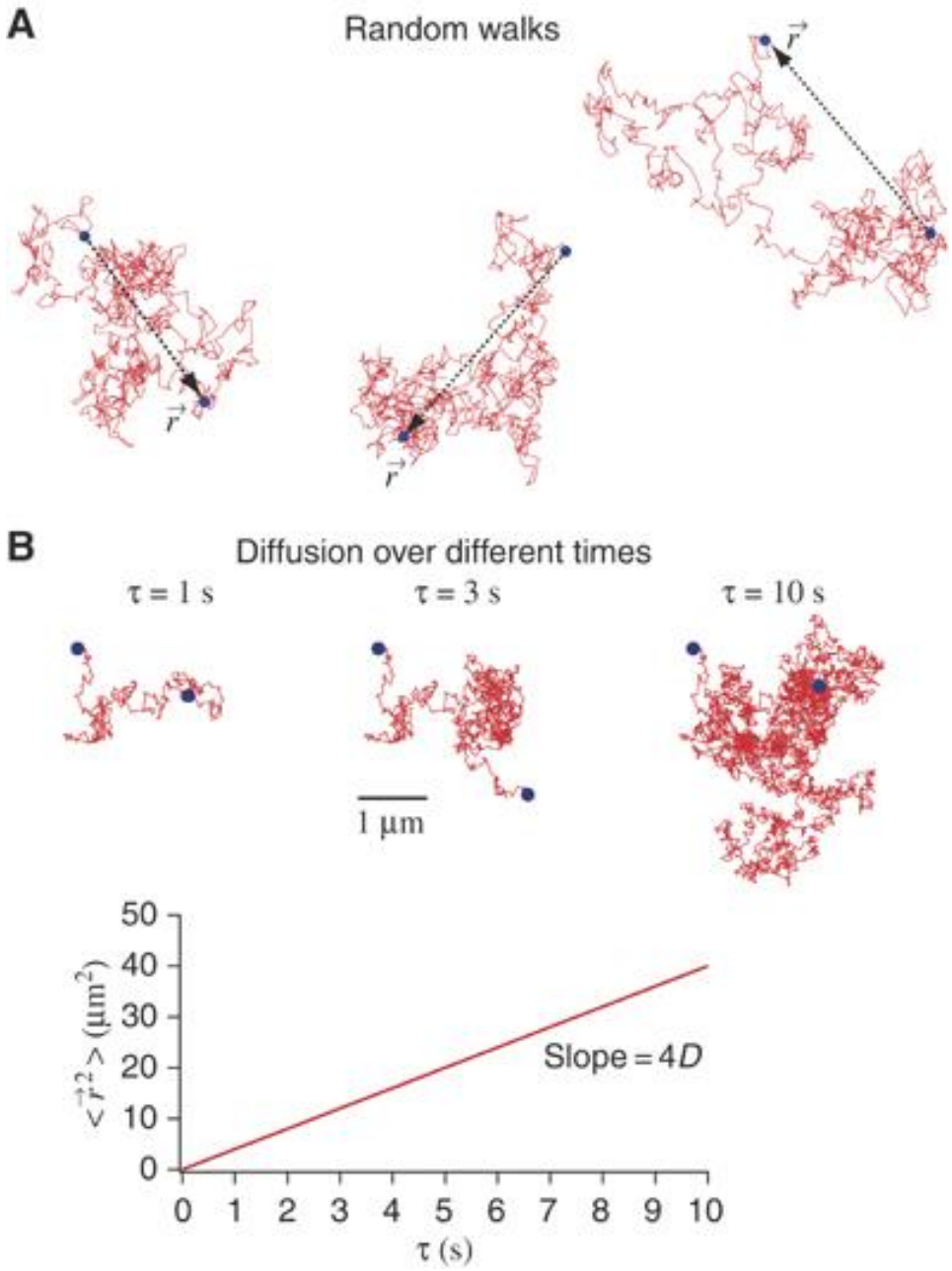

Figure 1: Brownian motion and diffusion. (A) Molecules undergo random-walk motion owing to collisions with solvent molecules during a time interval τ, we will see that it is displaced by a position vector. (B) The three pictures show the trajectory of a molecule having a diffusion coefficient D=1 µm2 s−1 during various time intervals. Reprinted with permission from Marguet, D., Lenne, P.-F., Rigneault, H., & He, H.-T. (2006). Dynamics in the plasma membrane: how to combine fluidity and order. The EMBO Journal, 25(15), 3446-3457.

Einstein went on to relate the diffusion coefficient to measurable physical quantities. Einstein imagined the random displacement, Δ, was governed by some probability distribution $\phi(\Delta)$. Assuming conservation of particle number, Einstein was able to express the number of particles per unit volume [*f(x,t)*] at time $t + \tau$ lying between a small space spanning from *x* to *x+dx* (a small distance) using a Taylor series:

$$f(x, t+\tau)dx = dx \int_{-\infty}^{\infty} f(x+\Delta)\phi(\Delta)\, d\Delta \qquad \text{Eq. 1}$$

Since τ is small, *f(x,t+τ)* is simply:

$$f(x, t+\tau) = f(x,t) + \tau \frac{\partial f}{\partial t} \qquad \text{Eq. 2}$$

f(x+Δ, t) can be expressed using a Taylor series:

$$f(\mathrm{x}+\Delta, \mathrm{t}) = f(\mathrm{x}, \mathrm{t}) + \Delta \frac{\partial f(\mathrm{x})}{\partial \mathrm{x}} + \cdots + \frac{\Delta^n \partial^{\mathrm{n}} f(\mathrm{x})}{\mathrm{n}!\, \partial \mathrm{x}^{\mathrm{n}}} \ldots \qquad \text{Eq. 3}$$

Thus,

$$f(x,t) + \tau \frac{\partial f}{\partial t} = f(x,t) \int_{-\infty}^{\infty} \phi(\Delta) d\Delta + \frac{\partial f}{\partial x} \int_{-\infty}^{\infty} \Delta \phi(\Delta) d\Delta + \frac{\partial^2 f}{\partial x^2} \int_{-\infty}^{\infty} \frac{\Delta^2}{2} \phi(\Delta) d\Delta + \cdots$$
$$= f(x,t) + \frac{\partial^2 f}{\partial x^2} \int_{-\infty}^{\infty} \frac{\Delta^2}{2} \phi(\Delta) d\Delta + \cdots \qquad \text{Eq. 4}$$

It is clear that the second and higher order even terms vanish, being equivalent to being displaced and walking back to the starting position, and solving for $\frac{\partial f}{\partial t}$:

$$\frac{\partial f}{\partial \mathrm{t}} = \frac{\partial^2 f}{\partial x^2} \frac{1}{\tau} \int_{-\infty}^{\infty} \frac{\Delta^2}{2\tau} \phi(\Delta) \mathrm{d}\Delta + \cdots \qquad \text{Eq. 5}$$

The second moment of the probability of displacement is the diffusion coefficient (D):

$$\mathrm{D} = \frac{1}{\tau} \int_{-\infty}^{\infty} \frac{\Delta^2}{2\tau} \phi(\Delta) \mathrm{d}\Delta \qquad \text{Eq. 6}$$

From here, it is easy to see that the density of particles at point x at time t may be expressed using the so-called diffusion equation (also called Fick's Second Law):

$$\frac{\partial f}{\partial \mathrm{t}} = \mathrm{D} \cdot \frac{\partial^2 f}{\partial x^2} \qquad \text{Eq. 7}$$

This equation has a closed form solution, assuming N particles start from the origin at time t=0:

$$f(x,t) = \frac{N}{\sqrt{4\pi Dt}} e^{-\frac{x^2}{4Dt}} \quad \text{Eq. 8}$$

This is a normal distribution with zero mean and variance of 2Dt. The first moment of this equation is 0, which means particles are equally likely to go in any direction, which highlights that the random walk model is a stochastic process. The second moment is easily calculated as:

$$\bar{x}^2 = 2Dt, \quad \text{Eq. 9}$$

Where $\bar{x}^2$ is the mean squared displacement. The diffusion coefficient (D), or diffusivity, has units of $\frac{m^2}{s}$ and, for liquids, is a function of temperature and the viscosity of the inclosing medium.

2.2. The Bloch Equations

The next major development in diffusion measurement came with the popularity of nuclear magnetic resonance (NMR) spectroscopy in the 1940s. The underlying physics of magnetic resonance imaging (MRI) is driven by the nuclear magnetic resonance phenomenon which was first exploited for studying the magnetic properties of atomic nuclei by Isidor Isaac Rabi in 1937 and further quantified by Felix Bloch and Edward Purcell in the late 1940s. From Bloch (1946), a magnetic moment, μ, in the presence of a magnetic field, B, will experience a torque $\boldsymbol{\mu} \times \boldsymbol{B}$. Further, the torque, T, may be expressed as

$$\boldsymbol{T_s} = -\boldsymbol{B}_0 \times \boldsymbol{\mu} = -\gamma \boldsymbol{B}_0 \times \boldsymbol{a} \quad \text{Eq. 10}$$

Where, B_0, is a uniform magnetic field, γ is the gyromagnetic ratio, μ is the magnetic moment of a single proton (or Hydrogen nucleus), and $\boldsymbol{a}$ is the proton's angular momentum. The gyromagnetic ratio may be expressed as:

$$\gamma = \frac{|\boldsymbol{\mu}|}{|\boldsymbol{a}|}\left(\frac{MHz}{T}\right) \quad \text{Eq. 11}$$

γ_p is $42.58\frac{MHz}{T}$ for protons and is a useful measure to remember as it relates the precession frequency of a proton in a magnetic field. μ_p will align either parallel or antiparallel to B_0 and the torque will induce a precession about B_0. The induced torque is illustrated in Figure 2.

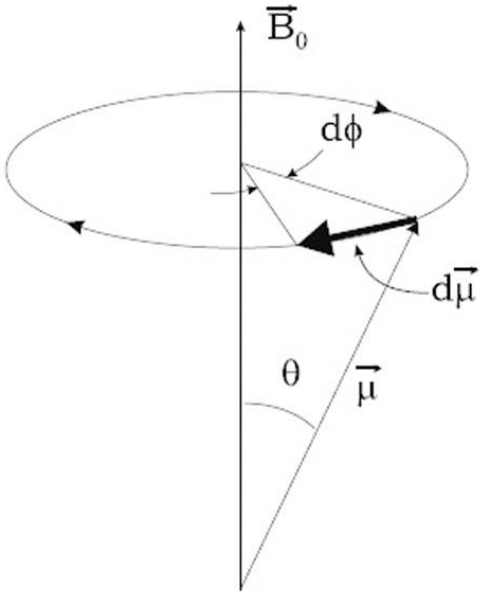

Figure 2: By definition, precession is the circular motion of the axis of rotation of a spinning body about another fixed axis caused by the application of a torque in the direction of the precession. The interaction of the proton's spin with the magnetic field produces the torque, causing it to precess about $\mathbf{B_0}$. When looking down from above the vector $\mathbf{B_0}$, the precession of the magnetic moment vector $\vec{\mu}$, which is proportional to the spin vector, is clockwise. Reprinted with permission from Magnetic Resonance Imaging. (2014). In Magnetic Resonance Imaging (pp. 1-17). https://doi.org/https://doi.org/10.1002/9781118633953.ch1

In truth, the mechanics of a single particle are not very interesting, nor practical to measure. For several particles subject to a magnetic field, $\mathbf{B_0}$, all magnetic moments will align either parallel or antiparallel. There is a slight preference for the lower energy parallel state, and for approximately every 10^6 particles, there will be one more particle that aligns parallel than

antiparallel. This means that there is a net magnetization, **M**, which is more meaningful to observe but behaves as a single particle as shown above. **M** is perpendicular to $\mathbf{B}_0$, causing all changes in M to be constrained to the x-y plane; by convention, we require $\mathbf{B}_0$ to lie along to the z-axis.

The torque is classically related to the change in angular momentum, **A**, via:

$$\boldsymbol{T} = \frac{d\boldsymbol{A}}{dt} = \boldsymbol{M} \times \boldsymbol{B_0} \qquad \text{Eq. 12}$$

Because $\gamma \boldsymbol{a} = \boldsymbol{\mu}$, for a single nucleus, $\gamma \boldsymbol{A} = \boldsymbol{M}$ for the ensemble. Taking the derivative with respect to time, the rate of change of **M**, $d\boldsymbol{M}/dt$, may be calculated like so:

$$\frac{d\boldsymbol{M}}{dt} = \gamma \frac{d\boldsymbol{A}}{dt} = \gamma[\boldsymbol{M} \times \boldsymbol{B_0}] \qquad \textit{Eq. 13}$$

If we define ϕ as the precession angle, we can determine the precession rate $d\phi/dt$ simply using the gyromagnetic ratio and $|\mathbf{B}_0|$:

$$\frac{d\phi}{dt} = \gamma|\boldsymbol{B_0}| \qquad \text{Eq. 14}$$

$\frac{d\phi}{dt}$ (MHz) is typically denoted as ω_0 (angular frequency) and is the well-known Larmor frequency.

The system in Eq. 14 is at equilibrium. A system introduced to $\mathbf{B}_0$ will require time to equilibrate, and **M** will be shared between the x-y plane and the z-axis. The time evolution of the net magnetization is governed by two relaxation terms. The first term is the longitudinal relaxation time or spin-lattice relaxation, called T1(s). T1 represents the recovery of **M** or the longitudinal magnetization. T2 is the spin-spin relaxation time and represents the decay of the transverse, or x-y, magnetization. The longitudinal magnetization is often denoted $\boldsymbol{M}_{\parallel}$ and the transverse magnetization is often denoted $\boldsymbol{M}_{\perp}$, where $M_{\perp} = M_x\hat{x} + M_y\hat{y}$.

In reality, the relaxation phenomena described here are not so much by chance but rather by design. Instead of introducing particles to $\mathbf{B_0}$ and allowing them to equilibrate to make a single measurement, the field is perturbed by an oscillating radiofrequency (RF) pulse, $\mathbf{B_1}$, which is played at the Larmor frequency of the protons in the medium of concern.

A rotating frame reference can be introduced, where the x-y plane rotates at an angular frequency, ω_0, which will be set to the spin precession frequency of the system. This is distinct from the laboratory frame of reference, which is defined about $\mathbf{B}_0$, conventionally called the z-axis, and is stationary. By setting ω_0 to the precession frequency, the frame rotates at the same speed as **M** rotates about $\mathbf{B}_0$, thereby, the system becomes stationary. Alternatively, this may be thought of as fixing ϕ at some value; therefore, the tipping of **M** onto the transverse plane appears to occur along a plane defined by $\{(0,0,0), (0,0,|\boldsymbol{M}|), (|\boldsymbol{M}|\cos\phi\,, |\boldsymbol{M}|\sin\phi\,, 0)\}$. Figure 3 shows a comparison of a) the rotating reference frame and b) the laboratory frame.

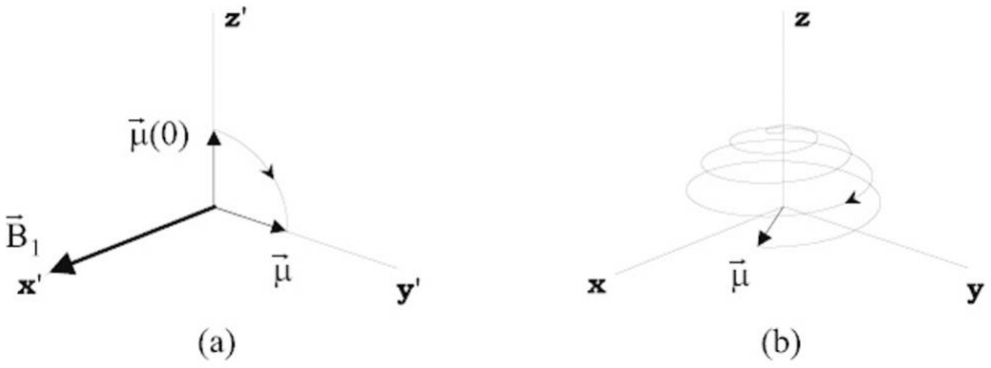

Figure 3: The effect of an rf pulse on an individual magnetic moment $\vec{\mu}$.(a) In a frame rotating about $\mathbf{B_0}$ (which is along z, say) at the Larmor frequency (with coordinates x′, y′ and z′ = z), there is no observed precession about $\mathbf{B_0}$. Upon application of an rf magnetic field pulse applied along x′, the magnetic moment is rotated about x′ at a rate corresponding to the frequency $\omega_1 = \gamma\mathbf{B_1}$ determined by the amplitude of the rf field, $\mathbf{B_1}$. A $\pi/2$ flip relative to its starting position

along zˆ is achieved in a time τrf provided that $\omega_1\tau rf = \pi/2$. (b) The behavior of the same magnetic moment rotation is observed to be more complicated in the fixed laboratory frame. Reprinted with permission from Magnetic Resonance Imaging. (2014). In Magnetic Resonance Imaging (pp. 1-17). https://doi.org/https://doi.org/10.1002/9781118633953.ch1

Because the magnetic moments are quantized, they may only absorb energy at the Larmor frequency. When an oscillating RF pulse is applied at ω_0, **M** is tipped into the transverse plane; thereby $\boldsymbol{M}_{\perp} \neq 0$ and $\boldsymbol{M}_{\parallel} < \boldsymbol{M}_0$, where $\mathbf{M_0}$ is the equilibrium net magnetization. In order for $\mathbf{B_1}$ to tip **M** into the transverse plane, it must itself lie in the transverse plane. Like Bloch's derivation, $\mathbf{B_1}$ is defined such that the effective external magnetic field, $\mathbf{B}=(B_x,B_y,B_z)=(|\mathbf{B}_1|\cos(\phi), |\mathbf{B}_1|\sin(\phi), |\mathbf{B}_0|)$. Further, constrain $\mathbf{B}_1$ to oscillate at ω_0.

It would be nice to know the time evolution of the magnetization lying on each axis. Let $\boldsymbol{M} = (\boldsymbol{M_x}, \boldsymbol{M_y}, \boldsymbol{M_z})$. Then, the signal from the above derivation of $\frac{\boldsymbol{dM}}{\boldsymbol{dt}}$ becomes:

$$\frac{dM_x(t)}{dt} = (\gamma \boldsymbol{M}(t) \times \boldsymbol{B}(t))_{\boldsymbol{x}} \quad \text{Eq. 15}$$

$$\frac{dM_y(t)}{dt} = (\gamma \boldsymbol{M}(t) \times \boldsymbol{B}(t))_{\boldsymbol{y}} \quad \text{Eq. 16}$$

$$\frac{dM_z(t)}{dt} = (\gamma \boldsymbol{M}(t) \times \boldsymbol{B}(t))_{\boldsymbol{z}} \quad \text{Eq. 17}$$

Bloch noted, however, that these equations are not sufficient and that additional terms needed to be considered. The first effect he considered is what would later become known as the spin-lattice relaxation. With the added deposited energy from the $\mathbf{B_1}$ field, the ensemble of protons enters an excited state that is thermally unstable and locally alters the magnetic field due to increased vibrations of the protons. The spin-lattice relaxation time or longitudinal relaxation time (T1) is the time it takes for 63% of the longitudinal magnetization to recover or 63% of the

moments to return to their equilibrium states. As T1 is related to the recovery of the signal oscillating about $\mathbf{B}_0$, it influences the rate of change of M_z.

The second phenomenon is known as the transverse relaxation or spin-spin relaxation and emerges due to local inhomogeneities in $\mathbf{B}_0$ and the presence of other magnetic moments. The local changes in the static field cause the dephasing of the transverse magnetization to deviate from the values expected from Eq. 15-17 above. The spin-spin relaxation time or the transverse relaxation time (T2) is the amount of time it takes for the transverse magnetization to decay to 37% of its maximum value.

Eq. 13 may be modified to account for these effects:

$$\frac{d\boldsymbol{M}}{dt} = -\gamma(\boldsymbol{M} \times \boldsymbol{B}) - \frac{M_x\hat{x}}{T2} - \frac{M_y\hat{y}}{T2} + \frac{(M_0 - M_z)\hat{z}}{T_1} \quad \text{Eq. 18}$$

The rates of change of the components of **M** along each axis then become the well-known Bloch Equations:

$$\frac{dM_x(t)}{dt} = (\gamma \boldsymbol{M}(t) \times \boldsymbol{B}(t))_{\boldsymbol{x}} - \frac{M_x(t)}{T2} \quad \text{Eq. 19}$$

$$\frac{dM_y(t)}{dt} = (\gamma \boldsymbol{M}(t) \times \boldsymbol{B}(t))_{\boldsymbol{y}} - \frac{M_y(t)}{T2} \quad \text{Eq. 20}$$

$$\frac{dM_z(t)}{dt} = (\gamma \boldsymbol{M}(t) \times \boldsymbol{B}(t))_{\boldsymbol{z}} + \frac{(M_0 - M_z(t))}{T1} \quad \text{Eq. 21}$$

The solution to this simple system of linear differential equations is given by:

$$\boldsymbol{M_x} = \boldsymbol{M_0} e^{-t/T2} \quad \text{Eq. 22}$$

$$\boldsymbol{M_y} = \boldsymbol{M_0} e^{-t/T2} \quad \text{Eq. 23}$$

$$\boldsymbol{M_z} = \boldsymbol{M_0}(1 - e^{-t/T1}) \quad \text{Eq. 24}$$

The resonance produced by $\mathbf{B_1}$ is unstable upon the removal of the field, due to its energized state. Quantum mechanics dictates that the system will seek to return to the lower energy state at

equilibrium by emitting an RF pulse equal to $\mathbf{B_1}$. In a classical conceptualization, the decay of $\boldsymbol{M}_{\perp}$ and recovery of $\boldsymbol{M}_{\parallel}$ produces a magnetic flux. By Faraday's Law of Induction, this flux results in a small current in the receiver coil that produces the measured signal in MRI.

The *flip angle* or tipping angle, α, is a specified parameter in scanning that determines the proportion of $\boldsymbol{M}_{\parallel}$ that is projected or tipped onto the transverse plane. In spin-echo sequences, which are of concern for this work, only 90° excitation and 180° refocusing RF pulses are applied. The 90° pulse projects **M** entirely onto the transverse plane. $\boldsymbol{M}_{\perp}$ partially dephases due to field inhomogeneities; this dephasing is governed by what is known as the T2* time, which is expressed as:

$$\frac{1}{T2^*} = \frac{1}{T2} + \frac{1}{T2_{in}} \qquad \text{Eq. 25}$$

Where $T2_{in}$ is the decay time caused by local field distortions. It is clear that T2* is always less than T2. This means that experiments that do not account for field inhomogeneities will see $\boldsymbol{M}_{\perp}$ decay faster than what would be expected by T2. In spin-echo experiments, the 180° pulse is applied to remove T2* effects. The 180° pulse effectively flips the transverse magnetization, thereby, the faster spins catch up to the slower spins and $\boldsymbol{M}_{\perp}$ briefly regains coherence and is called a *spin echo*. The acquired echo is free of inhomogeneity contributions and is T2-weighted.

On the topic of spin echo measurements, it is useful to introduce some terminology, namely the repetition time (TR) and echo time (TE). TR is the time between the peaks of 90° pulses, and TE is the time from the peak of the 90° pulse to the center of the echo. It is also interesting to note that the time from center of the 90° pulse to the center of the 180° is TE/2, which is also the time from the center of the 180° pulse to the center of the echo. An example of a spin echo sequence is shown in Figure 4. For now, only the RF pulse and signal acquisition

aspects of Figure 4 are of interest, but the slice, phase, and frequency encoding elements will be revisited in the image acquisition section.

2.3. Carr & Purcell and the first diffusion NMR experiments

Although the first spin echo experiments were performed by Hahn (1950), this work will focus primarily on the contributions of Carr and Purcell (1954), which were the first to employ spin echoes for both the elimination of diffusion effects and the quantification of the self-diffusion coefficient (D). Like Einstein's derivation, Carr and Purcell used a random walk model of diffusion, wherein a particle remains at a location z for τ seconds before moving to a new location one step away. Each step was of length ζa_i, where ζ is $\sqrt{\bar{\boldsymbol{z}}_{\boldsymbol{i}}^{\boldsymbol{2}}}$ or the root mean squared (rms) displacement of a 3D jump defined by $\boldsymbol{\delta} = \sqrt{\boldsymbol{3}\bar{\boldsymbol{z}}_{\boldsymbol{i}}^{\boldsymbol{2}}}$ and a_i may be 1 or -1. The goal is now to quantify the change in precession resulting from the movement of the particle. Let's assume there is a gradient, B_z, which is applied along z with strength G. $B_z(0)$ is the strength of the field observed by a particle at t=0. If the particle diffuses for $t=j\tau$, it will observe a field given by:

$$\boldsymbol{B}_{\boldsymbol{z}}(j\tau) = \boldsymbol{B}_{\boldsymbol{z}}(0) + G\zeta \sum_{i=1}^{j} a_i \qquad \text{Eq. 26}$$

The change in phase (ϕ) will differ from its original value (ϕ_0) by:

$$\Delta\phi = \phi - \phi_0 = \sum_{i=1}^{N} \gamma\tau\big(\boldsymbol{B}_{\boldsymbol{z}}(j\tau) - \boldsymbol{B}_{\boldsymbol{z}}(0)\big) = G\zeta\gamma\tau \sum_{i=1}^{N} i a_i \qquad \text{Eq. 27}$$

Where *N* is the number of steps occurring in $j\tau$. Extending for an infinite number of infinitesimal steps, we arrive at the continuous diffusion estimate and may represent Einstein's definition of D in terms of Carr and Purcell's derivation:

$$D = \frac{\zeta^2}{2\tau} \quad \text{Eq. 28}$$

With extremely large N, we have:

$$\sqrt{\bar{\phi}_D^2} = G^2\gamma^2 D t^3/6n^2 \quad \text{Eq. 29}$$

Carr and Purcell then calculated the diffusion component of the intensity of the nth echo:

$$\boldsymbol{M_y}(t) = M_0 \int_{-\infty}^{\infty} \cos\phi_D P(\phi_D) d\phi_D = M_0 e^{-\gamma^2 G^2 D t^3/12n^2} \quad \text{Eq. 30}$$

Where P($\boldsymbol{\phi_D}$) is the probability of a displacement of $\boldsymbol{\phi_D}$. The total transverse signal is then given by:

$$\boldsymbol{M_y(t) = M_0 e^{-t/T2} e^{-\gamma^2 G^2 D t^3/12n^2}} \quad \text{Eq. 31}$$

The diffusion coefficient is then given by:

$$\mathrm{D} = [\ln\left(\frac{\boldsymbol{M_y}(t)}{M_0}\right) + t/T2]\frac{-12n^2}{\gamma^2 G^2 t^3} \quad \text{Eq. 32}$$

Carr and Purcell were able to experimentally determine D by applying a small current through wires on either side of the sample to produce a diffusion weighting along the magnetic field produced by the two wires.

2.4. The Bloch-Torey Equations

The Bloch equations were observed to perform quite well in fluids; however, they neglected to account for the magnetic effects resulting from the random movement, i.e., diffusion, of particles in the media observed.

In 1956, H. C. Torrey introduced a reformulation of the Bloch Equation accounting for the diffusion of magnetic moments. These now famous equations are known as the Bloch-Torrey Equation.

$$\frac{\partial \boldsymbol{M}(t)}{\partial t} = \gamma(\boldsymbol{M} \times \boldsymbol{B}) - \frac{\boldsymbol{M}_{\perp}(t)}{T2} + \frac{\boldsymbol{M}_{\parallel}(0) - \boldsymbol{M}_{\parallel}(t)}{T1} + \nabla \cdot D\nabla(\boldsymbol{M}(t) - \boldsymbol{M}(0)) \quad \text{Eq. 33}$$

Which in respect to each axis is given by:

$$\frac{\partial \boldsymbol{M_x}(t)}{\partial t} = \gamma(\boldsymbol{M} \times \boldsymbol{B})_x - \frac{\boldsymbol{M_x}(t)}{T2} + \nabla \cdot D\nabla(\boldsymbol{M_x}(t) - \boldsymbol{M_x}(0)) \quad \text{Eq. 34}$$

$$\frac{\partial \boldsymbol{M_y}(t)}{\partial t} = \gamma(\boldsymbol{M} \times \boldsymbol{B})_y - \frac{\boldsymbol{M_y}(t)}{T2} + \nabla \cdot D\nabla(\boldsymbol{M_y}(t) - \boldsymbol{M_y}(0)) \quad \text{Eq. 35}$$

$$\frac{\partial \boldsymbol{M_z}(t)}{\partial t} = \gamma(\boldsymbol{M} \times \boldsymbol{B})_z + \frac{\boldsymbol{M_z}(0) - \boldsymbol{M_z}(t)}{T1} + \nabla \cdot D\nabla(\boldsymbol{M_z}(t) - \boldsymbol{M_z}(0)) \quad \text{Eq. 36}$$

Torrey derived that the rate of increase of a given component of the magnetic moment due the diffusion current in that direction is given by the divergence of the diffusion coefficient times the gradient of the change in M.

2.5. Pulsed Gradient Spin Echo (PGSE)

At this point, the reader may be under the impression that the diffusion signal contribution is a nuisance term, and, for many NMR experiments, it is. Transient particles diffusing through the field-of-view during an experiment could lead to signal aberrations that could alter the observed spectra; however, this work, and hundreds of others, will show that this is not always the case. The diffusion information can be both a powerful and insightful tool.

The work of Stejskal and Tanner (1965) at the University of Wisconsin, introduced pulsed gradients to the standard spin echo (SE) sequence. The addition of a second set of gradients allowed NMR to encode diffusion weighting and introduced the pulsed gradient spin echo (PGSE) sequence that is the basis of modern diffusion weighted imaging (DWI). Stejskal

and Tanner solved the Bloch-Torrey partial differential equations with the addition of diffusion gradients, which became known as the Stejskal-Tanner formula:

$$S = S_0 e^{-bD}, \quad \text{Eq. 37}$$

where S is the diffusion weighted signal, S_0 is the non-diffusion weighted signal, and b is defined as:

$$b = \gamma^2 G^2 \delta^2 (\Delta - \delta/3) \quad \text{Eq. 38}$$

γ ($\frac{rad}{s \cdot T}$) is the gyromagnetic ratio, G ($\frac{T}{m}$) is the diffusion gradient strength, δ(s)is the duration of the gradient pulse, and Δ (s) is the spacing between the start of gradient pulses. *b* is typically called the *b-value* and is used to prescribe the amount of diffusion weighting in an image.

Calculating one D value for the entire brain is not very informative, so naturally, the PGSE was extended to include slice-select and phase encoding gradients, which allow for the coding of three-dimensional information and forms the basis of DWI. The PGSE pulse sequence diagram is shown below:

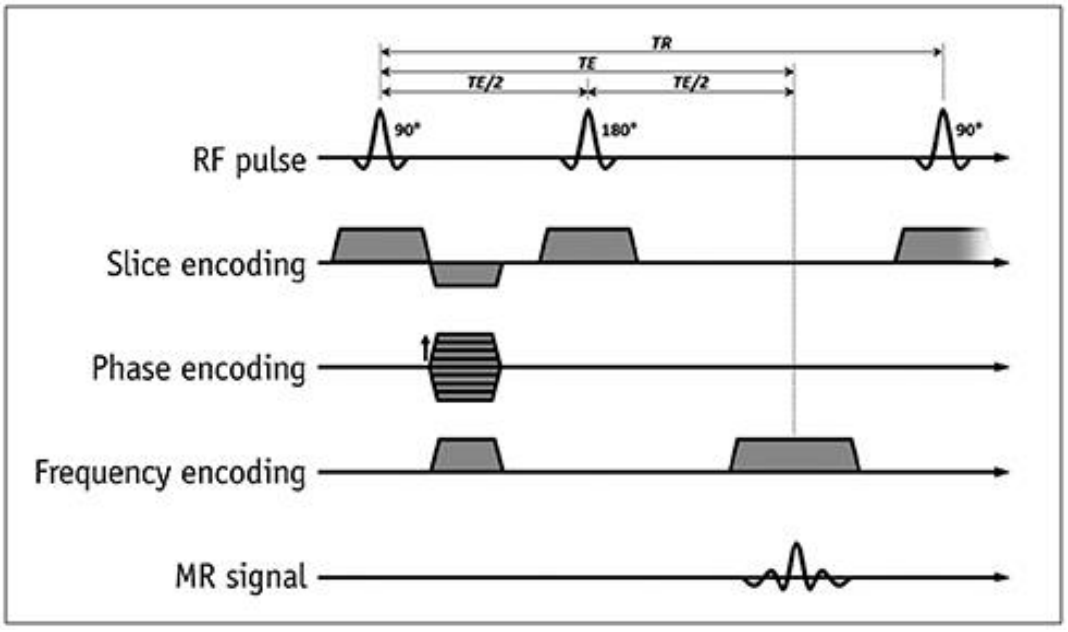

Figure 4: A basic spin echo pulse sequence diagram. Reprinted from Jo, Y., Kim, J., Park, C. H., Lee, J. W., Hur, J. H., Yang, D. H., Lee, B. Y., Im, D. J., Hong, S. J., Kim, E. Y., Park, E.-A., Kim, P. K., & Yong, H. S. (2019, 9/). Guideline for Cardiovascular Magnetic Resonance

Imaging from the Korean Society of Cardiovascular Imaging—Part 1: Standardized Protocol. Korean J Radiol, 20(9), 1313-1333.

2.6. Diffusion Tensor Imaging

Calculating the ADC at each point in the brain, while clinically useful for stroke imaging, is not the most informative for research. It is desirable to better characterize the three-dimensional motion of water within a voxel. One way to achieve this is by devising an acquisition scheme that can be fitted using a tensor or an ellipsoid. A tensor is a symmetric covariance matrix that serves as a mapping between vector spaces.

Diffusion tensor imaging (DTI) was introduced by (Basser et al., 1994a, 1994b) to develop a tensor-based imaging protocol, which uses a set of diffusion gradients to encode the diffusivity of water along the three principal directions. An adapted derivation of the diffusion tensor imaging method as originally published in *MR Diffusion Tensor Spectroscopy Imaging* (Basser et al., 1994b) and *Estimation of the Effective Self-Diffusion Tensor from the NMR Spin Echo* (Basser et al., 1994a) follows and is reproduced with permission.

Calculating the effective diffusion tensor, $\mathbf{D^{eff}}$, requires the use of Fick's First Law:

$$\boldsymbol{J} = -\boldsymbol{D}^{eff}\nabla\boldsymbol{C} \quad \text{Eq. 39}$$

Where **J** and **C** are the macroscopic diffusive flux and concentration vectors, respectively. ∇C is the gradient of the concentration and represents the vector field of the concentration. In isotropic media, the magnitude of the magnetization at the receipt of the echo, *A(TE)*, is related to D by:

$$ln\left[\frac{A(TE)}{A(0)}\right] = -\gamma^2 \int_0^{TE} (\boldsymbol{F}(t') - 2H(t' - \frac{TE}{2})\boldsymbol{f})^T \cdot D(\boldsymbol{F}(t') - 2H\left(t' - \frac{TE}{2}\right)\boldsymbol{f})dt' \quad \text{Eq. 40}$$

Where *H(t)* is the Heaviside function, i.e., $H(t) = \begin{cases} 1, t > 0 \\ 0, t < 0 \end{cases}$, A(0) is the magnetization immediately after the 90° pulse, and **F** and **f** are defined in terms of the Gradient strength applied as follows:

$$\boldsymbol{G}(t) = (G_x(t), G_y(t), G_z(t))^T = \int_0^t \boldsymbol{F}(t'')dt''; \boldsymbol{f} = \boldsymbol{F}(\frac{TE}{2}) \quad \text{Eq. 41}$$

If we collect $\gamma^2 \int_0^{TE}(\boldsymbol{F}(t') - 2H(t' - \frac{TE}{2})\boldsymbol{f})^T \cdot (\boldsymbol{F}(t') - 2H\left(t' - \frac{TE}{2}\right)\boldsymbol{f})dt'$ into a single term called *b*, D^{eff} in terms of Stejskal-Tanner above becomes:

$$ln\left[\frac{A(TE)}{A(0)}\right] = -bD^{eff} \quad \text{Eq. 42}$$

For anisotropic media, D^{eff} may be easily replaced with the diffusion tensor, $\boldsymbol{D}$:

$$ln\left[\frac{A(TE)}{A(0)}\right] = -\gamma^2 \int_0^{TE}(\boldsymbol{F}(t') - 2H(t' - \frac{TE}{2})\boldsymbol{f})^T \cdot \boldsymbol{D}(\boldsymbol{F}(t') - 2H\left(t' - \frac{TE}{2}\right)\boldsymbol{f})dt' \quad \text{Eq. 43}$$

Basser et al. (1994a) were able to restate Stejskal and Tanner's derivation above in terms of a linear relationship between the attenuated signal and the effective diffusion tensor, $\boldsymbol{D^{eff}}$:

$$ln\left[\frac{A(TE)}{A(0)}\right] = -\sum_{\boldsymbol{i=1}}^{\boldsymbol{3}}\sum_{\boldsymbol{j=1}}^{\boldsymbol{3}} b_{ij}D_{ij}^{eff} \quad \text{Eq. 44}$$

Because $\boldsymbol{D^{eff}}$ is positive definite, its eigenvectors (e_1, e_2, e_3) exist and are perpendicular, further, its eigenvalues (λ_1, λ_2, λ_3) are real valued. Without loss of generality, let $\lambda_1 > \lambda_2 > \lambda_3$, where λ_1 is the eigenvalue of the principal diffusion axis. The eigenvalues are the diffusivities along each of the three orthogonal diffusion axes. From linear algebra, we can restate $\boldsymbol{D^{eff}}$ in terms of its eigenvectors and eigenvalues:

$$\boldsymbol{D_{eff}E = E\Lambda} \quad \text{Eq. 45}$$

Where $\mathbf{E}=(e_1|e_2|e_3)$ and $\boldsymbol{\Lambda} = \begin{bmatrix}\lambda_1 & 0 & 0\\ 0 & \lambda_2 & 0\\ 0 & 0 & \lambda_3\end{bmatrix}$.

The diffusion tensor, $\boldsymbol{D}$, is expressed as:

$$\boldsymbol{D} = \begin{bmatrix}D_{xx} & D_{yx} & D_{zx}\\ D_{xy} & D_{yy} & D_{xy}\\ D_{xz} & D_{yz} & D_{zz}\end{bmatrix} \quad \text{Eq. 46}$$

where D_{ii} are the variances along the principal diffusion directions and $\boldsymbol{D_{ij}}$ are the covariances between the *i* and *j* directions. As the $\boldsymbol{D}$ is symmetric, meaning $D_{ij} = D_{ji}$, we need only measure six diffusion-weighted and one non-diffusion-weighted (b_0) image. In practice, this is not enough information to produce a tensor that is informative or stable. The diffusion ellipsoid can be calculated using the standard equation for an ellipsoid:

$$\frac{x^2}{a^2}+\frac{y^2}{b^2}+\frac{z^2}{c^2}=1=\left(\frac{x'}{\sqrt{2\lambda_1\tau}}\right)^2+\left(\frac{y'}{\sqrt{2\lambda_2\tau}}\right)^2+\left(\frac{z'}{\sqrt{2\lambda_3\tau}}\right)^2 \quad \text{Eq. 47}$$

Figure 5 shows the practical details of populating the diffusion tensor and calculating the eigenvalues and eigenvectors. Figure 6 shows the steps for transforming the apparent diffusion coefficients in order to calculate a diffusion ellipsoid aligned along the principal diffusion axis.

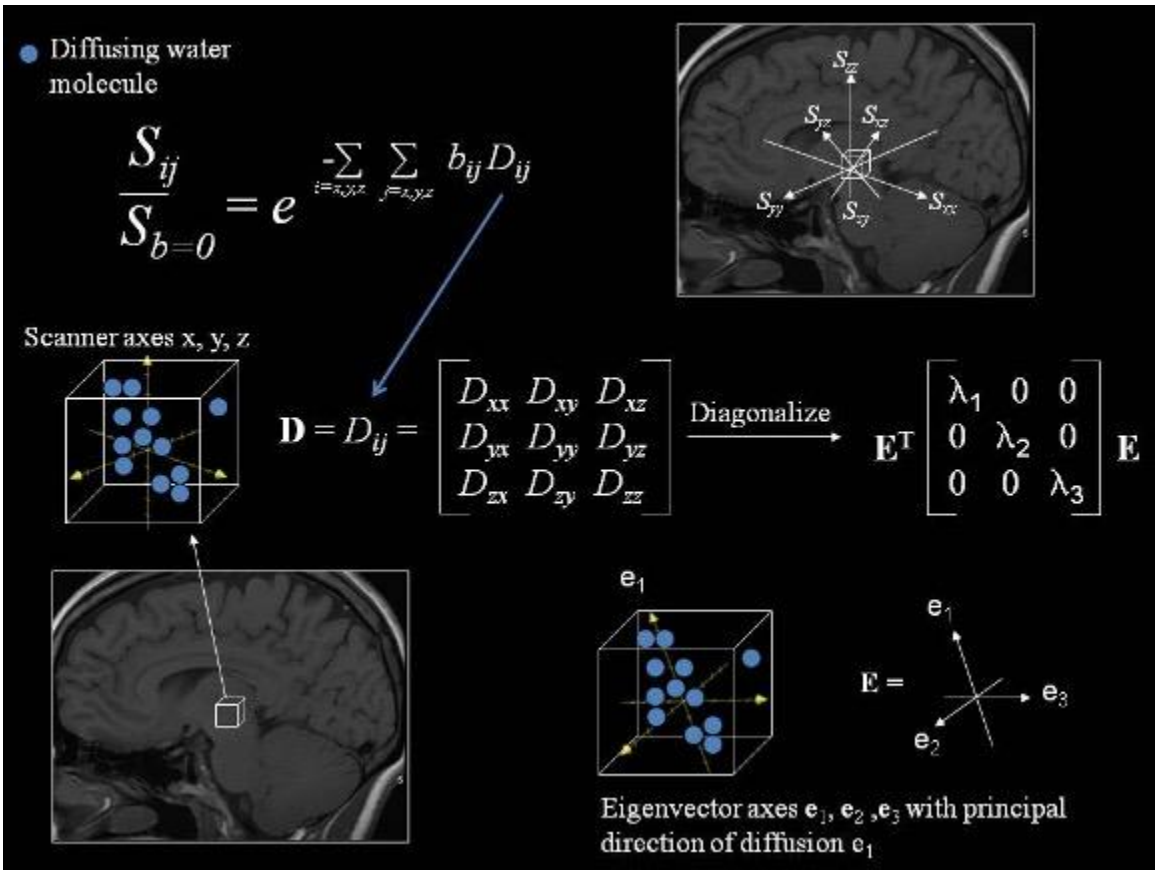

Figure 5: Populating the diffusion tensor. Reprinted with permission from Gallagher, T. A., Alexander, A. L., & Field, A. S. (2012). Diffusion Tensor Magnetic Resonance Imaging: Physical Principles. In S. H. Faro, F. B. Mohamed, M. Law, & J. T. Ulmer (Eds.), Functional Neuroradiology: Principles and Clinical Applications (pp. 709-729). Springer US.

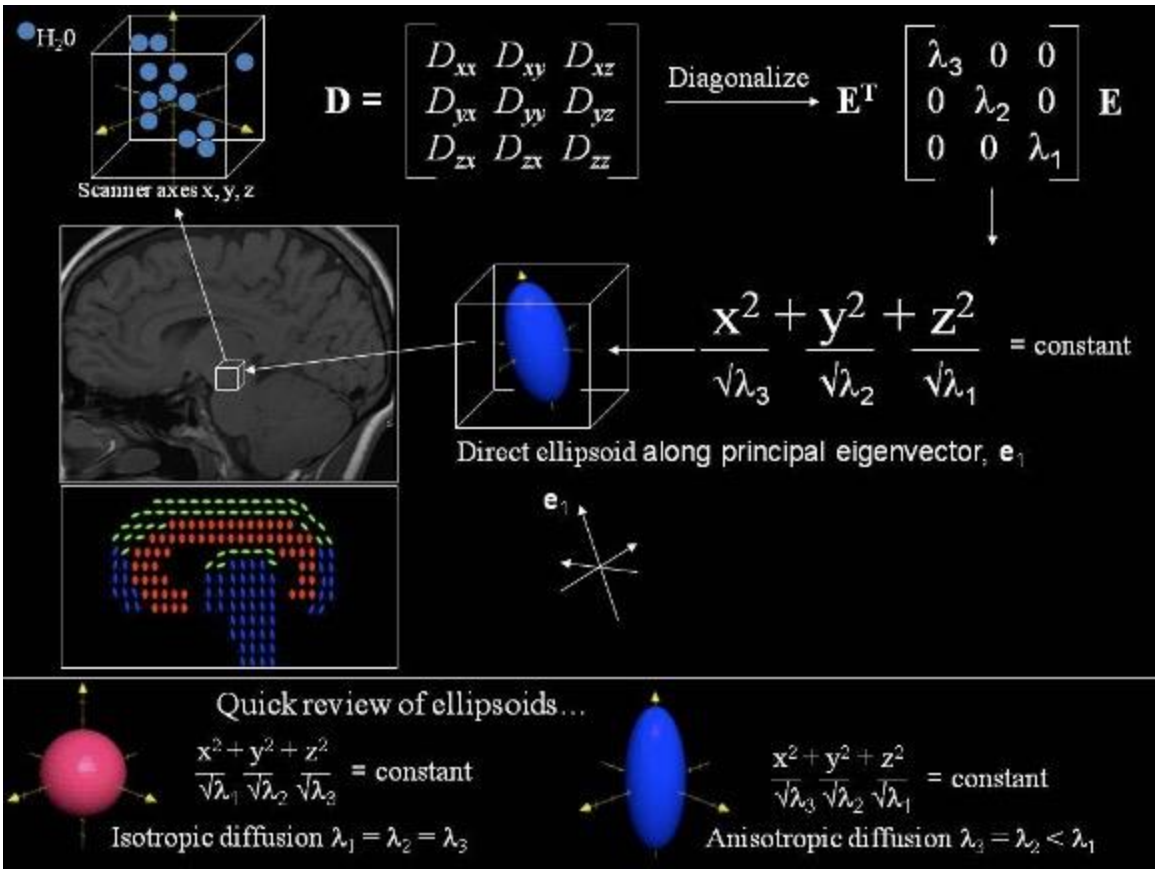

Figure 6: Calculating the tensor. Reprinted with permission from Gallagher, T. A., Alexander, A. L., & Field, A. S. (2012). Diffusion Tensor Magnetic Resonance Imaging: Physical Principles. In S. H. Faro, F. B. Mohamed, M. Law, & J. T. Ulmer (Eds.), Functional Neuroradiology: Principles and Clinical Applications (pp. 709-729). Springer US. https://doi.org/10.1007/978-1-4419-0345-7_35

There are a number of ways of estimating the diffusion tensor. In the original formulation proposed by Basser et al. (1994a), the tensor is estimated by solving a multivariate regression problem using weighted linear least squares. Define a 7x1 vector, $\boldsymbol{\alpha}$:

$$\boldsymbol{\alpha} = \left\{D_{xx}^{eff}, D_{yy}^{eff}, D_{zz}^{eff}, D_{xy}^{eff}, D_{xz}^{eff}, D_{yz}^{eff}, \ln[\boldsymbol{A}(0)]\right\}^{T} \quad \text{Eq. 48}$$

Let $\boldsymbol{B}$ represent the *n* x *7* (n=total number of measurements) matrix of b-values:

$$\boldsymbol{B} = \begin{bmatrix} -b_{xx1} & -b_{yy1} & -b_{zz1} & -b_{xx1} & -2b_{xy1} & -2b_{xz1} & -2b_{yz1} & 1 \\ \vdots & \vdots & \vdots & \vdots & \vdots & \vdots & \vdots & \vdots \\ -b_{xxN} & -b_{yyN} & -b_{zzN} & -b_{xxN} & -2b_{xyN} & -2b_{xzN} & -2b_{yzN} & 1 \end{bmatrix} \quad \text{Eq. 49}$$

The predicted outcomes, ξ, based on the diffusion weighting may be defined as:

$$\boldsymbol{\xi} = \boldsymbol{B}\boldsymbol{\alpha} \quad \text{Eq. 50}$$

To minimize the χ^2-error, which is the weighted sum of squares of deviations between the observed and predicted echo intensities and is given by:

$$\chi^2(\xi) = (x - \xi)^T \Sigma^{-1} (x - \xi) \quad \text{Eq. 51}$$

Where Σ^{-1} is a diagonal covariance matrix with the corrected reciprocal error variance for that measurement, x_i^2 / σ_i^2 on the diagonal and **x** is populated by the observed measurements. The optimal parameters of $\boldsymbol{\alpha}$ minimizing $\chi^2(\xi)$ is given by the weighted linear least squares solution:

$$\boldsymbol{\alpha}_{opt} = (\boldsymbol{B}^T \boldsymbol{\Sigma}^{-1} \boldsymbol{B})^{-1} (\boldsymbol{B}^T \boldsymbol{\Sigma}^{-1})^{-1} \boldsymbol{x} \quad \text{Eq. 52}$$

The terms *isotropic* and *anisotropic* diffusion have and will repeatedly arise in this work and Figure 6 presents a clear picture of the difference between the two. Isotropic diffusion is shown in the bottom left of Figure 6 and anisotropic diffusion is shown on the right. Isotropic diffusion occurs when $\lambda_1 \approx \lambda_2 \approx \lambda_3$. An isotropic diffusion ellipsoid is simply a sphere and the diffusion of coefficient for an entire voxel is accurate because it represents the likelihood of diffusion in any direction, which is equal across the three diffusion axes. In an anisotropic environment, where the diffusion tensor is most useful, some property of the environment (cytoarchitecture, cell membranes, etc.) causes diffusion perpendicular to the principal diffusion axis to be restricted, while diffusion along the principal diffusion axis is largely unimpeded. Physiologically speaking in white matter, fiber bundles are an environment of restricted diffusion wherein the principal axis of the fiber is the preferred diffusion direction and diffusion is restricted in the remaining diffusion axes.

A rotationally invariant scalar has emerged to assess the degree of anisotropy in a voxel called *fractional anisotropy* (FA), which may be calculated using the eigenvalues:

$$FA = \sqrt{\frac{3}{2}}\frac{\sqrt{(\lambda_1-\bar{\lambda})^2+(\lambda_2-\bar{\lambda})^2+(\lambda_3-\bar{\lambda})^2}}{\sqrt{\lambda_1^2+\lambda_2^2+\lambda_3^2}} \quad \text{Eq. 53}$$

Where $\bar{\lambda} = Mean\ Diffusivity\ (MD) = \frac{\sum_{i=1}^{3}\lambda_i}{3}$. Two other useful measures are axial (parallel) diffusivity (AD), which is merely λ_1, and radial (perpendicular) diffusivity (RD), which is the average of λ_2 and λ_3. Note that MD is also rotationally invariant, and all diffusivities have units of $mm^2/_s$. For isotropic media, the assignment of λ_1 becomes arbitrary and AD may not be a stable measure. Two nice things about the weighted-least squares approach are that it is intuitive and not computationally heavy. For imaging studies of populations that are likelier to move during a scan, this computational efficiency allows for many diffusion volumes to be collected without significantly increasing processing time. These extra volumes may act as *insurance,* if many volumes need to be removed due to artifacts, an accurate tensor may still be produced. Practically speaking, most protocols can tolerate the removal of up to 10% of diffusion volumes and still produce reliable results. It is also important to note that there are other methods for estimating the tensor, including nonlinear least squares (Kingsley, 2006), Robust Estimation of Tensors by Outlier Rejection (RESTORE) (Chang et al., 2005), and Informed RESTORE (L.-C. Chang et al., 2012). RESTORE and Informed RESTORE are particularly useful as they are able to remove volumes containing artifacts and physiological noise (Chang et al., 2005; L. C. Chang et al., 2012).

2.7. Neurite Orientation Dispersion and Density Imaging (NODDI)

DTI is not without its limitations. DTI is only valid for a range of diffusion weightings where the diffusion is approximately Gaussian, typically b<1500 $^{s}/_{mm^2}$. With increasing b-value, the observed diffusion becomes more non-linear and non-Gaussian. Above 1500$^{s}/_{mm^2}$ the tensor model should not be used. Further, DTI is not able to resolve overlapping fibers. This is particularly bad in instances when fibers cross perpendicularly within a voxel, which is typically 2mm x 2mm x 2mm. As the voxel size is much larger than the size of WM fibers, DTI is only able to represent the average diffusion signal in a voxel. This means that the healthy perpendicular fibers could artificially produce a high MD value with very small FA, which is typically shown in literature to be associated with white matter decline. This is not a desirable result.

The use of high diffusion weighting in MRI has long been explored and several models derived, including Composite hindered and restricted model of diffusion (CHARMED)(Assaf & Basser, 2005) and the neurite orientation dispersion and density imaging (NODDI) model (Zhang, Schneider, et al., 2012) This work will focus on the NODDI model.

NODDI is a three-compartment model comprised of glial (extra-cellular), neurite (intra-cellular), and CSF compartments and has the added utility, where other models such as CHARMED have fallen short, to retain information regarding the changing in diffusion due to the degree of fanning and dispersion of axons in a voxel. A summary of Zhang, Schneider, et al. (2012)NODDI treats the normalized, full signal *A* as:

$$A = (1 - v_{iso})(v_{ic}A_{ic} + (1 - v_{ic})A_{ec} + v_{iso}A_{iso} \quad \text{Eq. 54}$$

Where A_{ic} and v_{ic} are the normalized signal and volume fraction of inter-cellular (IC) compartment; A_{ec} is the normalized extra-cellular (EC) compartment; and A_{iso} and v_{iso} are the normalized signal and volume fraction of the CSF (isotropic) compartment.

The IC compartment is defined by cell membranes of neurites and is modelled as cylinders of zero radius and A_{ic}:

$$A_{ic} = \int_{\mathbb{S}^2} f(\boldsymbol{n}) e^{-b d_{\parallel} (\boldsymbol{q}\cdot\boldsymbol{n})^2} d\boldsymbol{n} \quad \text{Eq. 55}$$

Where **q** is the gradient direction and b is the diffusion weighting, $d_{\parallel}$ is the diffusivity parallel to the fiber axis, $f(\boldsymbol{n})d\boldsymbol{n}$ gives the probability of finding sticks along orientation **n**. The orientation distribution function is modeled with a Watson distribution centered around $\boldsymbol{\mu}$ and extent of dispersion κ:

$$f(\boldsymbol{n}) = M\left(\frac{1}{2}, \frac{3}{2}, \kappa\right)^{-1} e^{\kappa(\boldsymbol{\mu}\cdot\boldsymbol{n})^2} \quad \text{Eq. 56}$$

M is a confluent hypergeometric function.

The EC (glial) and CSF compartments are modeled as anisotropic and isotropic diffusion, respectively, using the tensor model discussed above. Useful measures derived from NODDI include the neurite density index (NDI), which is simply v_{ic} and the orientation dispersion index (ODI), which is a measure of the degree of fanning in an axon. ODI is governed by the concentration parameter κ introduced above. ODI is calculated as:

$$ODI = \frac{2}{\pi} \tan^{-1} \frac{1}{\kappa} \quad \text{Eq. 57}$$

Figure 7 shows a Watson distribution with the same orientation but different ODI values. Figure 8 presents a comparison of DTI and NODDI derived measures.

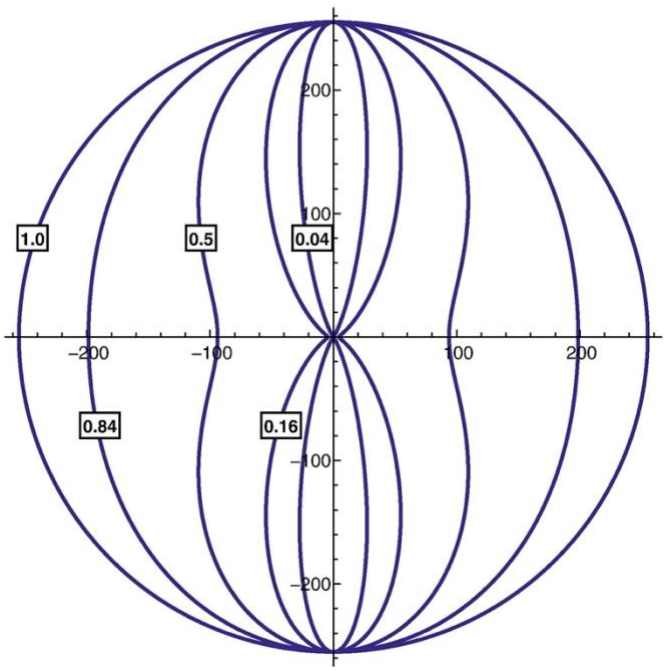

Figure 7: Illustration of a set of Watson distributions with the same mean orientation but different orientation dispersion index: ODI = 0.04, 0.16, 0.5, 0.84, 1.0. Reprinted with permission from Zhang, H., Schneider, T., Wheeler-Kingshott, C. A., & Alexander, D. C. (2012, Jul 16). NODDI: practical in vivo neurite orientation dispersion and density imaging of the human brain. Neuroimage, 61(4), 1000-1016.

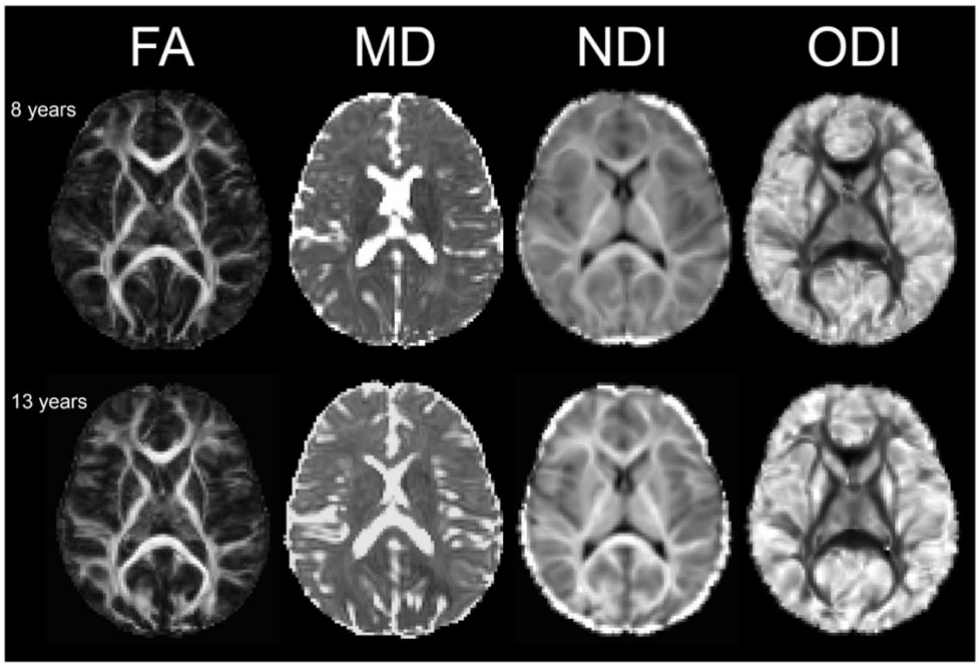

Figure 8: Comparison of DTI and NODDI measures in an 8-year-old male and 13-year-old female. Reprinted with permission from Mah, A., Geeraert, B., & Lebel, C. (2017). Detailing neuroanatomical development in late childhood and early adolescence using NODDI. PLoS One, 12(8), e0182340. https://doi.org/10.1371/journal.pone.0182340

2.8. Image Acquisition and Common Artifacts

So far, this work has revealed precious little about the actual acquisition of MR images, rather focusing on the physics of interest and the evolution of signal. From the outsider perspective, the I of MRI evokes the idea of a camera, which is not the case. MR images are acquired in frequency space, or k-space, which may be transformed into the spatiotemporal (image) space using the Fourier transform. k-space is conventionally arranged so that phase is on the ordinate axis and frequency on the abscissa. A point in k-space contains information about every point in the image space, rather than a direct one-to-one correspondence. The key to spatial encoding in MRI is the use of gradient magnets, which perturb $\mathbf{B}_0$ and, thus, ω in a predictable spatial dependence (typically linear). By applying a gradient that shifts ω at say +15mm of isocenter, and then playing an RF pulse corresponding to ω at +15mm, the received signal will come from protons at that 'slice' in space. This is known as slice-selection. Likewise, the phase encode and frequency encode gradients then select the point in k-space within a slice to be sampled. Again, this should not be equated with filling a single point in the image space, as one could collect a single point in k-space and still produce an, albeit boring, image.

In practice, the serial stimulation of an echo and cartesian filling of k-space are extremely inefficient. Several methods have evolved to make the filling of k-space faster: single-shot echo planar imaging (EPI), multi-shot EPI, simultaneous multi-slice (SMS), and non-cartesian k-space filling (e.g., radial, propeller, and spiral). This work will focus only on single-shot EPI. Single-shot EPI is a technique of k-space filling using a single 180° RF pulse to fill all of k-space in a single TR. This is accomplished by rapidly alternating the frequency encode (readout) gradient from positive to negative and applying phase 'blips' to rapidly select the phase coordinate in k-space (Gallagher et al., 2012). The rapidly alternating frequency encode gradient stimulates

smaller echoes that can then be measured. The series of echoes in a single TR are typically called a *train*. A typical PGSE EPI sequence is shown in Figure 9.

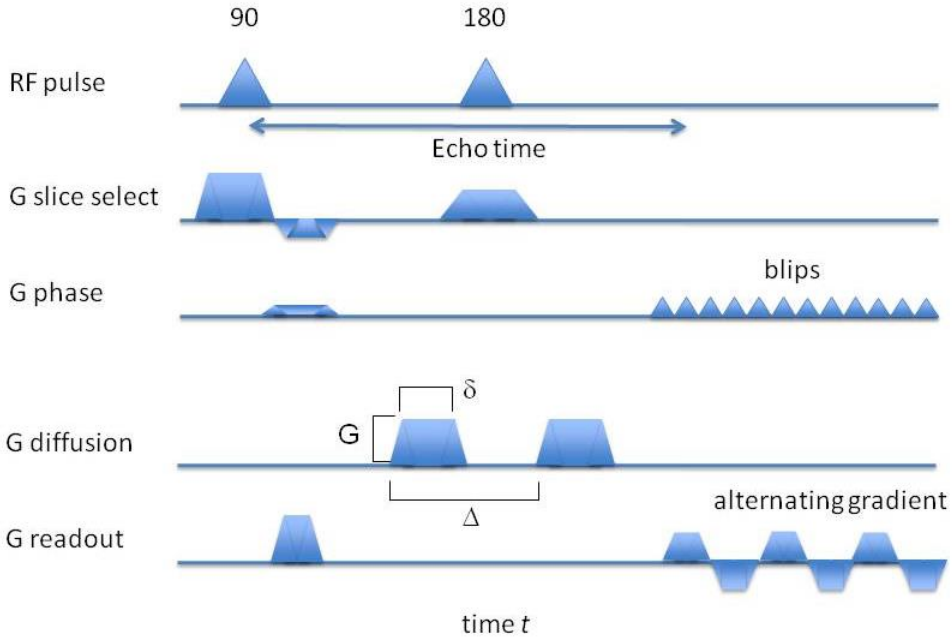

Figure 9: Typical DWI EPI sequence. *Reprinted with permission from Gallagher, T. A., Alexander, A. L., & Field, A. S. (2012). Diffusion Tensor Magnetic Resonance Imaging: Physical Principles. In S. H. Faro, F. B. Mohamed, M. Law, & J. T. Ulmer (Eds.), Functional Neuroradiology: Principles and Clinical Applications (pp. 709-729). Springer US.*

The above descriptions of diffusion imaging have been rather fantastical or idealistic in that they have failed to address some of the common challenges and pitfalls of diffusion imaging. In short, diffusion imaging is not easy, particularly with regards to motion. The heavyweights of *T2**-weighted imaging (diffusion, perfusion, and functional MRI) all rely on a common attribute: the motion of particles around the field-of-view (FOV) alter the local magnetic field in a way that is measurable. A key requirement of these methods, therefore, is a stationary subject, which is almost impossible. Even the most well-behaved subjects will continue to breathe, maintain peristalsis, and pump blood through their veins; all of these may cause motion that can corrupt signal. In diffusion imaging, gross subject motion, such as pitch, yaw, or roll of the subject's head, results in signal voids, blurring, and/or aliasing. These signal voids manifest as artificially

increased diffusion (more isotropic) because signal intensity and the diffusion coefficient are inversely related. There are ways to mitigate motion artifacts, such as padding the subjects head, cardiac and respiratory gating, and developing faster acquisition schema. EPI is one such method used to reduce imaging times, which leads to a decreased chance of subject motion during an acquisition.

EPI cannot eliminate motion, only decrease its likelihood. Further, EPI is extremely sensitive to field inhomogeneities, particularly in the phase encode direction. The field inhomogeneities can alter the resonant frequency of tissue, particularly near sharp magnetic susceptibility transitions, e.g., above the sinuses. The change in frequency will effectively result in a chemical shift artifact, wherein tissue of one type will be artificially mapped as a different tissue elsewhere in the image. This can lead to bright or dark bands near the tissue boundary (Jezzard & Balaban, 1995). EPI distortions may also appear as stretching or truncation (signal pile up appearing as a bright band), as well as aliasing (Reeder et al., 1997). EPI distortions are shown in the fourth panel of Figure 10, labelled as *Susceptibility-induced Distortions*. One method for correcting EPI distortions is to collect an image of the $\mathbf{B_0}$ field to measure the degree of inhomogeneity, and subsequently unwarping the EPI images. Note that lost signal cannot be recovered with conventional methods (Jezzard & Balaban, 1995). Because of the wide bandwidth in the frequency encode (~100kHz), the EPI distortions are minimized, and EPI distortions typically occur along the phase encode, due to the small bandwidth in that direction (~1kHz) (Jezzard & Balaban, 1995).

For volume-to-volume and within volume motion, panels 1 and 2 of Figure 10, respectively, these artifacts can often be corrected by aligning to an image without motion. In DTI, this motion-free image is typically chosen from the set of b_0 images, which are T2-

weighted. The benefits of selecting the b_0 image is twofold: 1) it corrects for motion and 2) because the T2-weighted image is collected with the T2* effects removed, the field inhomogeneities are suppressed and aligning to this image can help correct EPI distortions.

The last artifact that will be discussed arises from the presence of *eddy currents*, which derive their name from eddies in a river. Think of the large $\mathbf{B}_0$ field as a river with a strong flow or flux, eddy currents form in the magnetic field just as eddies form in a flowing river. The physical reason for this phenomenon is Faraday's Law of Induction. The rapidly changing gradients in EPI produce a magnetic flux that results in eddy currents in the scanner electronics, which alter the main magnetic field and the gradients. Eddy currents typically lead to shearing, scaling, and translation of the image, which can be corrected for by modeling the effect of the eddy currents on the data and spatial normalization to the b_0 image (Andersson et al., 2016; Graham et al., 2016; Spees et al., 2011). Example eddy current distortions are shown in the third panel of Figure 10.

2.9. R1 Structural Imaging

Along with diffusion imaging, Chapter 6 of this work uses R1 relaxometry, which is the longitudinal relaxation rate. R1 has been shown to be a surrogate measure of myelin content, although, not exclusively, as iron and axon density can affect R1 (Alexander et al., 2011; Lazari & Lipp, 2021). R1(s^{-1}) maps are derived using quantitative T1 maps, which differ from T1-*weighted* images. T1-weighted images are unitless and are produced by using short TRs and TEs. In relaxometry, T1 maps are in units of time, typically seconds or milliseconds and are generated by repeatedly sampling the exponential recovery of the T1 signal at multiple points for multiple flip angles. An exponential model is then fitted and the T1 value calculated. R1 is simply the inverse of T1.

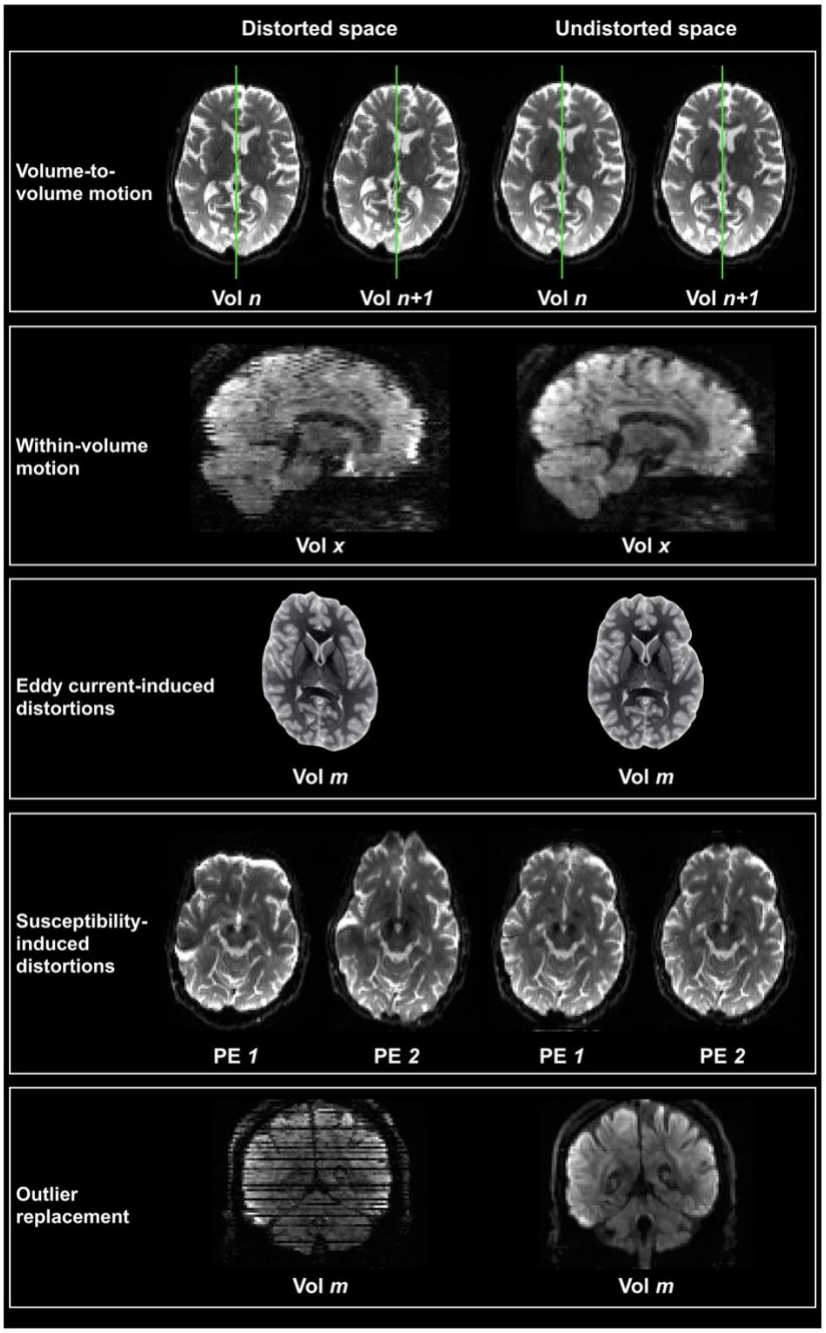

Figure 10: Overview of the EDDY framework for distortions and motion correction. Raw data in distorted space are brought to artefact-free undistorted space. Motion parameters are estimated and used to correct both between and within volumes displacement. Both eddy currents and susceptibility-induced off resonance fields are used to correct for geometric distortions. Using a Gaussian process to describe the 4D data, outlier slices (i.e., slices affected by severe signal dropout) are detected and replaced with their predictions. To illustrate the effects of eddy currents-induced distortions, T2 weighted images have been manually skewed. Reprinted with open-access permissions from Bastiani, M., Cottaar, M., Fitzgibbon, S. P., Suri, S., Alfaro-Almagro, F., Sotiropoulos, S. N., Jbabdi, S., & Andersson, J. L. R. (2019, 2019/01/01/). Automated quality control for within and between studies diffusion MRI data using a non-parametric framework for movement and distortion correction. Neuroimage, 184, 801-812. https://doi.org/https://doiorg/10.1016/j.neuroimage.2018.09.073

3. Chapter 2: Neuroanatomical and Physiological Background

3.1. White Matter

The bulk of the preceding chapter was spent deriving and exploring the physical phenomena that give rise to a diffusion signal observable with MRI. This chapter will explore the biological origins of those signals and the physiological and pathophysiological processes that may affect the observed signal.

Conveniently for MRI researchers, humans are mostly water. Around 60% of the total body (Popkin et al., 2010) and upwards of 75% of the brain are water (Zhang et al., 2018). Consequently, humans have an abundance of hydrogen atoms, and more importantly, an abundance of hydrogen nuclei, i.e., protons. As discussed above, MRI is reliant on the manipulation of the spin resonance of lots of protons to derive a signal. The abundance of water in the brain makes it ideal for MRI experiments, particularly of white matter.

White matter is comprised of fiber bundles of axons, which are themselves projections of neurons from the cell body. These fibers carry action potentials from neuron to neuron, as well as to innervate the rest of the body. There are numerous analogies for the function of white matter within the brain: the roads (white matter) connecting cities (gray matter); however, the most useful picture is that of a wire. A wire may carry a current from one part of a circuit to another, and the thicker the wire, the more efficiently the current may be carried. This is also true of white matter. The brain will selectively reinforce connections within the brain that are commonly used, essentially leading to a "better wire."

Further, a wire may be either insulated or uninsulated, which is also true of white matter. Myelin is a fatty, dialectic material that primarily serves to insulate axons. Within the cortex, where connections are typically very short, the axons remain unmyelinated. Normal white

matter servicing interlobular cortico-cortical, cortico-subcortical, cortico-cerebellar, or corticospinal connections is myelinated. Myelin forms a sheath around white matter between the nodes of Ranvier. The nodes of Ranvier are rich in ion channels, which function as signal amplifiers and help to propagate the action potential. An axon potential will be emitted from the cell body and travel through the axon. The myelin will insulate the emitted current, which is amplified or boosted at each node of Ranvier, before the signal arrives at the axon terminals. White matter derives its name from the white appearance of densely group, myelinated fibers which are lighter in appearance than gray matter.

WM typically derives its function from the regions it connects, and tracts are separated into three classes: projection fibers, association fibers, and commissural fibers. The projection fibers are comprised of the corticospinal (CST), corticopontine, and corticobulbar tracts and facilitate voluntary motor control (Catani & Thiebaut de Schotten, 2012; Ramos-Fresnedo et al., 2019). The CST is the projection fiber of most concern for this work. The CST is the efferent pathway from the cortex to the spine and the rest of the body. The fibers that form the CST originate in the primary motor, premotor, supplementary motor, somatosensory, and cingulate cortices. The fibers are somatotopically arranged with the fibers innervating the face, head, and neck comprising the outermost layer, which decussate in the cerebral peduncle and are called the geniculate fibers because they pass through the genu of the internal capsule. Medial to the geniculate fibers are the fibers innervating the upper arms and torso, followed by the most medial fibers which innervate the lower limbs. These fibers decussate at the pyramids, meaning that a

given side of the cortex controls the opposite side of the body (Ramos-Fresnedo et al., 2019). The CST highlights the complex arrangement and function of white matter in just a single tract.

The Association Fibers are large white matter tracts that facilitate ipsilateral communication between lobes of the brain. The Association Fibers include the uncinate fasciculus (frontal to temporal lobe), superior longitudinal fasciculus (SLF; occipital to frontal and temporal lobes), inferior longitudinal fasciculus (ILF; occipital to temporal lobe), and the cingulum (cingulate gyrus to parahippocampal gyrus) (Gupta, 2017). The Association Fibers are heavily recruited in a variety of functions. The uncinate fasciculus is considered to be part of the limbic system and is believed to be involved in associative and episodic memory, social-emotional functions, and language (Von Der Heide et al., 2013). The SLF is implicated in visuospatial attention, motor control, language, auditory processing, and reading (Nakajima et al., 2020). The ILF is involved in facial and object recognition, reading, visual comprehension, and semantic processing (Herbet et al., 2018). The cingulum is involved in episodic memory, executive function, working memory, emotion, and pain (Bubb et al., 2018). Clearly the Association Fibers play diverse and important roles in memory, attention, reasoning, and executive function which will be of importance to this work and are discussed in Chapters 4, 5, and 6.

The Commissural Fibers connect corresponding regions from each hemisphere and include the corpus callosum and the anterior, posterior, habenular, hypothalamic, hippocampal, and cerebellar commissures (Gupta, 2017). The corpus callosum and anterior commissure are the largest and most studied commissural tracts. These fibers play several roles, but are particularly

implicated in higher order cognition, emotion, taste, and pain (Catani & Thiebaut de Schotten, 2012; Ramos-Fresnedo et al., 2019).

The last tracts of interest to this work are the thalamic radiations or thalamocortical fibers (there are also corticothalamic fibers). All inbound information, excluding olfaction, must pass through the thalamus before passing to the cortex (George & J, 2021). The thalamus serves as a relay center, among other functions, to direct incoming signals to the necessary processing centers in the cortex. This makes these fibers particularly important for auditory, motor, visual, and somatosensory processing (George & J, 2021).

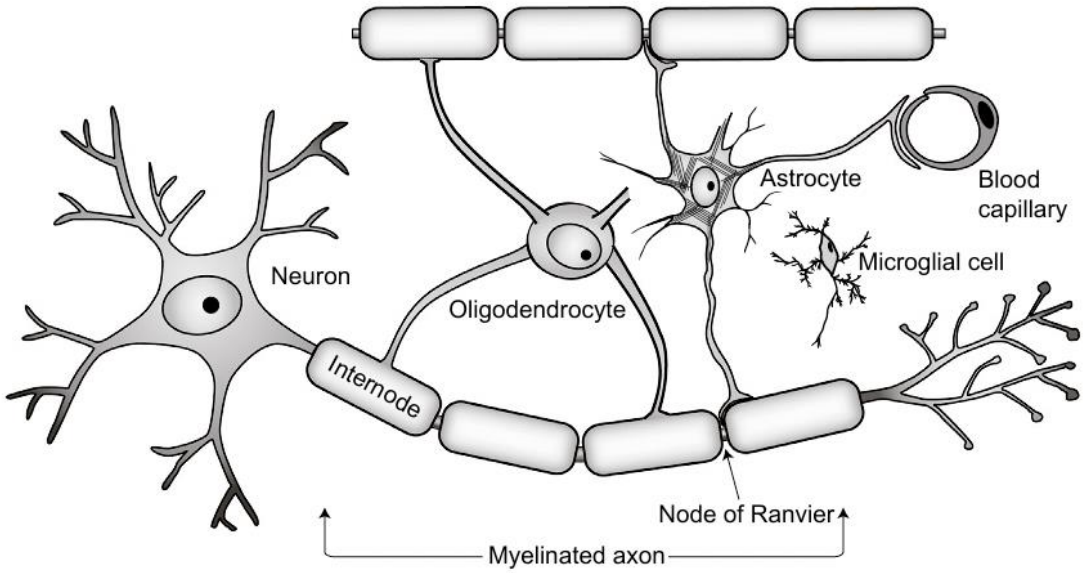

Figure 11: Structure of a neuron featuring a myelinated axon. Reprinted with permission from Edgar, J. M., & Griffiths, I. R. (2014). Chapter 7 - White Matter Structure: A Microscopist's View. In H. Johansen-Berg & T. E. J. Behrens (Eds.), Diffusion MRI (Second Edition) *(pp. 127-153). Academic Press.*

The above exploration of the organization and function of large bundles of white matter fibers has been a useful exercise to illustrate the complexity and importance of white matter in the brain. The discussion will now turn to the microscopic structure and physiology of individual

axons and the network of support cells that nourish, protect, and prune connections within the brain. Figure 11 depicts a typical nerve cell with a myelinated axon. Observe that the nucleus of the cell is surrounded by what look like small axons. These structures are called dendrites and together form what is known as the dendritic arbor of the neuron and facilitate both local communication with nearby neurons, but also synapse with the axon terminals of other neurons to receive and process information. To the right, the axon projects outwards and is sheathed in myelin as described above. There are several support cells, or *glia*, depicted in Figure 11, namely oligodendrocytes, astrocytes, and microglia. Each of these cells provides a specialized form of support to the axon.

Oligodendrocytes are myelinating cells and produce the myelin sheath that encapsulates the axon and promote the production of ion channels at the nodes of Ranvier to encourage saltatory nerve conduction, i.e., boost the transmitted signal (Bradl & Lassmann, 2010). Figure 12 shows a detailed rendering of the saltatory conduction process; observe that the insulated signal from the internode, myelinated axon portion enters the node of Ranvier, is repolarized, and amplified before entering the next internode segment. Oligodendrocytes selectively encapsulate axons greater than 2 microns in diameter, although the exact mechanism of this selection is unknown. Further, frequent use of an axon signals increased activity to the oligodendrocytes which will apply more layers to the myelin sheath (Bradl & Lassmann, 2010). This phenomenon will be important to explore and is expanded upon in the neuroplasticity section below.

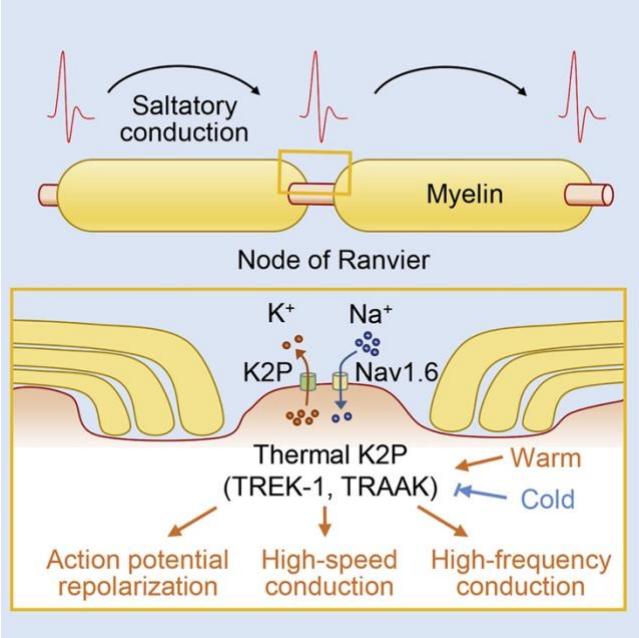

Figure 12: Detail of saltatory nerve conduction. Reprinted with permission from Kanda, H., Ling, J., Tonomura, S., Noguchi, K., Matalon, S., & Gu, J. G. (2019, 2019/12/04/). TREK-1 and TRAAK Are Principal K+ Channels at the Nodes of Ranvier for Rapid Action Potential Conduction on Mammalian Myelinated Afferent Nerves. Neuron, 104(5), 960-971.e967.

The next support cell shown in Figure 11 is an astrocyte. Astrocytes perform several tasks depending on location and the developmental stage of the brain. Astrocytes play a role in neurogenesis and synaptogenesis, as well as regulating homeostasis within the nerve cells, providing nourishment, and facilitating blood-brain barrier permeability when needed (Siracusa et al., 2019).

The last support cell shown in Figure 11 is a microglial cell. For clarity, it is important to note that all microglial cells (microglia) are glial cells, but not all glia are microglia. Microglia play an important role in the central nervous system (CNS), primarily in several immune response phenotypes. Microglia can behave as macrophages and are responsible for the inflammatory response to foreign bodies via the production of proinflammatory cytokines, such as interleukin (IL)-1β, IL-6, and tumor necrosis factor-α, reactive oxygen species, and reactive nitrogen species (Wang et al., 2015). Alternatively, microglia may also act in an anti-

inflammatory behavior by producing and releasing trophic factors, such as brain-derived neurotrophic factor (BDNF) (Bachiller et al., 2018; Wang et al., 2015). Microglia have a complex role in the CNS, not only in the immune response as described above, but also in the homeostasis, cleaning, pruning of synapses, and signaling for synaptic growth (Bachiller et al., 2018).

Not every connection in the brain is useful or may be temporarily useful but diminish in importance over time. The brain has a finite space to work with, the volume of the skull, and maintaining unused connections can displace, impede, or interfere with the creation of new or maintenance of useful connections. To be blunt, the brain runs a tight ship, meaning that if a connection is not useful, the brain has mechanisms in place to remove the connection. The brain will also seek to generate new synapses and reinforce existing connections that optimize performance. The bulk of the work for both the generation, reinforcement, and pruning of connections is achieved by glia. Microglia observing a no longer used pathway, will begin to produce an inflammatory and phagocytic response to prune the connection. Conversely, frequent use of a connection will signal for increased blood flow from astrocytes, increased myelin production from oligodendrocytes, and the production of trophic factors by microglia (Fields et al., 2013; Innes et al., 2019; Wu et al., 2015). These responses signal for higher myelin sheath turnover and growth of the axon. Along with long-term potentiation (LTP) and long-term depression (LTD), this functionality forms the basis of neuroplasticity and the underpinnings of learning discussed below (Abraham et al., 2019). The dysregulation of these processes is also highly implicated in neurodegeneration, which will be explored in its own section.

MRI has not yet achieved the resolution required for imaging individual glial cells or synaptic changes *in-vivo*. Such imaging would require resolution on the order of a micron, which

would only be possible with extremely ultrahigh field strengths and impractically long scan times. The effects of ultrahigh field strengths on humans are not well understood, and extremely long scan times are not practical without the use of anesthesia or at extreme discomfort to the subject. To this end, it is not possible to image support cells in the brain *in-vivo*; however, the chorus of processes undertaken by microglia have useful effects – they may displace or otherwise affect the diffusion of water in the axons they support, which can be detected with diffusion MRI.

The bulk of the remaining chapters of this work deal largely with processes intimately related to glial cell function and white matter as a whole: neuroplasticity and neurodegeneration. Because the diffusion modeling methods described in Chapter 2 are not biologically derived, but rather physical models applied to biological data, it would be an overstatement to derive conclusive biological meaning from imaging data alone; however, in this work, we will seek to explore the changes of diffusion imaging measures in two cohorts. The first set of analyses will explore diffusion associations with cognitive decline and amyloid burden in a Down syndrome (DS) population, which is genetically predisposed to develop Alzheimer's Dementia. In these analyses, we will seek to bridge the cognitive, imaging, and dementia literature in the largely understudied DS population. The second set of analyses will seek to explore the sensitivity of diffusion measures to short-term (~hours) and long-term (~weeks) neuroplastic processes involved in videogame training in typically developing college students.

3.2. Down Syndrome

Down Syndrome (DS) is a genetic disorder involving chromosome 21. Trisomy, the presence of an extra entire or partial copy, of chromosome 21 accounts for 95% of DS cases, while the remaining 5% are due to Robertsonian Translocation (mosaicism), which results in the increased dosage of gene products associated with chromosome 21 (Neale et al., 2018).

DS is associated with physical growth delays, intellectual disabilities, and characteristic facial features. There are many neuroanatomical abnormalities in DS. People with DS are brachycephalic and have decreased total brain volume and smaller frontal and temporal lobes and cerebella (Lott, 2012). Further, the superior temporal gyrus is reduced and the parahippocampal gyrus is in enlarged (Lott, 2012). Other neuroanatomical distinctions in DS include increased frontal and occipitoparietal cortices, thinner motor cortices, smaller hippocampi, and larger putamen volumes relative to the general population (Lott, 2012). DS brains also age more rapidly than the general populace with an adjusted brain-predicted age difference increase of 7.7 years in DS individuals relative to the general public (Cole et al., 2017).

The DS-AD neuroimaging literature may be one of the few disciplines where a review of every single article could feasibly be cited in a literature review, as there are only 11 PET and 9 MRI studies in this population (Neale et al., 2018).

3.3. Alzheimer's Disease

Alzheimer's disease (AD) is a form of dementia, largely dominated by cognitive decline and eventual death. An excellent overview of the forms of dementia is contained in a review by Ferencz and Gerritsen (2015) summarized with permission in this paragraph. The other types of dementia include Lewy body dementia (LBD), frontotemporal dementia (FTD), and vascular dementia (VaD). LBD differs from AD in that it is linked to the accumulation of synuclein plaques or Lewy bodies. LBD encompasses two diseases, dementia with Lewy bodies and Parkinson's disease dementia, which become indistinguishable with disease progression. LBD is associated with both cognitive and behavioral infarcts, as well as motor symptoms observed in Parkinson's disease. FTD is a heterogeneous grouping of disorders linked to frontotemporal degeneration. Lastly, VaD, or cerebral small vascular disease, is dementia derived from micro-strokes and ischemia. VaD symptoms are largely dependent on the region of vascular damage. It is also possible for people to have mixed dementia, wherein someone has multiple types of dementia, e.g., AD and vascular dementia (Ferencz & Gerritsen, 2015). This work will focus on AD, particularly in a Down syndrome cohort, which is largely protected against cerebral vascular disease (Head et al., 2017).

Alois Alzheimer, a neuroanatomist and psychiatrist from Germany, is credited with the discovery and first reporting of an AD case study at the 37th Meeting of South-West German Psychiatrists in 1906 (Hippius & Neundörfer, 2003). Alzheimer described a curious case study of a 50-year-old woman with paranoia, progressive sleep problems, memory impairment, confusion, and aggressiveness. Histology performed by Alzheimer revealed accumulated plaques and neurofibrillary tangles (NFT) in the patient's brain as well as severe atrophy (Hippius &

Neundörfer, 2003). These senile plaques and NFTs are discussed in more detail below and are the most prominent pathophysiological indicator of AD.

AD would not become a household name until the late 1970s, when it was mentioned on US vitality reports for the first time and recognized as the same disease as senile dementia (Ballard et al., 2011). Further, it was important for the medical community to recognize that AD symptoms are atypical and should not be consider reflective of normal aging. Since this time, AD and other dementias have gained enormous research traction, but a cure has not been discovered. Epidemiologically, AD accounts for almost 75% (Qiu et al., 2009) of global dementia cases and over 36 million people are affected by AD (Prince et al., 2013). Age and genetic predisposition are the leading, known causes of AD, and with the population of people aged 65+ projected to exceed 1 billion by 2030 cases are only going to increase (United Nations & Affairs, 2002). With a global prevalence of 5-7% for people 60+ , there are projected to be 65.7 million cases of AD in 2030 and 115.4 million by 2050 (Prince et al., 2013). Figure 13 shows the prevalence of AD per age group in several regions; it is remarkable that almost 1 in 3 people over 90 in the US have AD (Qiu et al., 2009).

AD is typically divided into two subtypes, early onset (EOAD) and late onset (LOAD) (Bateman et al., 2011). EOAD typically includes further subtyping, such as autosomal dominant and familial AD. LOAD may include familial AD inheritance, as well as sporadic AD (the most common type of AD), which are mostly linked to the apolipoprotein E4 (ApoE4) allele (Bekris et al., 2010). Autosomal dominant AD (ADAD), familial AD, and early onset AD (EOAD) involve a genetic component that contributes to an increase risk of AD onset. For ADAD this includes mutations of genes coding for amyloid precursor protein (APP), presenilin 1, or presenilin 2, which around 50% of carriers will develop EOAD at age 30-50 (Bateman et al., 2011). While

ADAD accounts for less than 1% of AD cases, it has produced a genetically identifiable population with high-risk of AD development that has been useful in the study of preclinical AD development. This work will focus on a population with an increased production of APP due to genetic mutation (trisomy) in Down syndrome, which makes the population similar to ADAD populations. The APP processing pathways are discussed below.

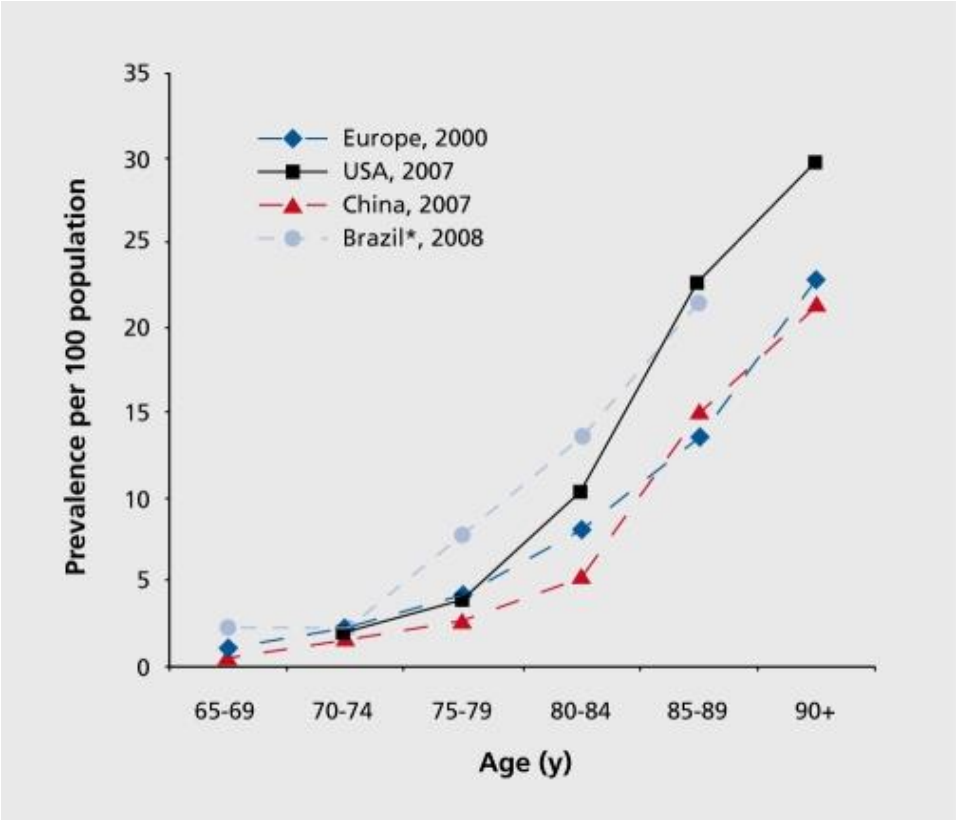

*Figure 13: Age-specific prevalence of Alzheimer's disease (per 100 population) across continents and countries. *, prevalence of all types of dementia. Reprinted with permission from Qiu, C., Kivipelto, M., & von Strauss, E. (2009). Epidemiology of Alzheimer's disease: occurrence, determinants, and strategies toward intervention.* Dialogues in clinical neuroscience, 11*(2), 111-128.*

The pathophysiological hallmarks of Alzheimer's Disease are the extracellular accumulation of amyloid-β (Aβ) peptides (senile plaques) and intracellular neurofibrillary tangles (NFTs) comprised of hyperphosphorylated tau proteins in neurons, which are believed to

drive the neurodegeneration and necrosis associated with cognitive decline and eventual death in AD.

The development of senile plaques has been linked to the proteolysis of APP. The two proteolytic pathways for APP cleavage at cell membranes are shown in Figure 14. The left portion of the figure shows the non-amyloidogenic (non-plaque forming) pathway. In this pathway, APP is first cleaved by α-secretase in the β-amyloid region (red) to produce releases soluble APPα and C-terminal fragment-α (CTFα). CTFα is further cleaved by γ-secretase to produce P3 peptide and the APP intracellular domain (AICD). In the amyloidogenic pathway, APP undergoes posttranslational proteolysis by β-secretase to produce soluble APPβ and C-terminal fragment-β (CTF-β); CTF-β is further cleaved by γ-secretase to generate the hydrophobic β-amyloid (Aβ) peptides and AICD in the extracellular domain (Zhang, Ma, et al., 2012). APP proteolysis is normally highly regulated (Chow et al., 2010); however, in AD, this process is dysregulated and amassed Aβ becomes insoluble and is not effectively cleared, forming amyloid plaques (Vlassenko et al., 2012).

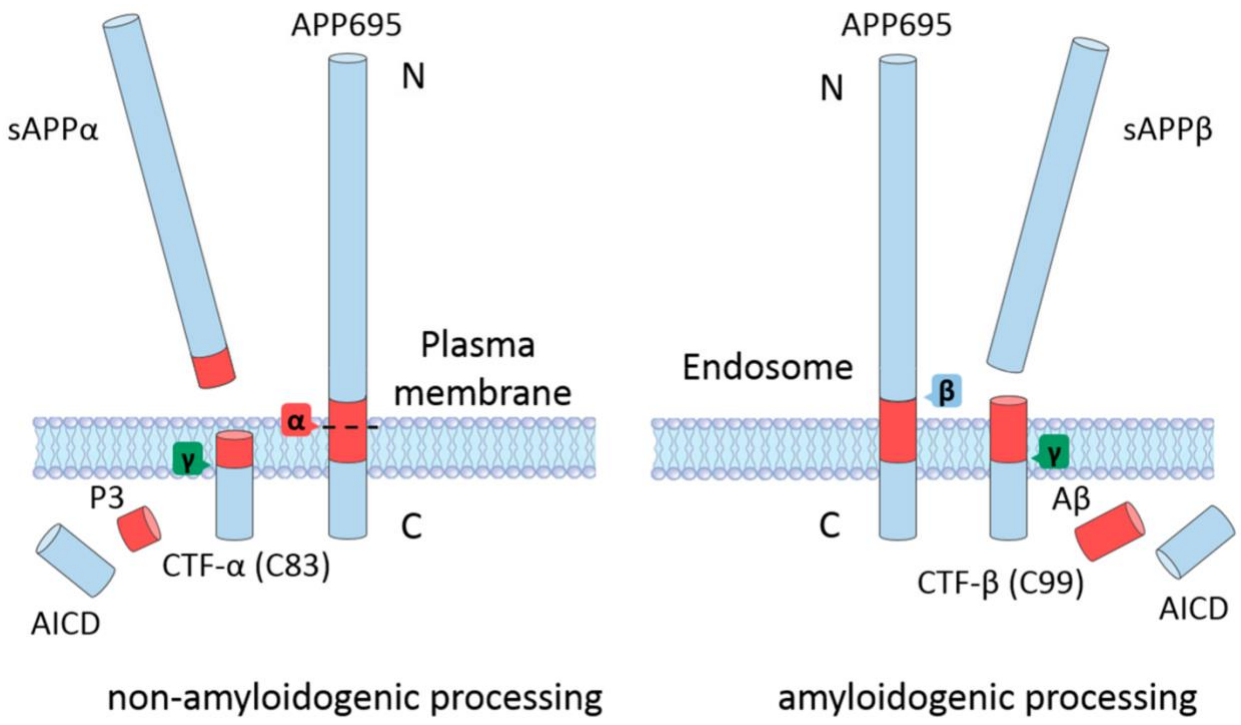

Figure 14: Proteolytic pathways for APP cleavage. Reprinted with permission from Zhang, T., Chen, D., & Lee, T. H. (2020). Phosphorylation Signaling in APP Processing in Alzheimer's Disease. International Journal of Molecular Sciences, 21(1), 209.

The importance of Aβ in the development of AD has made it a focus of the AD research community and has given rise to the *Amyloid Cascade Hypothesis*, which states that the change in Aβ metabolism and subsequent accumulation of Aβ plaques causes a cascade of effects that lead to AD pathology, cognitive decline, and neurodegeneration (Barage & Sonawane, 2015; Hardy & Higgins, 1992). Figure 15 shows a graphical representation of the chain of events in the Amyloid Cascade Hypothesis. First, alterations in the Aβ metabolism causes the buildup of Aβ42. Next, alterations of synaptic response occur followed by an inflammatory response from microglia and astrocytes. Concurrently, Aβ plaques begin to form leading to progressive cellular and axonal damage. Ultimately leading to aberrant oligomerization of tau proteins and the formation of NFTs (Barage & Sonawane, 2015; Haass & Selkoe, 2007; Hardy & Higgins, 1992)

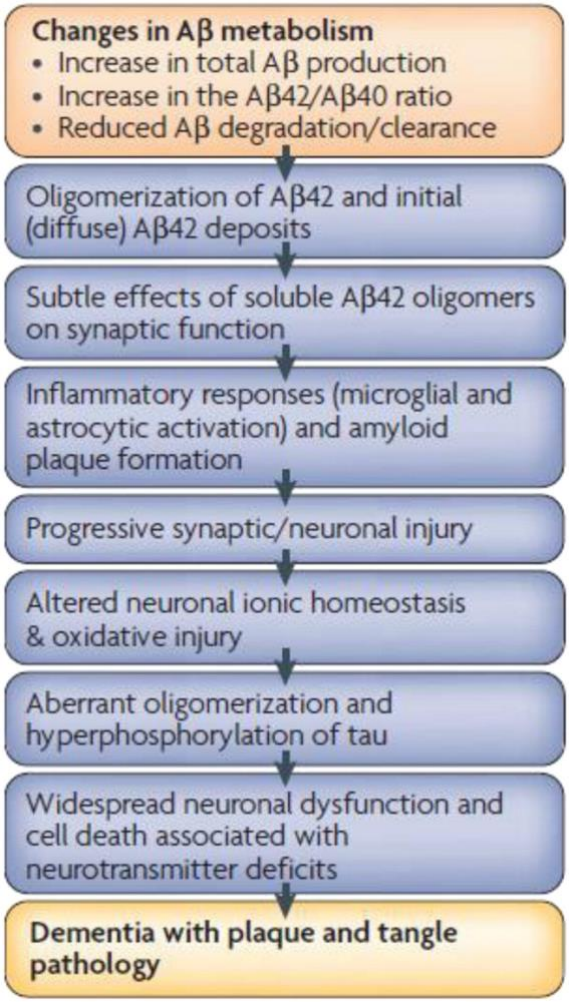

Figure 15: Graphical depiction of the Amyloid Cascade Hypothesis. Reprinted with permission from Haass, C., & Selkoe, D. J. (2007). Soluble protein oligomers in neurodegeneration: lessons from the Alzheimer's amyloid β-peptide. Nature reviews Molecular cell biology, 8(2), 101-112.

The underlying physiology that results in amyloid accumulation and neuronal death is not fully understood; however, one hypothesis suggests the involvement of glia (Sokolowski & Mandell, 2011). People with AD or elevated Aβ deposits have been shown to have increased neuroinflammation and gliosis, which involves microglia and astrocyte swelling (Beach et al., 1989; Itagaki et al., 1989). This swelling may be an immune response elucidated by the presence of Aβ with macrophages and microglia reacting to contain the Aβ plaque; however, it is unknown whether this response is detrimental or protective (but insufficient) in purpose (Chow

et al., 2010; Sokolowski & Mandell, 2011). Regardless, the prolonged neuroinflammatory response has been shown to be neurotoxic and facilitated by the release of proinflammatory cytokines/chemokines and neurotoxins (Chow et al. 2010).

Though AD is typically seen as gray matter disease, as Aβ plaques and NFTs accumulate in gray matter, this does not mean that white matter is unaffected in AD. Aβ accumulation in WM is exceedingly rare; however, WM degeneration and atrophy are hallmarks of the disease and have been shown to be linked to the progression of AD (Nasrabady et al., 2018). The leading argument for this WM loss is Wallerian degeneration, wherein the damage or death of the connecting neurons kills the axon as well (De Simone et al., 2005; Nasrabady et al., 2018). A comparison of a healthy and severe AD brain is shown in Figure 16. Note not only the severe gray matter atrophy and ventriculomegaly, but also the severe white matter degeneration, as well.

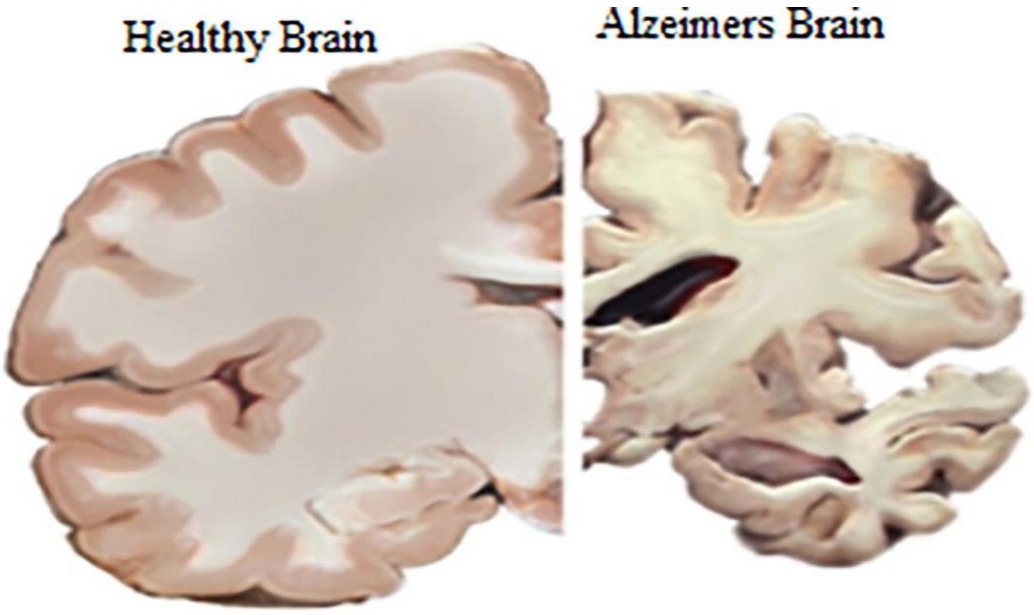

Figure 16: Comparison of normal (left) and severe Alzheimer's Disease pathology (right). Reprinted with permission (Kishore et al., 2020)

As stated above, Wallerian degeneration is seen as the most likely culprit for axonal loss; however, emerging evidence supports the involvement of 1) microglia activation and

inflammation or phagocytic malfunction (Sokolowski & Mandell, 2011) and 2) oligodendrocyte malfunction or death resulting in demyelination via neuropathologic retrogenesis (Nasrabady et al., 2018). Figure 17 shows a modification of the Amyloid Cascade Hypothesis to include the effects of glial cell involvement. Observe the presence of Aβ is recognized by astrocytes and microglia, which further elicits a microglial response in one of two pathways anti-inflammatory or inflammatory, of which, the inflammatory response is neurotoxic (Sokolowski & Mandell, 2011).

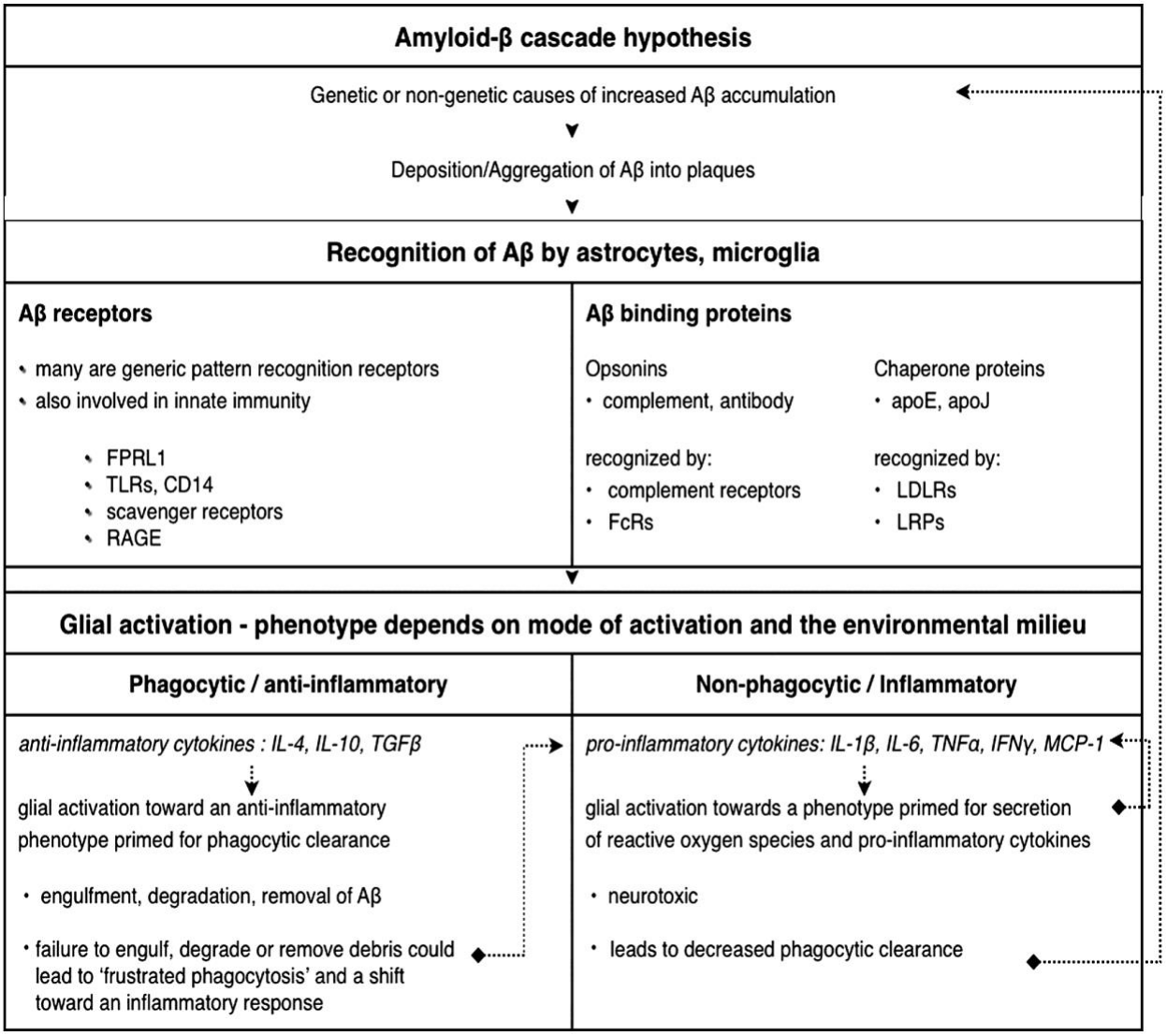

Figure 17: Sequence of events connecting the amyloid cascade hypothesis to putative glial cell responses. Reprinted with permission from Sokolowski, J. D., & Mandell, J. W. (2011, Apr). Phagocytic clearance in neurodegeneration. Am J Pathol, 178*(4), 1416-1428.*

With the amyloid cascade hypothesis in mind, it would be good to have an idea of how quantifiable changes in the brain progress with disease status. This has made the detection and tracking of biomarkers, i.e., imaging, histopathological, or genetic indicators of disease, of great interest in AD research. Jack et al. (2010) proposed an evolution of AD biomarkers governed by the amyloid cascade hypothesis that showed the transition of biomarkers from normal to abnormal versus disease stage. These curves became known as *Jack curves* and Figure 18 shows

the biomarker and symptom evolution versus disease stage. Note that Aβ accumulates largely asymptomatically in the cognitively normal brain before significant tauopathy occurs, which leads to brain atrophy and memory decline associated with mild cognitive impairment (MCI). As tau continues to increase, so do brain atrophy and memory degradation. Finally, in demented individuals, clinical function across all cognitive domains declines rapidly (Jack et al., 2010).

With the introduction of MCI, it is important to review different methods for staging of AD. MCI is a syndrome characterized by cognitive decline greater than that expected with normal aging and a person's level of education, but without significant interference in a person's daily life (Gauthier et al., 2006). MCI may be thought of as a risk state for dementia, and the amnesic form of MCI is associated with higher risk of AD development and may represent the prodromal stage of AD (Gauthier et al., 2006).

Two scales typically used in the clinical assessment of AD are the Global Deterioration Scale (GDS) (Reisberg et al., 1982) and Clinical Dementia Rating (CDR) (Hughes et al., 1982). The GDS is a numeric scale from 1 to 7, with a GDS of 1 representing no cognitive decline or memory deficits and a GDS of 7 representing severe dementia. A GDS of 2 represents cognitive decline within the range expected with normal aging. MCI is associated with a GDS of 3, where the first major deficits may be observed, but without large impact on daily life. Symptoms of MCI may include getting lost in new environments, losing objects of value, difficulty with reading comprehension and retention, and difficulty remembering names upon introduction to new people. The CDR ranges from 0 to 3, where a CDR of 0 is cognitively normal and a CDR of 3 represents severe dementia. A CDR of 0.5 is similar to a GDS of 2 indicating cognitive decline associated with normal aging. A CDR of 1 indicates MCI, equivalent to a GDS of 3.

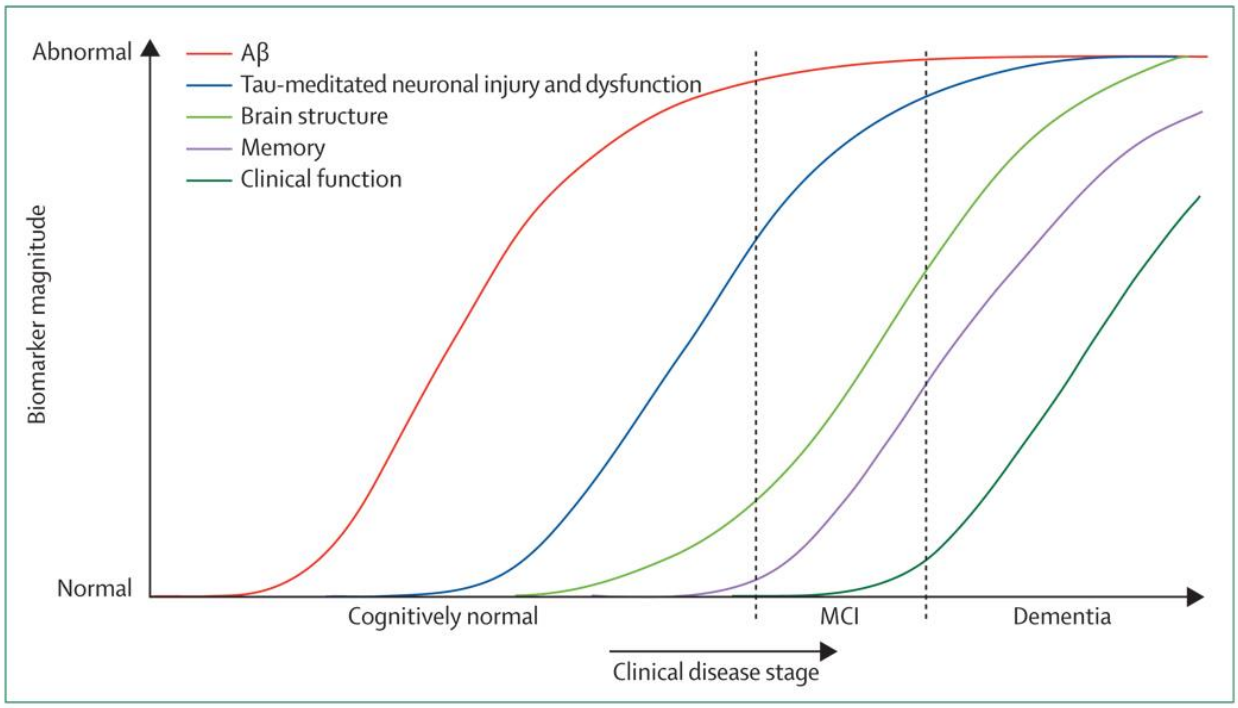

Figure 18: Dynamic biomarkers of the Alzheimer's pathological cascade. Reproduced with permission from Jack, C. R., Jr., Knopman, D. S., Jagust, W. J., Shaw, L. M., Aisen, P. S., Weiner, M. W., Petersen, R. C., & Trojanowski, J. Q. (2010). Hypothetical model of dynamic biomarkers of the Alzheimer's pathological cascade. The Lancet. Neurology, 9*(1), 119-128.*

The GDS and CDR are clinical determinations based on cognitive assessment. There are also post-mortem staging methods based on immunohistochemistry. Famously, Braak and Braak (1991) introduced a post-mortem pathology assessment of NFT using the silver-based method of (Campbell et al., 1987). Braak and Braak (1991) showed that the earliest sites of accumulated tau began in the transentorhinal region (part of the temporal mesocortex) and constituted Braak stage I (Braak et al., 2006; Braak & Braak, 1991). Stage II involves the pre-$\boldsymbol{\alpha}$ layer of the entorhinal cortex with intrusion into the hippocampus. Stage III involves the worsening of the hippocampus, the parahippocampus, and the occipito-temporal gyrus (Braak & Braak, 1991). In stage IV, severe NFT accumulation begins in the MTL and insula.; Stage V involves further accumulation in the occipital lobe (Braak et al., 2006; Braak & Braak, 1991). Stage VI involves

changes throughout the sensory association and primary areas of the occipital lobe (Braak et al., 2006; Braak & Braak, 1991).

The Braak staging method is based on NFT intrusions. Turning to the imaging of Aβ, a method was published by Thal et al. (2002), which Heiko Braak was the lead author, that once more used the silver staining method of (Campbell et al., 1987). Thal et al. (2002) divided Aβ accumulation into five stages. In the first stage, Aβ is diffuse throughout the neocortex, and the second stage sees intrusion into the allocortex (hippocampus and olfactory regions) (Thal et al., 2002). Stage 3 is characterized by Aβ accumulation in the diencephalon (thalamus, hypothalamus, epithalamus, and pituitary gland), striatum, and the basal forebrain (Thal et al., 2002. Stages 4 and 5 involved Aβ intrusion into the brainstem and cerebellum, respectively (Thal et al., 2002). Thal et al. (2002) further noted that all non-AD brains were classified as stage 1, 2, or 3, and all AD brains were either stage 3, 4, or 5.

3.4. Imaging Alzheimer's Disease

The use of neuroimaging methods for characterizing and diagnosing AD is not new. Positron emission tomography (PET) studies of AD began in the early 1980s (Ferris et al., 1980) and MRI followed shortly thereafter (Leys et al., 1990; McGeer et al., 1986; McGeer, 1986). While genetic and CSF markers are also important in the diagnosis of AD, these techniques are not employed within this work and are left to the reader for an exhaustive review. Further, it should be noted that biomarkers in AD research are typically categorized according to the AT(N) (amyloid -> tau -> neurodegeneration) framework proposed by Jack et al. (2018). This work exams amyloid (A) and neurodegeneration (N) biomarkers.

Early MRI studies of AD were constrained to structural imaging due to the technology of the time. This led to the frequent use of volumetry measures or voxel-based morphometry, which

is used to characterize changes in brain volumes. As there is a great deal of atrophy in AD, which progressively worsens, characterizing these volumetrics *in-vivo* overtime provide a great deal of insight into the progression of AD that was not available previously. Fox et al. (1999) showed in a cohort of 28 subjects that AD diagnosis was associated with median brain volume decreases of 1.5% per year compared with 0.2% in the control group. Fox et al. (2001); Fox et al. (1996) showed that even pre-symptomatic AD was linked with hippocampal atrophy, and Jack et al. (1997), Scahill et al. (2002), and Lehéricy et al. (1994) found similar changes in the entire medial temporal lobe (MTL) in early AD and normal aging. Jack et al. (1997) also showed the utility of hippocampal volume in discriminating AD from control populations, an early imaging-based biomarker. Scahill et al. (2002) also showed that ventriculomegaly and increasing of CSF spaces were associated with AD progression. These early volumetric studies of the AD brain were groundbreaking discoveries in the progressive atrophy observed in AD and painted a grim but informative picture of these changes. Many of these changes were observed in asymptomatic and normal aging populations, which highlights the difficulty of detecting pathology pre-symptomatically and providing early pharmaceutical and lifestyle interventions. Figure 19 shows the increasing degree of both gray and white matter atrophy and ventriculomegaly observed with mild cognitive impairment and AD pathology using MRI. Figure 19 shows *in-vivo* similar atrophy to the post-mortem brains in Figure 16. Similarly, Figure 20 shows a topographical heat map of gray matter atrophy observed with increasing Braak stage at autopsy. Note that the MTL and frontal lobes are particularly impacted, as expected from post-mortem histology. With the utility of structural MRI for assessing cortical atrophy and the rising use of machine learning methods, automatic gray matter volume extraction and characterization has become popular both in the clinic and research arenas (Dona et al., 2016). These methods have helped to reduce the

subjectiveness and heterogeneity in radiologist review, as well as to the detection of disease pathology too faint for detection by human review (Diciotti et al., 2012).

A major milestone in reconciling AD imaging research occurred in 2004 with the creation of the Alzheimer's Disease Neuroimaging Initiative (ADNI). ADNI is an on-going multi-site, multimodality imaging consortium with the goal of developing clinical, imaging, genetic, and biochemical biomarkers to detect AD as early as possible and gain meaningful insights from tracking the progression of the disease. ADNI has produced over 1,000 publications in its 17-year history, a truly remarkable feat (Weiner et al., 2017). A substantial contribution of ADNI has been to set the benchmark for establishing reproducible and standardized protocols across imaging site, modality, and vendor, as well as being a leader in data availability and transparency. ADNI provides standardized MRI datasets that have been manually quality controlled by the Aging and Dementia Imaging Research Laboratory at the Mayo Clinic, with checks for artifacts and deviations from expected geometries derived from the ADNI phantom (Wyman et al., 2013). All ADNI imaging sites are qualified based on the ADNI phantom (Jack et al., 2015).

ADNI is currently in its third iteration, *ADNI-3*. The first ADNI protocol from 2004 consisted of [^{11}C]-Pittsburgh Compound-B (PiB) PET Aβ imaging (Klunk et al., 2004), [^{18}F]-fluorodeoxyglucose (FDG) PET metabolic imaging (Reivich et al., 1979), and structural MRI, mostly at 1.5 T, as well as the collection of CSF, genetic, and cognitive data. ADNI-2 introduced Florbetapir PET Aβ imaging (Wong et al., 2010) and included structural, diffusion, functional, and perfusion MRI, all acquired at 3T (Beckett et al., 2015). ADNI-3 added Florbetaben (Sabri et al., 2015) and AV-1451 PET (Chien et al., 2013), a tau tracer, to its protocol (Weiner et al., 2017).

While it would be impractical to systematically review all 1000+ ADNI publications, it is useful to cite some of the major contributions of their findings, as they serve as way markers of the progress of AD neuroimaging research over the past two decades. Perhaps the greatest contribution has been the repeated confirmation of the Amyloid Cascade Hypothesis using ADNI PET (Araque Caballero et al., 2015) and CSF (Young et al., 2014) data, which have shown that amyloid accumulation typically precludes symptom development, tau accumulation, and atrophy and occurs in the ordering proposed by Thal et al. (2002) (Weiner et al., 2017). Further, asymptomatic populations may exhibit noticeable hippocampal and basal forebrain cholinergic system (BFCS) atrophy that is detectable with MRI and the BFCS atrophy predicts PET-derived Aβ burden (Kerbler et al., 2015; Teipel et al., 2014). Figure 21 shows the anatomic evolution of PET and MRI biomarkers versus AD disease stage (Jack et al., 2010).

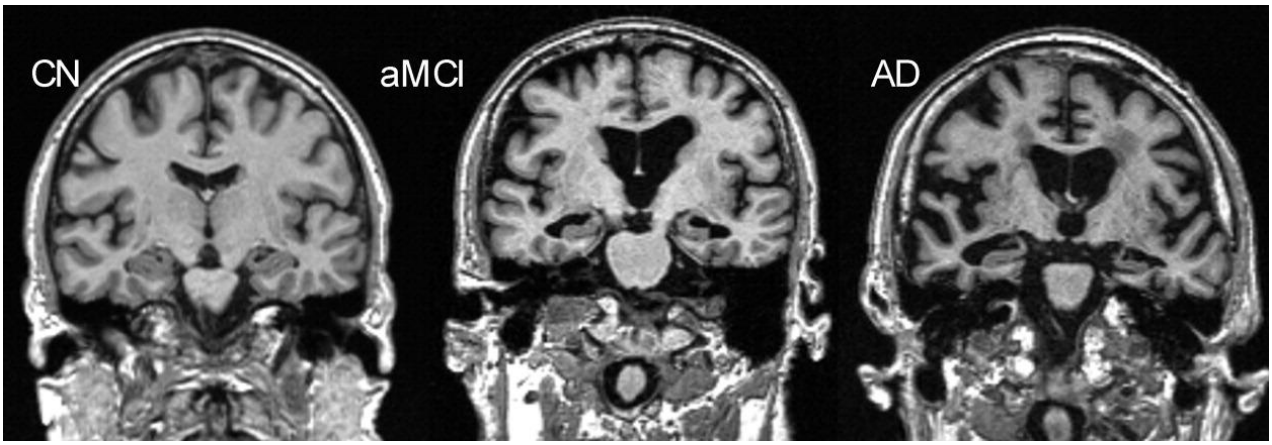

Figure 19: Progressive atrophy (especially medial temporal lobes) in elderly cognitively normal (CN), amnestic mild cognitive impairment (aMCI), and Alzheimer's disease (AD) subjects. Reprinted with permission from Jack, C. R. (2011, 2011/12/01/). Alliance for Aging Research AD Biomarkers Work Group: structural MRI. Neurobiology of Aging, 32*, S48-S57.*

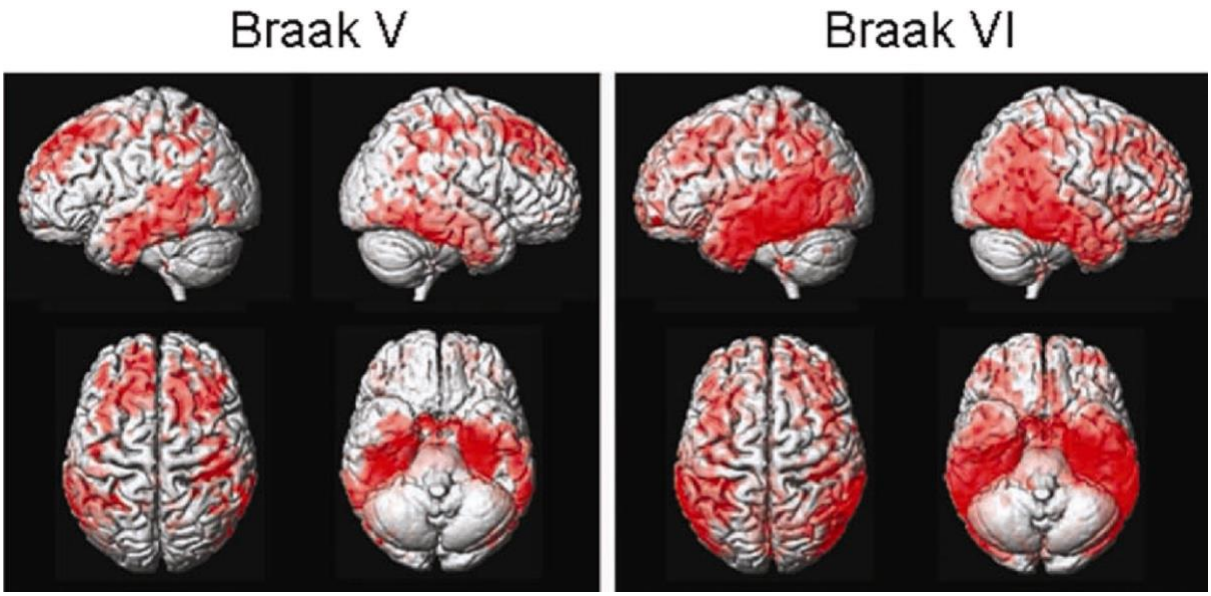

Figure 20: Topography of grey matter loss vs. Braak stage. Jack, C. R. (2011, 2011/12/01/). Alliance for Aging Research AD Biomarkers Work Group: structural MRI. Neurobiology of Aging, 32, *S48-S57.*

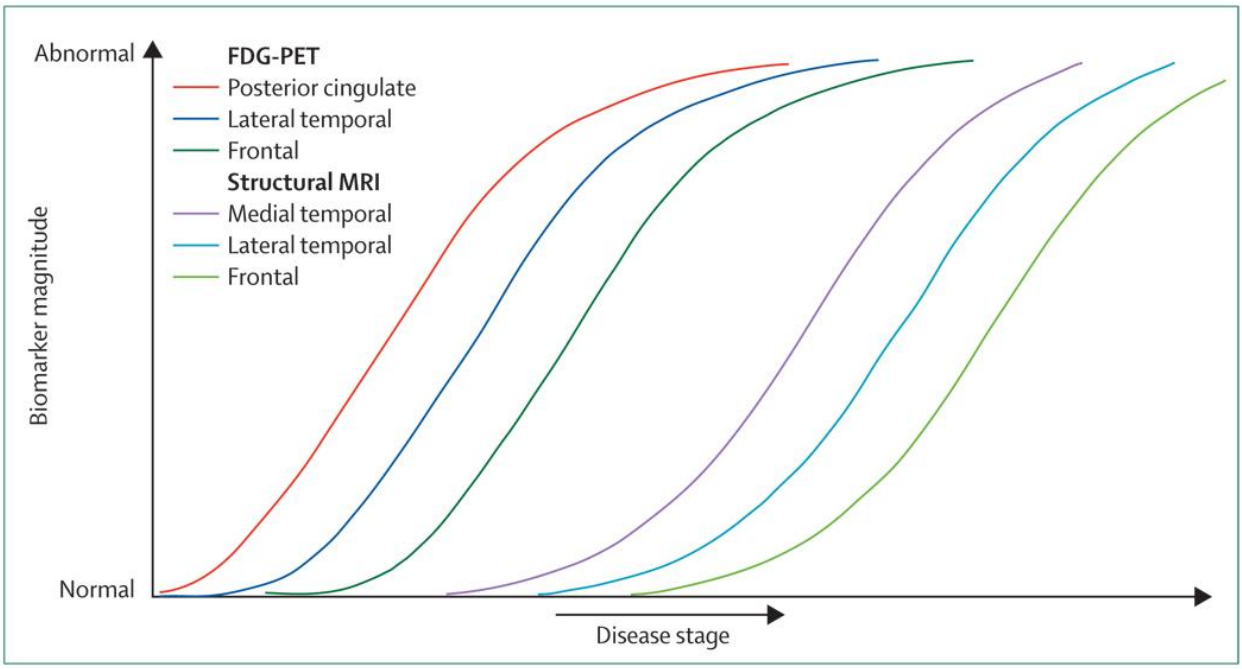

Figure 21: Evolution of abnormal PET and MRI biomarkers with AD stage. from Jack, C. R., Jr., Knopman, D. S., Jagust, W. J., Shaw, L. M., Aisen, P. S., Weiner, M. W., Petersen, R. C., & Trojanowski, J. Q. (2010). Hypothetical model of dynamic biomarkers of the Alzheimer's pathological cascade. The Lancet. Neurology, 9*(1), 119-128.*

Structural MRI biomarkers have largely relied on the detection of atrophy resulting from Aβ or NFTs and how well these measures correlated with symptom onset and disease progression; however, it is possible that there may be anatomical changes that occur before gross atrophy of an area is detectable, particularly in WM. Detecting these changes is perfectly suited to diffusion MRI methods, particularly DTI. One of the earliest DTI and AD papers was published by Rose et al. (2000) found decreased lattice index (anisotropy measure similar to FA) throughout much of the association tracts, while much of the brainstem and pyramidal fibers were spared. Wolf et al. (2015) showed that DTI indices evolved in a non-linear fashion with Aβ, where low Aβ was associated with higher FA and lower MD than controls, but as Aβ further increased, FA decreased and MD increased, suggesting a neuroprotective response to the early presentation of Aβ. Racine et al. (2014) found similar indications of neuroprotective behavior in the presence of Aβ as Wolf et al. (2015). Antemortem DTI scans with postmortem AD pathology staging showed that high Braak scores (V-VI) were associated with higher MD in the cingulum, fornix, and entorhinal white matter (Kantarci et al., 2017). Higher MD and lower FA in the ventral cingulum, entorhinal, and precuneus white matter have also been associated with higher Braak staging (Kantarci et al., 2017). Increased CSF measured Aβ42 was associated with increased MD in gray and white matter in the frontal, parietal, occipital, and temporal lobes in healthy aging adults at risk for AD (Bendlin et al., 2012). Further, DTI evidence suggest that WM degeneration in AD may follow a pattern of retrogenesis, late myelinating areas degrade first, as well as Wallerian degeneration in competing processes (Alves et al., 2015).

DTI is also useful in AD research because of its utility to discriminate AD, MCI, and cognitively normal subjects and its correlation with cognitive performance (Nir et al., 2013). Adults with clinical AD have been found to evidence increased MD and decreased FA across

multiple brain regions (Mayo et al., 2018; Mayo et al., 2017; Nowrangi et al., 2015). Moreover, WM integrity has been found to be associated with cognitive decline and, more specifically, impaired episodic memory in non-demented adults (Acosta-Cabronero & Nestor, 2014; Mayo et al., 2018; O'Dwyer et al., 2011). For example, Nicholas et al. (2020) found that increases in frontal MD across time were associated with decreases in the ability to correctly recall words (i.e. free recall) in older adults without AD (Nicolas et al., 2020). Remy et al. (2015) found an association between lower FA in the medial temporal lobe and worse episodic memory in older adults without AD (Rémy et al., 2015). Similarly, Metzler-Baddeley et al. (2011) showed that better WM integrity (increased MD and decreased FA) in the fronto-temporal lobe was associated with better episodic memory in older adults without AD (Metzler-Baddeley et al., 2011). Lastly, Lockhart et al. (2012) found associations between lower FA and worse episodic memory across younger and older adults without AD throughout major association fibers, including the superior longitudinal fasciculus, inferior longitudinal fasciculus, the cingulum bundles, uncinate fasciculus, and thalamo-cortical projections (Lockhart et al., 2012). Clearly, AD is a complex disease that requires imaging, genetic, histologic, and cognitive assessments to provide a comprehensive picture.

3.5. Alzheimer's Disease and Down Syndrome

There is much to be learned about DS, particularly in geriatrics, as the life expectancy of people with DS nearly quadrupled in the last century, from 16 years of age in the early 20th century to 60 years in 2019 (Down Syndrome: Condition Information; Zigman et al. 2008). It is known that nearly all persons with DS will develop AD neuropathology by age 40, and post-mortem studies have shown AD neuropathology in adults with DS as young as 20 years-of-age (Down

Syndrome: Condition Information). The likelihood of AD development in DS is greater than any other demographic; therefore, the study of the link between both diseases is of great importance. The relationship between AD, DS, and amyloid is underscored by the production of APP, as the gene that codes for APP is located on the 21st chromosome. This makes amyloid an important marker for the study of AD development and progression in DS (Annus et al. 2016).

Neale et al. (2018) provided an excellent review of current DS-AD PET and MRI studies and, at the time of publishing, there were only 11 reported PET and 9 MRI studies. Many of these studies have had small datasets, as low as 7 total participants (Handen et al., 2012) and as many as 63 (Sigan L. Hartley et al., 2014). It is important to note that both Handen and Hartley are collaborators and coauthors for the publications produced from research presented in Chapters 4 and 5. While these studies have covered numerous imaging and cognitive domains, limited sample size, artifacts, and/or limited data types have left a great deal of the DS-AD frontier unstudied. To this end, the analyses conducted in this work seek to bridge the PET, MRI, and cognitive DS-AD literature by providing a deep dive into the associations of DS white matter microstructure with global Aβ burden and cognitive performance. Within the current body of literature, the two studies presented in Chapters 4 and 5 are the largest DS imaging studies to date and provide revelations of the interplay of Aβ, diffusion alteration, and links to episodic memory performance, which have not been previously studied in a DS cohort.

3.6. [^{11}C]PiB Amyloid Imaging

[^{11}C]-Pittsburgh Compound-B (PiB) is a PET tracer derived from Thioflavin T, which is a histological dye used for identifying amyloid plaques ex vivo. Radiolabeled PiB has been shown to have sufficient brain permeability and histologically confirmed binding with amyloid to serve as an effective measure of amyloid burden. In previous work completed by Lao, et al.

(2018), a cohort of non-Demented adults with DS were labelled as either PiB+ or PiB- using population derived amyloid positivity thresholds based on standard uptake value ratios (SUVR) in subcortical gray matter ROIs. PiB+ individuals were shown to have increased amyloid burden, while PiB- individuals had normal levels of amyloid.

3.7. Neuroplasticity

Neuroplasticity, particularly synaptic plasticity, is the method by which the brain learns and adapts to stimuli and to optimize performance of tasks and an excellent overview of the mechanisms of plasticity is provided by Meriney and Fanselow (2019) and is summarized here with permission. Plasticity is the physiological mechanism underlying learning, memory, adaptation, sensitization, sensory processing, addiction, and cognition. Plastic changes can occur via structural alterations in presynaptic nerve terminals, postsynaptic specializations, or in the function of those synaptic compartments. There are several mechanisms to stimulate these changes, including small transient changes in the neurotransmitter release of existing synapses to large structural changes via synapse genesis, reinforcement, and pruning. Plasticity may be divided into short-term and long-term plasticity.

Short-term plasticity refers to synaptic changes resulting from rapid, successive synapse activation and may take several forms: paired-pulse potentiation, paired-pulse depression, tetanic potentiation, tetanic depression, post-tetanic potentiation, short-term depression (STD), and short-term facilitation (STF). Paired-pulse potentiation and paired-pulse depression are processes where two extremely close (<100 ms separation) action potentials result in either increased (potentiation) or decreased (depression) neurotransmitter concentration in the synapse.
For tetanic (from Latin *tetanus* – to spasm) and post-tetanic potentiation, the repeated stimulation can give rise to increased neurotransmitter concentration (tetanic and post-tetanic potentiation) or

decreased neurotransmitter concentration (post-tetanic depression). The outcome of these processes is dependent on the initial concentration of neurotransmitter in the synapse. Figure 22 shows the synaptic activity for paired-pulse facilitation (A) and titanically stimulated processes (B,C,D).

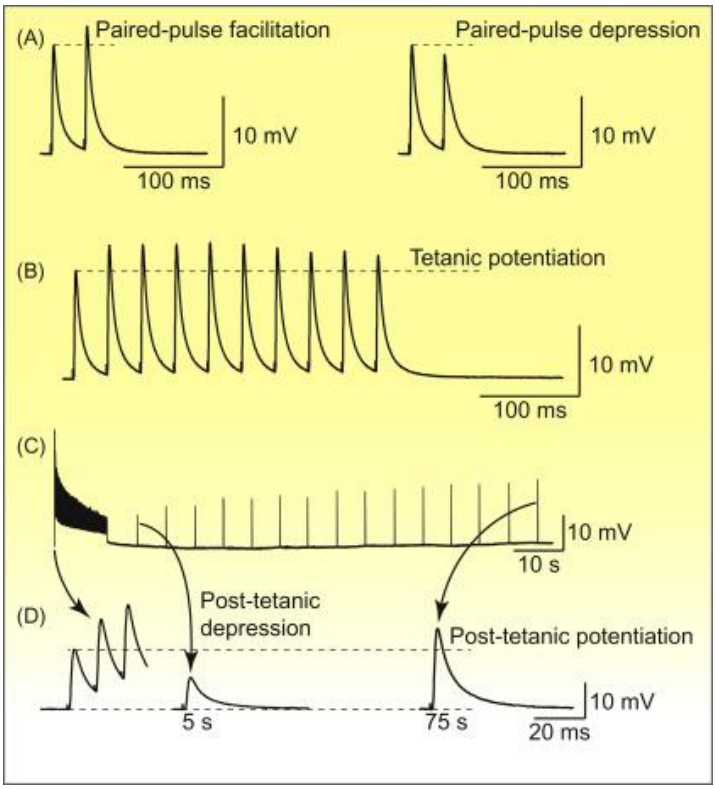

Figure 22: (A) An example of paired-pulse facilitation (left). In this example, the second endplate potential in a pair is larger than the first. On the right is an example of paired-pulse depression in which the second endplate potential in a pair is smaller than the first. (B) An example of tetanic potentiation. During a short train of high-frequency activity (30 action potentials per second; 30 Hz) the endplate potentials (EPP) increase in amplitude compared to the first EPP. (C) An example of post-tetanic changes in neurotransmitter release. In this case, a long high-frequency burst of activity (200 Hz for 10 s) leads to an immediate depression of neurotransmitter release (post-tetanic depression), followed by an increase in neurotransmitter release (post-tetanic potentiation). Post-tetanic depression occurs due to synaptic vesicle depletion from the nerve terminal. Post-tetanic potentiation occurs when residual bound calcium remains in the terminal after synaptic vesicle depletion recovers. Panel D shows an enlargement of endplate potentials in C at time points defined by the arrows. Reprinted with permission from Meriney, S. D., & Fanselow, E. E. (2019). Chapter 14 - Synaptic Plasticity. In S. D. Meriney & E. E. Fanselow (Eds.), Synaptic Transmission (pp. 287-329). Academic Press. https://doi.org/https://doi.org/10.1016/B978-0-12-815320-8.00014-4

In STD, synapses act as low-pass filters and slow down the transfer of information. While STF acts as a high-pass filter. These filters increase synaptic efficiency by allowing more

time for neurons to decide whether the received information is useful enough to generate an action potential. The filtering mechanics of STD (A) and STP (B) are shown in Figure 23.

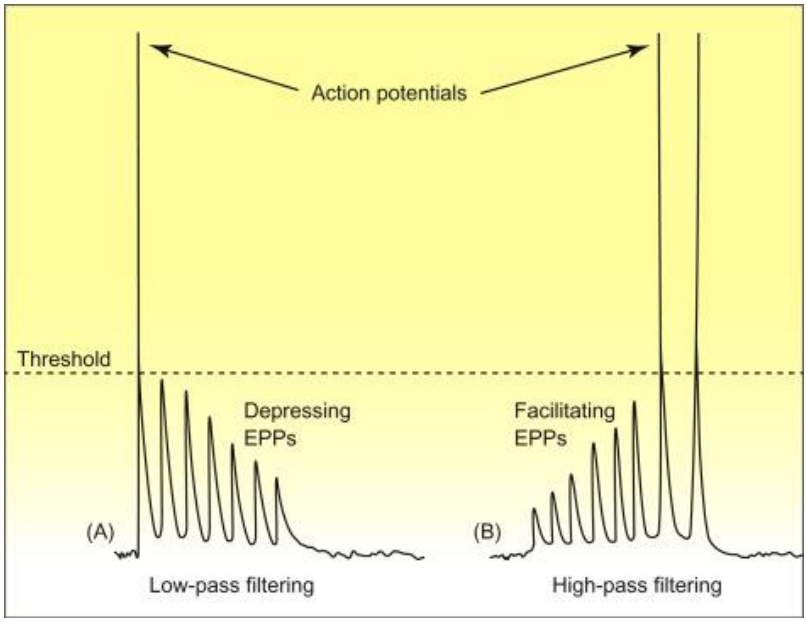

Figure 23: Short-term synaptic plasticity can allow synapses to function as either high-pass or low-pass filters. Reprinted with permission from Meriney, S. D., & Fanselow, E. E. (2019). Chapter 14 - Synaptic Plasticity. In S. D. Meriney & E. E. Fanselow (Eds.), Synaptic Transmission (pp. 287-329). Academic Press. https://doi.org/https://doi.org/10.1016/B978-0-12-815320-8.00014-4

As the name implies, short-term plasticity's effects are only temporary, if the stimulus is not sustained, the synapse will return to normal. Sustained stimulation leads to long-term plastic changes, including long-term potentiation (LTP) and long-term depression (LTD). Long-term plasticity is associated with memory formation and may be observed in the hippocampus. High-frequency stimulation of the perforant pathway (entorhinal cortex to the hippocampus) can result in increased synaptic activity for hours or even days after the initial excitation. This served as a confirmation of Hebbian plasticity, which purports that pre- and post-synaptic neurons can be active simultaneously, which strengthens the connection between the two. This is also known as the *fire together, wire together* principle of neuroplasticity, indicating that simultaneously active neurons during task performance will preferentially optimize their connection. An illustration of

the perforant pathway is shown in Figure 24. Figure 25 (left) shows LTP, where sustained (~1s), high-frequency (100Hz) stimulus results in maintained synaptic activity for hours after the initial excitation. Hebbian plasticity extends to areas outside of the hippocampus, including the cortex, amygdala, and mid-brain. Conversely, sustained (~20s) lower frequency stimulation can result in LTD, which is linked with learning, memory, and addiction. LTD works to suppress synaptic activity to allow the promotion of more useful synapses via LTP. LTD post-synaptic activity is shown in Figure 25 (right).

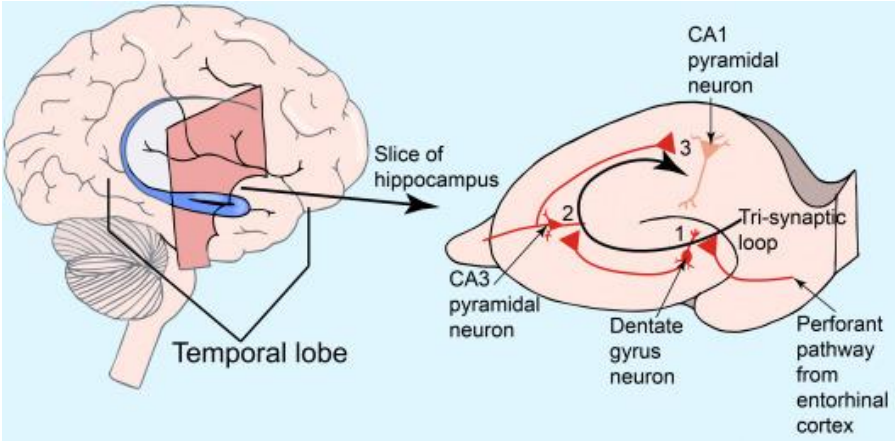

Figure 24: Hippocampal trisynaptic circuit. Reprinted with permission from Meriney, S. D., & Fanselow, E. E. (2019). Chapter 14 - Synaptic Plasticity. In S. D. Meriney & E. E. Fanselow (Eds.), Synaptic Transmission (pp. 287-329). Academic Press. https://doi.org/https://doi.org/10.1016/B978-0-12-815320-8.00014-4

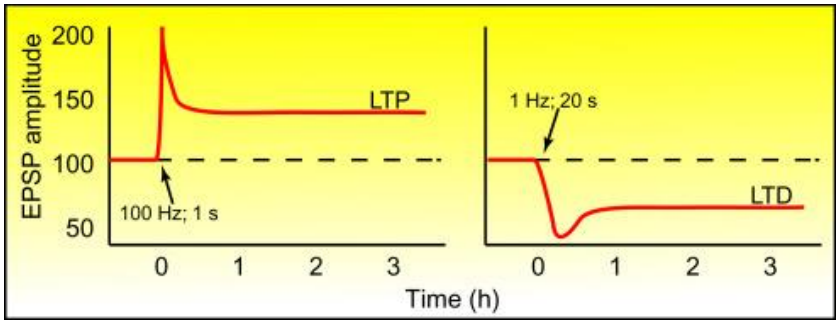

Figure 25: Long-term potentiation (LTP) and long-term depression (LTD). Plots of excitatory postsynaptic potential amplitude at a hippocampal synapse over time during two different stimulus patterns. (Left panel) Following a long burst of high-frequency stimulation (100 Hz for 1 s), synapses strengthen, leading to a larger EPSP amplitude, and this is maintained for hours (LTP). The transient spike in strengthening that occurs immediately after the 100 Hz stimulus train results from post-tetanic potentiation. (Right panel) Following a low-frequency train of activity (1 Hz for 20 s), synapses weaken persistently, leading to a smaller EPSP amplitude (LTD). Reprinted with permission from Meriney, S. D., & Fanselow, E. E. (2019). Chapter 14 - Synaptic Plasticity. In S. D. Meriney & E. E. Fanselow (Eds.), Synaptic Transmission (pp. 287-329). Academic Press. https://doi.org/https://doi.org/10.1016/B978-0-12-815320-8.00014-4

The above physiology is by no means an exhaustive list of plastic processes. Not every connection in the brain is useful and simple connections developed in childhood, as well as unused synapses, need to be removed in a process known as *synaptic pruning*. The exact mechanisms of pruning are not known; however, it is known to occur both in small, local connections and larger connections throughout the brain. The most significant period of pruning occurs from adolescence to adulthood, where the number of synapses is reduced by 50% from the peak synaptic density (Chechik et al., 1999).

Long standing notions in the study of brain plasticity have been 1) the importance of the critical period from infancy to adolescence when the brain has been observed to be most plastic and 2) that brain plasticity largely stabilizes in late adolescences to adulthood (Voss et al., 2017). Recent studies have begun to dispute the latter notion, leading to the emerging view that the brain retains significant plasticity throughout lifespan and that a variety of forms of behavioral training can induce clear neuroplastic changes (Voss et al., 2017).

It is currently impossible to image individual synapses in the brain *in-vivo* using MRI and will likely not be possible in this author's lifetime, if ever. As disparaging as this might seem, several imaging studies from the past two decades have shown the sensitivity of MRI to gross brain changes likely attributable to neuroplastic processes. A seminal work in the study of imaging neuroplasticity was published by Maguire et al. in 2000. Maguire et al. (2000) studied the brains of taxi drivers in London using T1 structural imaging and found increased bilateral hippocampal volumes in taxi drivers relative to controls. Since the work of Maguire et al., the imaging and training methods used to study plasticity have only grown. Driemeyer et al. (2008) used three months of a visuo-motor task, juggling, to induce occipito-temporal gray matter changes and suggested that learning a new skill is more impactful for plasticity than reinforcing already learned skills.

Over the past decade, fMRI and DWI methods have garnered a great deal of popularity for imaging plasticity due to their functional connectivity and microstructure sensitivity, respectively. Scholz et al. (2009) used a similar juggling task to Driemeyer et al. to exam white matter (WM) microstructural differences using diffusion tensor imaging (DTI) and found that fractional anisotropy (FA) increased in the intraparietal sulcus in the training group; this work was the first imaging study to examine the role of WM in the learning process (Scholz et al., 2009). A 2010 study by Taubert et al. showed that prefrontal changes could be detected using DTI following a brief period of training on a simple balancing task (Taubert et al., 2010). In a six-month training period, twenty younger and twelve older adults were examined using DTI before and after cognitive training over several domains: working memory, episodic memory, and perceptual speed. Comparison of DTI metrics in the corpus callosum found similar pre-post alterations in the younger and older populations compared to controls; these findings suggested

that neuroplastic processes extend well beyond adolescence (Lövdén et al., 2010). Further studies showed WM microstructural changes related to learning a second language (Hosoda et al., 2013) and extensive musical instrument practice (Gärtner et al., 2013; Moore et al., 2014). With growing interest of tailoring training tasks to elicit neuroplastic responses in more targeted areas detectable by MRI, plasticity studies began to employee videogames into their training paradigms. Sagi et al. (2012) utilized the racing game *Need for Speed* (NFS) ("Need for Speed: Shift," 2009) to evoke microstructural changes in and around the hippocampus, namely a decrease in mean diffusivity (MD), after a ninety-minute training period, which was subsequently replicated in a water-maze rodent model. Further, Sagi et al. observed a significant group by time interaction relative to normalized lap time (a measure of task improvement), with the learning group improving significantly relative to active controls. Further, MD in the parahippocampus was inversely correlated with task performance (Sagi et al. 2012). Hofstetter et al. (2013) went on to show, using a dataset incorporating data used by Sagi et al. 2012, that short-term training with NFS resulted in decreases in MD localized to the fornix using tract-based spatial statistics (TBSS) (Hofstetter et al., 2013). Tavor et al. (2013) also looked at NFS training and employed the more complex CHARMED method, which uses multi-shell diffusion weighting and compartmental modeling to estimate the amount of hindered, restricted, and free diffusion as well as the fiber orientation within a voxel. Tavor et al. observed temporary increases in the restricted volume fraction in the left hippocampus and a bilateral decrease in MD in the insular cortices and parahippocampal gyri, as well as the left hippocampus (Tavor et al., 2013). MD was positively correlated with hours spent completing videogame training in several brain regions, including the hippocampus, amygdala, thalamus, corpus callosum, and internal capsule (Takeuchi et al., 2015).

Keller and Just (2016) examined both fMRI and microstructural changes resulting from short-term training (45 minutes) with a spatial route learning video game and found both decreased MD in the hippocampus and greater functional connectivity between the hippocampus and the cortex relative to controls (Keller & Just, 2016). Decreases in MD were also observed in the precuneus, left superior frontal gyrus, left insula, left supramarginal gyrus, the left superior temporal gyrus, and left fusiform gyrus. Increased functional connectivity between the left hippocampus and the right posterior inferior temporal gyrus, right anterior temporal gyrus, and the right intraparietal sulcus was also observed and was correlated with decreased MD in the hippocampus and greater task performance (Keller & Just, 2016). Further, Keller & Just (2016) observed that the regions associated with visuo-spatial learning were right lateralized, while the regions associated with motor learning were left lateralized, corresponding to the contralateral side of all subjects' dominant hand (right). The seemingly contradictory work of Keller and Just, Tavor et al. 2013, and Sagi et al. 2012 with the work of Takeuchi et al. 2015 suggest that more complex and multimodal imaging may be required to accurately characterize plastic processes. Further, no study has examined advanced microstructural imaging methods (e.g., NODDI, CHARMED) in both the short-term (~hours) and long-term (~weeks) while completing videogame training.

4. White matter microstructure associations to amyloid load in adults with Down syndrome

4.1. Background

Down syndrome (DS) is a genetic disorder involving trisomy of chromosome 21 resulting in an overproduction of various proteins encoded from this chromosome, including amyloid precursor protein (APP)(Wiseman et al., 2015). As one of the neuropathological features of Alzheimer's disease (AD), an overproduction of APP and accompanying amyloid-beta (Aβ) pathology are implicated as primary sources for the enhanced risk of AD in DS individuals(Wiseman et al., 2015). As the life expectancy of people with DS nearly quadrupled in the last century, from 16 years of age in the early 20th century to 60 years in 2019 (Zigman et al., 2008) the prevalence of AD in this population has increased in parallel, with a lifetime risk of approximately 90% (McCarron et al., 2014).

Positron emission tomography (PET) imaging studies have been used to characterize amyloid burden in DS populations and have shown increased retention of [^{11}C]PiB (Pittsburgh compound B), which preferentially binds to amyloid plaques, in a some participants by their fourth decade (30-40 years) of life and the majority with amyloid positivity (amyloid(+)) by the middle of their fifth decade (Annus et al., 2016; Lao et al., 2016). These findings reveal the emergence of PET-measured amyloid(+) status in DS approximately 30 years earlier than seen in the general (non-DS) population. However, similar to the general population, the early stages of amyloid accumulation in DS do not adversely affect cognitive function. In a study of non-demented DS participants (age 30-53), there were no significant differences in neuropsychological measures across amyloid(+) and amyloid(-) groups (S. L. Hartley et al., 2014).

There are relatively few structural magnetic resonance imaging (MRI) studies of aging-DS and these studies have had varying results.(Neale et al., 2018) Detectable changes of gray matter volume and glucose metabolism with increased amyloid were observed by Matthews et al.(2016) and Rafii et al.(2015) in non-demented DS individuals. Recently, Lao et al.(2018) studied a group of non-demented adults with DS using structural MRI and PET and found no indication of pre-AD changes in MRI-measured gray matter morphology between amyloid(+) and amyloid(-) participants. Similar to the temporal course of AD biomarkers in the general population, these studies confirm that amyloid accumulation precedes gray matter atrophy and clinical dementia onset in DS (Matthew D. Zammit et al., 2020). This order of events is consistent with the AT(N) model (amyloid -> tau -> neurodegeneration) describing the progression of AD-related biomarkers (Jack et al., 2018). Neurodegeneration is typically characterized by MRI-measured atrophy in the hippocampus or FDG PET patterns of hypometabolism in the precuneus, temporal and parietal cortices. Research is also ongoing to employ other neuroimaging modalities such as diffusion tensor imaging (DTI) to characterize subcortical changes related to neurodegeneration.

Diffusion tensor imaging (DTI) is a non-invasive MRI technique used to probe microstructural differences in water diffusion properties of biological tissues (Basser et al., 1994b; Basser & Pierpaoli, 1996). DTI measurements include the mean diffusivity (MD), which is the directionally averaged diffusivity and is sensitive to the density of microstructural features; and the fractional anisotropy (FA), which is a summary measure of the directional variance of diffusivities and is often used as a sensitive marker of white matter microstructural changes (Alexander et al., 2007). Although AD is often considered a disease of gray matter,

white matter degeneration is also observed. This finding has been repeatedly observed in several studies(Mayo et al., 2017; Nowrangi et al., 2013; Nowrangi et al., 2015; O'Dwyer et al., 2011) that have used DTI to compare AD subjects to healthy controls. DTI investigations of white matter integrity in AD populations have reported increased MD and decreased FA in multiple white matter regions across the brain (Mayo et al., 2018; Mayo et al., 2017; Nowrangi et al., 2015). These outcomes have been associated with cognitive decline and impaired executive function resulting from the deterioration of cortico-limbic, entorhinal, and cortico-cortico connections, potentially resulting from the presence of Aβ and NFTs.

Previous DTI studies of non-demented individuals with DS have reported reduced FA relative to typically developing controls in frontal white matter connections (Fenoll et al., 2017; Romano et al., 2018). Similarly, Powell et al.(2014) observed widespread FA decreases in the frontal lobe in demented DS individuals compared with non-demented DS individuals and age-matched controls.

Several neuroimaging studies have also investigated the relationships between early white matter microstructural changes in AD and amyloid burden with PiB PET(Chao et al., 2013; Racine et al., 2014; Wolf et al., 2015). The goal of this study was to examine these relationships within an aging DS population. Given the near certainty of AD development and wide range of disease trajectories in the DS population and the marked early onset of pathology, characterizing the relationships between early white matter changes and AD burden in DS is essential to better understand the disease. In this work, we investigated the relationships between [^{11}C]PiB amyloid load ($A\beta_L$) imaging of amyloid burden in the brain with DTI measurements to assess white matter microstructure changes in an aging cohort of adults with Down syndrome. Further, DTI measures are known to be correlated with age;

FA has been shown to decrease with age, and MD is reported to increase with age. To investigate if the dependence of DTI measures on age and amyloid was constant, we looked at a continuous interaction term of amyloid-by-age ($A\beta_L$*age) with FA and MD.

4.2. Methods

4.2.1. Participant Selection

Ninety-six (n=96) subjects with Down syndrome (average age 38.45 ± 7.98 yrs.) received baseline scans as part of the Alzheimer's Biomarker Consortium-Down Syndrome (ABC-DS) study at three imaging facilities (34 at the University of Wisconsin-Madison, 34 at the University of Pittsburgh Medical Center (UPMC), and 28 at the University of Cambridge (UC)). All participants had genetically confirmed trisomy 21. Eleven participants were excluded due to excessive motion during the DTI acquisition. Of the remaining 85 participants, 78 were classified as non-demented (i.e., cognitively and functionally stable); 4 were classified as having mild cognitive impairment (MCI), and 3 participants were classified as demented. These clinical status determinations were based on a case consensus process that included at least three staff with clinical expertise who were blind to MRI and PET imaging data. Informed consent was obtained prior to data collection.

The following information was used in the case consensus process: a) medical/psychiatric history and neurological exam; b) caregiver-report of participant's functioning and life events; c) participant's adaptive skills on the Vineland Adaptive Behavior Scales (*Down Syndrome: Condition Information*, 2012; Sparrow et al., 1984); d) caregiver-report of participant's dementia symptoms on Dementia Questionnaire for

People with Learning Disabilities (Evenhuis, 2018) or Dementia Scale for Down syndrome (Jozsvai et al., 2018); e) participant's profile on the Down Syndrome Mental Status Examination(James V Haxby, 1989), Developmental Test of Visual-Motor Integration, 5th Edition(Beery, 2004), Wechsler Intelligence Scale for Children(Wechsler, 1945) Block Design and Haxby extension (J. V. Haxby, 1989), and Developmental NEuroPSYchological Assessment (Korkman et al., 2007) Word Generation Semantic Fluency.

Analyses were performed both with and without the subjects classified as either MCI or demented. Removal of these subjects did not result in a loss of significant effects, so subjects were included for increased statistical power.

4.2.2. PET Imaging of Amyloid Burden

A target dose of 15 mCi of [^{11}C] PiB was delivered intravenously via with participants while resting outside the PET scanner. PET data were acquired following a 40-minute radiotracer uptake period using either a Siemens ECAT HR+ (UW and UPMC), a Siemens 4-ring Biograph mCT (UPMC), or GE Advance (UC) scanner. The dynamic acquisition was performed from 40 – 70 minutes (post-injection) with data binned into 5-minute time frames. Following the emission scan, a 6-10 min ^{68}Ge/^{68}Ga transmission scan was acquired for attenuation correction of the annihilation radiation. PET images were reconstructed with the ECAT system software (OSEM algorithm; 4 iterations, 16 subsets) to a voxel size of 2.57mm x 2.57mm x 2.43 mm and matrix dimension of 128 x 128 x 63 with corrections for detector deadtime, scanner normalization, photon scatter, and radioactive decay. PET scans were reoriented along the anterior commissure posterior commissure (AC-PC) line, and inter-frame motion was corrected (Woods et al.,

1998).Standard uptake value ratio (SUVR) images were calculated from PET data 50-70 min post-injection (McNamee et al., 2009) with a cerebellar gray matter reference region.(Klunk et al., 2004; Lopresti et al., 2005; Price et al., 2005) Global Aβ burden was calculated using the amyloid load metric ($A\beta_L$) following previously described methodology (M. D. Zammit et al., 2020). Briefly, PiB images were spatially normalized to MNI152 space using a DS-specific PET template (Lao et al., 2019). Given the SUVR image and DS-specific template images of PIB carrying capacity and nonspecific binding, the $A\beta_L$ was calculated using the linear least-squares method.

4.2.3. Diffusion Tensor Imaging

Magnetic resonance imaging (MRI) data were collected on two 3.0T MRI scanners - a GE SIGNA 750 with an 8-channel head coil (UW-Madison) and a Siemens Magnetom Trio scanner with a 64-channel head coil (UPMC). Diffusion-weighted imaging at both sites was performed using a single-shell, diffusion-weighted spin echo sequence (UW-Madison TR/TE = 7800/67ms; UPMC TR/TE = 7200/56ms). The DWI protocol consisted of either 7 (UPMC) or 6 (UW-Madison) non-diffusion weighted (b_0) images and diffusion weighted images with a b-value of $1000 s/mm^2$ in 48 non-collinear directions. Additional imaging parameters consisted of matrix size: and 116 x 116 with 80 slices, field of view: 23.2 x 23.2 x 16 cm^3, and 2mm slice thickness. Data were processed using an in-house processing pipeline utilizing tools from FSL(Jenkinson et al., 2012), Mrtrix(Tournier et al., 2019), and the DiPy toolbox(Garyfallidis, Brett, Amirbekian, Rokem, van der Walt, Descoteaux, Nimmo-Smith, et al., 2014). The diffusion-weighted data were corrected for Gibbs' ringing artifacts(Kellner et al., 2016), Rician noise(Veraart et al., 2016), and eddy current distortions and head motion with outlier replacement(Andersson et al., 2016; Andersson &

Sotiropoulos, 2016). A threshold of 10% or more of slices replaced as outliers within a single diffusion weighted image (DWI) was established as a criterion for removal of a volume; however, no volumes exceeded this threshold and no DWIs were removed. The diffusion tensors were estimated using a robust estimator method, RESTORE (Chang et al., 2005), and FA and MD maps subsequently calculated.

All FA data in the study were aligned to a 2mm isotropic population derived FA template using ANTs(Avants et al., 2011). This template was constructed using amyloid negative participants without MCI or AD. A medial surface skeleton was generated from the population averaged FA image. Each participant's regional maximum FA data were then projected onto this skeleton surface for voxel-wise statistical analyses. The MD maps were likewise spatially normalized and projected onto the FA skeleton for analysis. The JHU white matter atlas labels(Oishi et al., 2008) were warped to the population derived FA template using ANTs (Avants et al., 2011).

4.2.4. Statistical Analyses

4.2.4.1. Tract-based Spatial Statistics

Statistical analyses of the DTI data were performed using the tract-based spatial statistics (TBSS) pipeline in FSL(Smith et al., 2006; Smith et al., 2004). Briefly, the FA data from all subjects were used to generate a population-derived FA template, which was used as the target image for analysis. A medial surface skeleton was generated from the population-averaged FA image. Each subject's regional maximum FA data were then projected onto this skeleton surface for voxel-wise statistical analyses. The FA derived warps were applied to the MD maps and projected onto the FA skeleton for analysis.

4.2.4.2. Statistical Testing

A general linear model (GLM) was constructed in FSL to investigate voxel-wise correlations of FA and MD with amyloid load, $A\beta_L$. These analyses were completed using the FSL tool PALM with threshold-free cluster enhancement (TFCE) to identify significant brain regions. Correction for multiple comparisons was performed by controlling for the Family-Wise Error rate (Smith & Nichols, 2009). For all TBSS results, the FSL tool *tbss_fillI* was used for ease of visualization; all inflated regions were mapped from a corrected significance of $p<0.05$.

A general linear model (GLM) was constructed in FSL to investigate voxel-wise comparisons of continuous $A\beta_L$-by-age ($A\beta_L$*age) interactions of DTI measures projected onto the population derived FA. A mask of areas with significant $A\beta_L$*age interaction was generated and used to extract average MD and FA values from within these areas.

4.3. Results

Figure 26 shows regions of positive $A\beta_L$*age interaction with MD. Figure 27 shows a negative $A\beta_L$*age interaction with FA. Results are mapped at a significance of $p<0.05$ corrected for multiple comparisons and imaging site. Across the extent of the significant regions shown, FA and MD were correlated with $A\beta_L$*age at $r=-0.606$($p<0.001$ corrected) and $r=0.623$($p<0.001$ corrected), respectively. No significant positive $A\beta_L$*age interactions with FA, nor were any significant negative $A\beta_L$*age interactions with MD observed.

Figures 28 and 29 show regions of significant positive correlation of $A\beta_L$ and MD. The red regions in Figure 28 were generated with a site covariate and corrected for multiple comparisons; Figure 29 was generated using correction for multiple comparisons, site, and age. Blue regions in Figures 30 and 31 show widespread significantly decreased FA with increased $A\beta_L$, including the bilateral occipital and prefrontal white matter, as well as the genu

of the corpus callosum, the right superior longitudinal fasciculus, the fornix, and left inferior longitudinal fasciculus. The blue regions in Figure 30 were generated with a site covariate and corrected for multiple comparisons; Figure 31 was generated using correction for multiple comparisons, site, and age. Likewise, Across the extent of the significant regions shown, FA and MD were correlated with $A\beta_L$ at r=-0.611($p<0.001$ corrected) and r=0.552($p<0.001$ corrected), respectively.

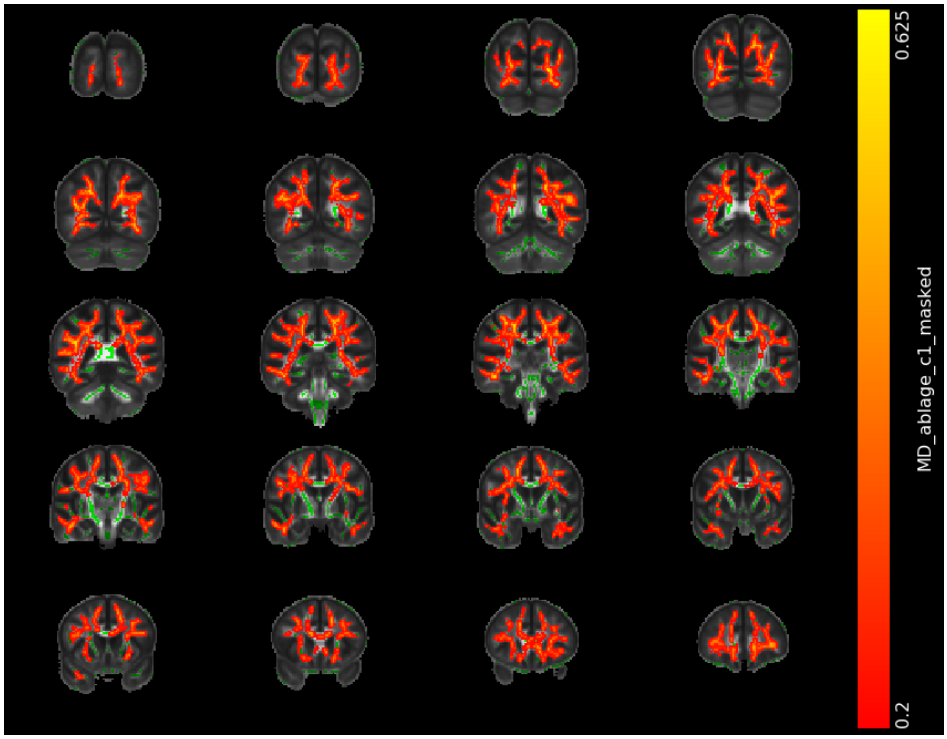

*Figure 26: Regions of significant AβL*age interaction with MD. Results reflect regions with p<0.05 corrected for multiple comparisons and imaging site.*

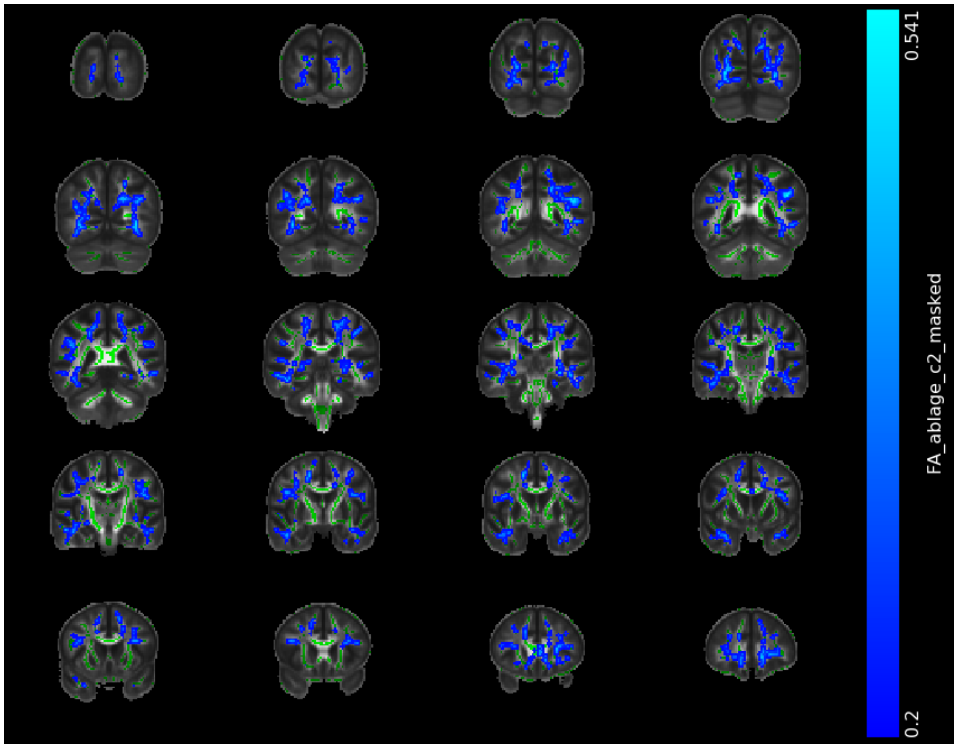

*Figure 27: Regions of significant negative AβL*age interaction with FA. Results reflect regions with p<0.05 corrected for multiple comparisons and imaging site.*

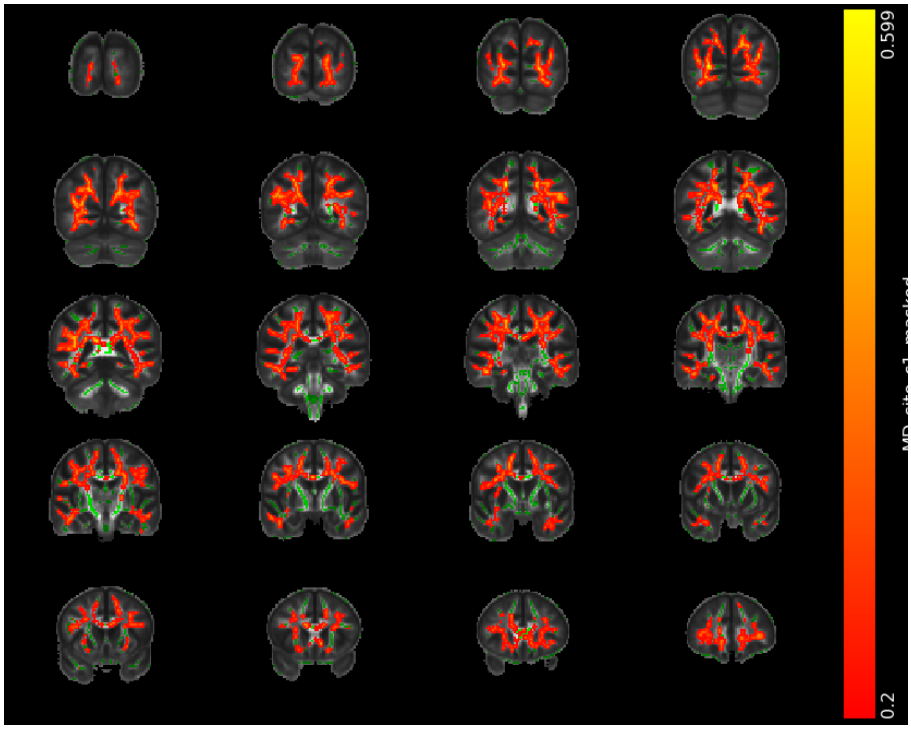

Figure 28: Regions of significant correlation between MD and AβL. Results reflect regions with p<0.05 corrected for multiple comparisons and imaging site.

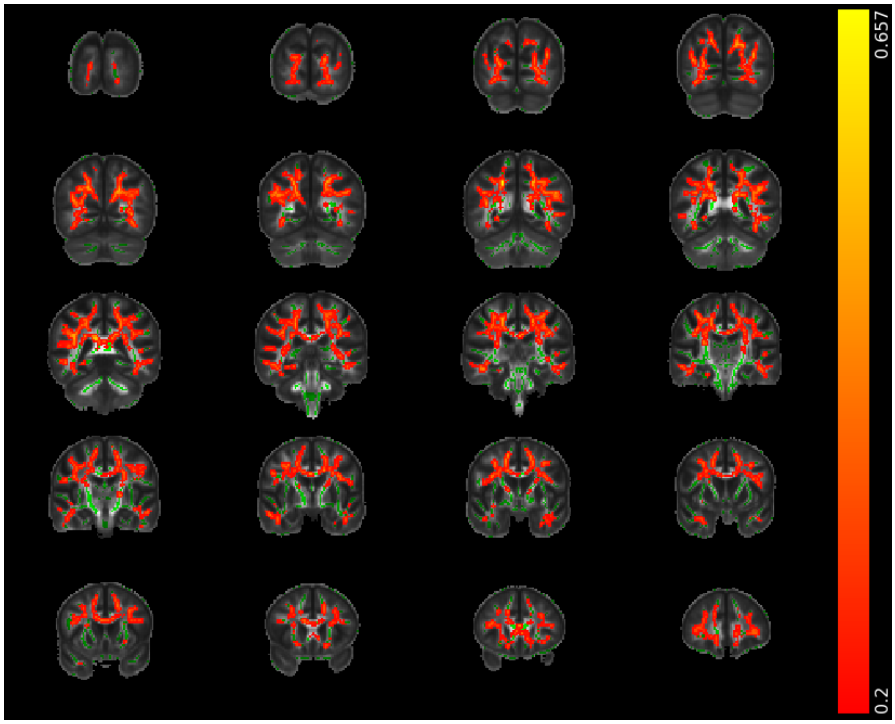

Figure 29: Regions of significant correlation between MD and AβL. Results reflect regions with p<0.05 corrected for multiple comparisons, imaging site, and age.

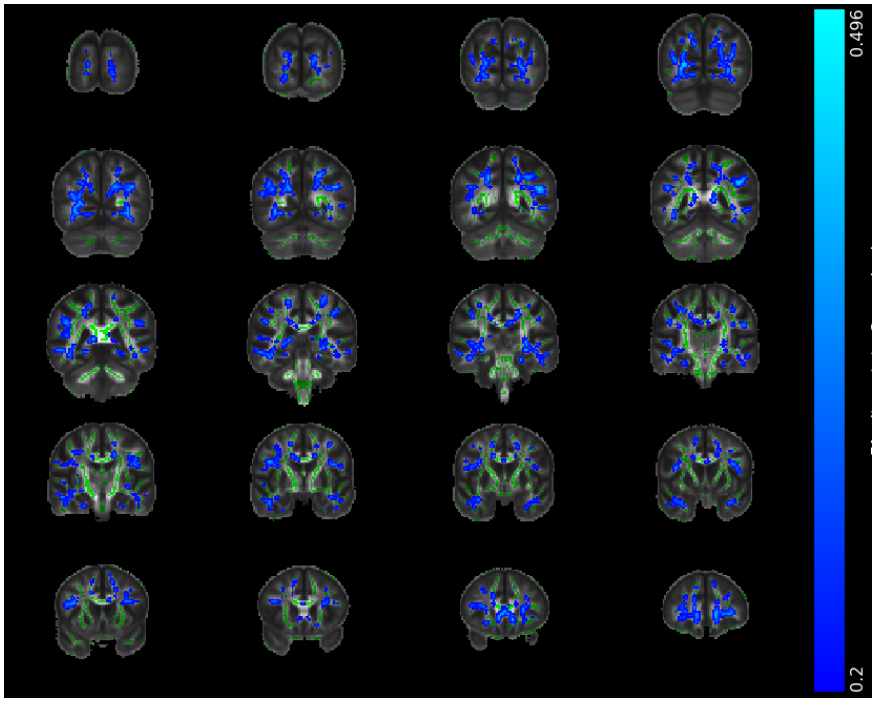

Figure 30: Areas of significant negative correlation between FA and AβL. Results reflect regions with p<0.05 corrected for multiple comparisons and imaging site.

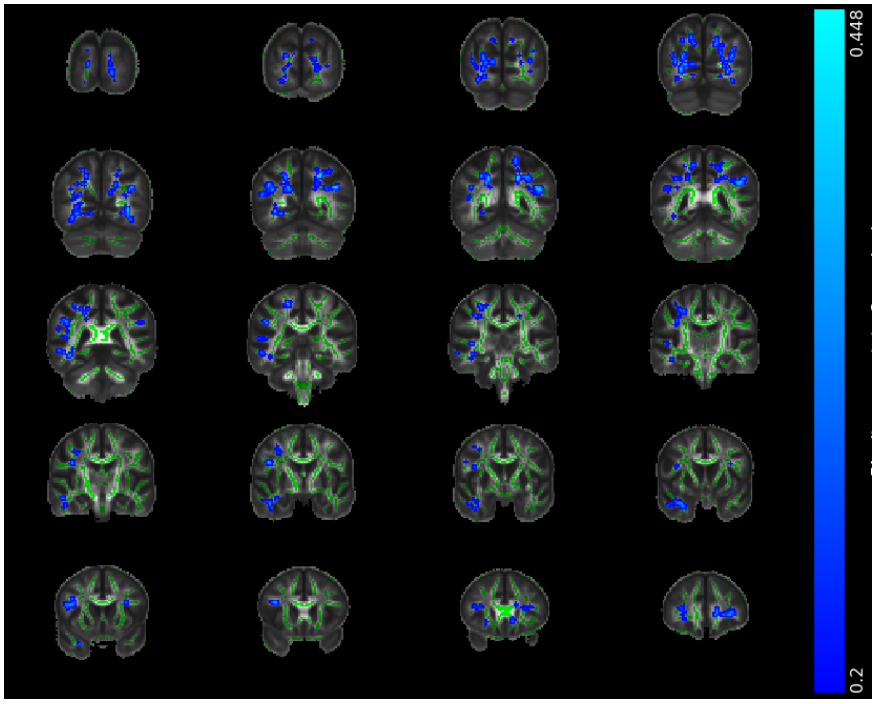

Figure 31: Areas of significant negative correlation between FA and AβL. Results reflect regions with p<0.05 corrected for multiple comparisons, imaging site, and age.

4.4. Discussion

To our knowledge, this is the first study to investigate the white matter microstructural differences based upon amyloid burden in individuals with DS. Our findings reveal a positive relation of MD with amyloid over most of the association white matter pathways. Further, our cohort exhibited diffuse negative associations of FA with $A\beta_L$ in the bilateral occipital parietal and prefrontal white matter, the genu of the corpus callosum, and right temporal white matter and right superior longitudinal fasciculus. Site was included as a co-variate, with significant site effects found in the cerebellum, brainstem, the posterior-inferior WM tracts for FA and the corpus callosum and corona radiata for MD. Importantly, independent analyses for each site showed similar correlations of interactions of FA and MD with $A\beta_L$. Since effects were preserved in the individual site analyses, we conclude that a site covariate within the GLM

was sufficient to mitigate scanner-specific effects and no further data harmonization was needed.

Caballero et al. 2020 observed a significant amyloid-age interaction of MD and white matter hyper intensity volume in a cohort of non-DS, non-AD individuals, which suggested accelerated neurodegeneration in subjects with greater amyloid and is in line with our findings in aging DS(Caballero et al., 2020). It is well documented in geriatric imaging studies that white matter FA decreases with age and MD increases (Abe et al., 2002; Bennett et al., 2010; Hsu et al., 2008). Given the trend of FA to decrease and MD to increase in prodromal and fully realized AD relative to healthy controls, our findings suggest that DS individuals with significant amyloid show signs of neurodegeneration, similar to the findings of Cabrello et al. (2020).

The association between white matter microstructure and amyloid burden using PiB PET in aging (non-DS) was investigated by Racine et al.,(2014) and found paradoxical increased FA and decreased MD in the PiB(+) group. Subsequently, Wolf et al.(2015) found increased FA and decreased MD accompanying low amyloid plaque burden but this was reversed for individuals with high amyloid burden with decreased FA and increased MD. Increased CSF measured Aβ42 was associated with increased MD in gray and white matter in the frontal, parietal, occipital, and temporal lobes in healthy aging adults at risk for AD (Bendlin et al., 2012). Many, but not all of these areas are likewise related to the white matter microstructural changes observed in our DS cohort.

A potential contributing factor to our findings is the presence of cerebrovascular disease, particularly microbleeds (MB). MBs have been observed to occur at a higher rate in DS populations and to contribute to increased cerebral amyloid angiopathy (CAA)(Head et al., 2017; Helman et al., 2019). MBs and CAA may be linked with Aβ accumulation and AD

onset(Noguchi-Shinohara et al., 2017). In non-DS populations, both CAA(Chen et al., 2007) and MBs(Akoudad et al., 2013) have been reported to influence diffusion metrics and indicate signs of decreased WM structural integrity. Since DTI is sensitive to both MBs and AD related brain changes, our results may reflect the contributions of both cerebrovascular disease and the presence of Aβ plaques.

Our findings of significant diffuse $A\beta_L$*age interactions highlight the complexity of uncoupling DTI, amyloid and age and warrant further study within DS and non-DS subjects alike. Since both DTI and amyloid measures are related to aging, larger, longitudinal cohort studies with more balanced age distributions will be required to disambiguate age and amyloid burden effects on DTI measures. These interaction effects, however, suggest that increased amyloid burden is associated with more rapid age-related changes in white matter microstructure.

5. White matter microstructure associations with episodic memory in adults with Down syndrome: A tract-based spatial statistics study

Portions of this chapter have been published in the Journal of Neurodevelopmental Disorders in April 2021. (Bazydlo, A., Zammit, M., Wu, M., Dean, D., Johnson, S., Tudorascu, D., Cohen, A., Cody, K., Ances, B., Laymon, C., Klunk, W., Zaman, S., Handen, B., Alexander, A., Christian, B., & Hartley, S. (2021, 2021/04/20). White matter microstructure associations with episodic memory in adults with Down syndrome: a tract-based spatial statistics study. *Journal of Neurodevelopmental Disorders, 13*(1), 17. https://doi.org/10.1186/s11689-021-09366-1)

5.1. Background

Down Syndrome (DS) is a genetic disorder caused by full or partial trisomy 21 and is associated with a host of physical and developmental problems including intellectual disability, congenital heart disease, hypotonia, thyroid disorders, and sleep problems (Antonarakis et al., 2020). People with DS also have several neuroanatomical brain differences from typically developing populations, including brachycephaly, ventriculomegaly, regional hypoplasia, and decreased depth and reduced number of cerebral sulci (Annus et al., 2017). DS is also associated with an increased prevalence and early onset of Alzheimer's disease (AD) purportedly due to the triplication of the amyloid precursor protein (APP) gene, located on chromosome 21, which causes an over-expression of amyloid-beta (Aβ). The extracellular accumulation Aβ plaques in the brain is one of the early hallmarks of AD (*Down Syndrome: Condition Information*, 2012; Zigman et al., 2008). The genetic linkage of increased amyloid production in DS to increased AD risk is most similar to the development of autosomal dominant AD in non-DS populations, which account for only 1% of AD cases as opposed to sporadic AD which accounts for 90% of total cases (Bateman et al., 2011; Bekris et al., 2010). Population-based studies suggest that over half of adults with DS aged 55 years and older receive

a clinical AD diagnosis (Rubenstein et al., 2020), with the lifetime risk of clinical AD in DS is approximately 90%(McCarron et al., 2014). There is a critical need for natural history studies to characterize early biomarkers of pathological changes of Alzheimer's disease in the Down syndrome population and understand the relationship of these biomarkers to cognitive declines in order to inform clinical trials aimed at delaying or preventing AD in this at-risk population (Neale et al., 2018).

Positron emission tomography (PET) imaging studies have recently been used to characterize the early accumulation of Aβ using the biomarker [^{11}C] Pittsburgh Compound-B (PiB) in adults with DS prior to onset of clinical AD. These studies found that a subset of adults with DS evidence marked Aβ accumulation (referred to as PiB (+)), typically beginning in the striatum, by their fourth decade of life with the majority being PiB (+) by the middle of their fifth decade (Annus et al., 2016; Lao et al., 2016). These findings indicate PET imaged Aβ accumulation occurs approximately 30 years earlier in the DS population as compared to general population samples of adults without a genetic risk for AD (Annus et al., 2016; Lao et al., 2016).

Although AD is often considered a disease of gray matter, white matter (WM) degeneration is evident in adults diagnosed with clinical AD (Mayo et al., 2018; Mayo et al., 2017; Nowrangi et al., 2013) and is also observed during the preclinical stage (i.e., prior to onset of clinical AD) and thought to result from the presence of extracellular Aβ plaques followed by intracellular neurofibrillary tangles of the protein tau (Mayo et al., 2017; Nowrangi et al., 2013; Nowrangi et al., 2015; O'Dwyer et al., 2011). Diffusion Tensor Imaging (DTI) is a non-invasive magnetic resonance imaging (MRI) technique that probes microstructural differences in water diffusion properties of biological tissue

(Basser et al., 1994b; Basser & Pierpaoli, 1996; *Down Syndrome: Condition Information*, 2012; Pierpaoli & Basser, 1996) and has been used to examine WM change associated with AD in both the DS (Neale et al., 2018; Powell et al., 2014) and non-DS populations (Bendlin et al., 2012; Racine et al., 2014). DTI measurements include the mean diffusivity (MD), which is the directionally averaged diffusivity and is sensitive to the density of microstructural features; and the fractional anisotropy (FA), which is a summary measure of the directional variance of diffusivities and is often used as a sensitive marker of WM microstructural changes (Alexander et al., 2007).

Across studies of non-DS populations, adults with clinical AD have been found to evidence increased MD and decreased FA across multiple brain regions (Mayo et al., 2018; Mayo et al., 2017; Nowrangi et al., 2015). Moreover, WM integrity has been found to be associated with cognitive decline and, more specifically, impaired episodic memory in non-demented adults from non-DS populations (Acosta-Cabronero & Nestor, 2014; Mayo et al., 2018; O'Dwyer et al., 2011). For example, Nicholas et al. (2020) found that increases in frontal MD across time were associated with decreases in the ability to correctly recall words (i.e., free recall) in older adults without AD (Nicolas et al., 2020). Remy et al. (2015) found an association between lower FA in the medial temporal lobe and worse episodic memory in older adults without AD (Rémy et al., 2015). Similarly, Metzler-Baddeley et al. (2011) showed that better WM integrity (increased MD and decreased FA) in the fronto-temporal lobe was associated with better episodic memory in older adults without AD (Metzler-Baddeley et al., 2011). Lastly, Lockhart et al. (2012) found associations between lower FA and worse episodic memory across younger and older adults without AD throughout major association fibers, including the superior

longitudinal fasciculus, inferior longitudinal fasciculus, the cingulum bundles, uncinate fasciculus, and thalamo-cortical projections (Lockhart et al., 2012).

In previous work from our own research group, we found evidence that WM integrity may also be impacted early on in AD in the DS population. Specifically, WM integrity assessed using DTI was negatively associated with PET Aβ using PiB in 65 non-demented adults with DS. Adults with DS who were PiB (+) in the striatum and/or neocortex had a higher level of WM insult than did those without marked accumulation (PiB (-)). These differences occurred for both MD and FA along the major association tracts including superior longitudinal fasciculus, inferior longitudinal fasciculus, the cingulum, and uncinate fasciculus (Patrick et al., 2019a, 2019b). Building on these findings, it is now important to determine if WM integrity is associated with declines in episodic memory, which also occur early on in the transition to dementia in DS (Acosta-Cabronero & Nestor, 2014; Cerciello et al., 2017; Wagner et al., 2012) and thus may be an informative biomarker of the transition to the prodromal stage of AD in DS.

Given the large number of neuroanatomical abnormalities in DS and the role of overproduction of Aβ in the development of AD in DS**,** it is not clear if WM impairments are involved early on in AD in DS and if DTI is a meaningful biomarker of WM differences linked to AD-related cognitive change in this population. The goal of the present study was to examine the association between DTI measured WM integrity and directly-administered measures of episodic memory in 52 adults with DS. We hypothesized that WM integrity, as characterized by FA and MD in the major association tracts (superior longitudinal fasciculus, inferior longitudinal fasciculus, the cingulum, and uncinate fasciculus), would be associated with episodic memory performance. Analyses were conducted with and

without controlling for chronological age and premorbid cognitive ability. Given that data come from two study sites, we also added a control variable for site in analyses.

5.2. Methods

5.2.1. Participants

Consent or assent for study participation was obtained from all adults with DS. Proxy consent was obtained from caregivers who served as legal guardians. This study was performed under the approval of the institutional review boards for human subjects research. Seventy (N=70) participants (M = 40.13, SD = 7.77 years) received baseline scans as part of the Neurodegeneration in Aging Down Syndrome (NiAD) study at two imaging facilities (36 at the University of Wisconsin-Madison [UW-Madison] and 34 at the University of Pittsburgh Medical Center [UPMC]). All participants had genetically confirmed trisomy 21. Subject demographic information is presented in Table 1. Eighteen (n=18) participants were excluded due to excessive motion during the DTI acquisition and removed from analyses. Of the remaining participants, forty-six (n=46) participants were classified cognitively stable and three (n=3) were classified as having mild cognitive impairment (MCI) and three (n=3) were diagnosed with dementia. These clinical status determinations were based on a case consensus process that included at least three staff with clinical expertise who were blind to MRI and PET imaging data. The following information was used in the case consensus process: a) medical/psychiatric history and neurological exam; b) caregiver-report of participant's functioning and life events; c) participant's adaptive skills on the Vineland Adaptive Behavior Scales (Sparrow et al., 1984); d) caregiver-report of participant's

dementia symptoms on Dementia Questionnaire for People with Learning Disabilities (Evenhuis, 2018) or Dementia Scale for Down syndrome (J. V. Haxby, 1989); e) participant's profile on the Down Syndrome Mental Status Examination (James V Haxby, 1989), Developmental Test of Visual-Motor Integration, 5th Edition (Beery, 2004), Wechsler Intelligence Scale for Children (Wechsler, 1945) Block Design and Haxby extension (J. V. Haxby, 1989), and Developmental NEuroPSYchological Assessment (Brooks et al., 2009) Word Generation Semantic Fluency. Informed consent was obtained prior to data collection.

	Total (N=52)	**MCI (N=3)**	**Dementia (N=3)**
Subjects Imaged at UW	36	3	0
Subjects Imaged at UPMC	34	0	3
Females (%)	24 (46.15%)	0 (0%)	1 (33%)
Age in years (SD)	39.13 (7.77)	45.53 (3.59)	50.47 (5.26)
RSPPV (SD)	122.20 (34.63)	131.33 (24.58)	84.00 (17.78)

Table 1: Subject Demographic Information

5.2.2. Diffusion Tensor Imaging

Magnetic resonance imaging (MRI) data were collected on two 3.0T MRI scanners - a GE SIGNA 750 with an 8-channel head coil (UW-Madison) and a Siemens Magnetom Trio scanner with a 64-channel head coil (UPMC). Diffusion-weighted imaging at both sites was performed using a single-shell, diffusion-weighted spin echo sequence (UW-Madison TR/TE = 7800/67ms; UPMC TR/TE = 7200/56ms). The DWI protocol consisted of either 7 (UPMC) or 6 (UW-Madison) non-diffusion weighted (b_0) images and diffusion weighted images with a b-value of 1000s/mm^2 in 48 non-collinear directions. Additional imaging parameters consisted of matrix size: and 116 x 116 with 80 slices, field of view: 23.2 x 23.2 x 16 cm^3, and 2mm slice thickness. Data were processed using an in-house processing

pipeline utilizing tools from FSL(Jenkinson et al., 2012), Mrtrix(Tournier et al., 2019), and the DiPy toolbox(Garyfallidis, Brett, Amirbekian, Rokem, van der Walt, Descoteaux, Nimmo-Smith, et al., 2014). The diffusion-weighted data were corrected for Gibbs' ringing artifacts(Kellner et al., 2016), Rician noise(Veraart et al., 2016), and eddy current distortions and head motion with outlier replacement(Andersson et al., 2016; Andersson & Sotiropoulos, 2016). A threshold of 10% or more of slices replaced as outliers within a single diffusion weighted image (DWI) was established as a criterion for removal of a volume; however, no volumes exceeded this threshold and no DWIs were removed. The diffusion tensors were estimated using a robust estimator method, RESTORE (Chang et al., 2005), and FA and MD maps subsequently calculated.

All FA data in the study were aligned to a 2mm isotropic population derived FA template using ANTs(Avants et al., 2011). This template was constructed using amyloid negative participants without MCI or AD. A medial surface skeleton was generated from the population averaged FA image. Each participant's regional maximum FA data were then projected onto this skeleton surface for voxel-wise statistical analyses. The MD maps were likewise spatially normalized and projected onto the FA skeleton for analysis. The JHU white matter atlas labels(Oishi et al., 2008) were warped to the population derived FA template using ANTs (Avants et al., 2011).

5.2.3. Episodic Memory Composite Measure

A composite score of episodic memory was calculated based on two measures of episodic memory .The first was the Free and Cued Recall test (Buschke, 1984), a measure of verbal episodic memory in which participants attempt to learn and remember 12 pictures that are linked to categories (e.g., fruit). The Free and Cued Recall score is the number of pictures recalled across

three free trials and three cued recall trials (i.e., category is given). The second measure was the Rivermead Behavioural Memory Test for Children Picture Recognition (Aldrich & Wilson, 1991), a measure of visual episodic memory obtained by determining if participants are able to distinguish 10 pictures previously presented from 10 pictures not previously seen after a brief delay. The total score is the number correctly recalled minus the number of false positives. These two scores (Free and Cued Recall total and Rivermead Total) were z-scored and summed to create the composite measure used in the present study. The decision to use this composite measure of episodic memory was based on a principal component analysis involving five measures - Free and Cued Recall, Rivermead, Developmental NEuroPSYchological Assessment (NEPSY) Visual Attention and Verbal Fluency tasks (Brooks et al., 2009), and the Beery Visual-Motor Integration (Beery, 2004). The first principal component was made up of the Free and Cued Recall, and Rivermead scores and explained over 50% of the variance. Moreover, both of measures have been shown to be sensitive to other biomarkers of early AD in adults with DS (e.g., Hartley et al., 2014).

5.2.4. Control Variables.

Sociodemographic variables and study site were included in models to account for any effect on WM and episodic memory. Chronological age in years was reported by caregivers. Premorbid (i.e., prior to any concerns of MCI or AD) cognitive ability was assessed using the Peabody Picture Vocabulary Test (Dunn, 2007), which assesses receptive language ability and has been shown to be strongly associated with lifetime global cognitive ability (Phillips et al., 2014). The mental age equivalent score was used in analyses. Imaging site was coded as Wisconsin = 1 and Pittsburgh = 2 to allow us to control for any differences in WM or episodic memory based on site.

5.2.5. Statistical Analyses

The distribution of variables and histograms of residuals were used to assess use the normalcy of data and to identify any outliers. Statistical analyses of the DTI data were performed using the tract-based spatial statistics pipeline in FSL(Smith et al., 2006; Smith et al., 2004). All FA data in the study were aligned to a population derived FA template using ANTs(Avants et al., 2011). A medial surface skeleton was generated from the population averaged FA image. Each participant's regional maximum FA data were then projected onto this skeleton surface for voxel-wise statistical analyses. The MD maps are likewise spatially normalized and projected onto to the FA skeleton for analysis. The JHU white matter atlas labels(Oishi et al., 2008) were warped to the population derived FA template using ANTs(Avants et al., 2011).

Pearson partial correlation analyses were performed using a general linear model in FSL. The model consisted of the episodic memory composite score, as well as the following control variables – chronological age, imaging site, and premorbid mental age equivalent score. Voxel-wise partial correlation analysis of the tract-based spatial statistics (TBSS) derived data and episodic memory composite score (EMCS) using the above GLM was performed using the permutation analysis of linear models (PALM) package from FSL with 2D threshold-free cluster enhancement (TFCE) optimization (Winkler et al., 2014). Correction for multiple comparisons was performed by controlling for the Family-Wise Error rate (Smith & Nichols, 2009).

5.3. Results

The episodic memory score was found to be near normal (kurtosis=0.460) and with minimal skew (Pearson's mode skewness = -1.270). Figure 32 shows the significant negative correlations between the episodic memory composite with MD. MD data are

shown at a multiple comparisons corrected significance of $p<0.05$, with additional covariates for imaging site, premorbid cognitive ability, and chronological age. These covariates were used to address variation between scanners (imaging site), the understanding of the task (premorbid cognitive ability), and the association of chronological age and DTI measures. Significant associations were observed bilaterally throughout the superior and inferior association fibers (see Table 2): superior longitudinal fasciculus (left: r=-0.399, p=0.005 FWER corrected; right: r=-0.444, p=0.001 FWER corrected) as well as in the inferior longitudinal fasciculus (left: r=-0.504, $p<0.001$ FWER corrected; right: r=-0.452, p=0.001 FWER corrected). We also examined FA within these regions and found significant associations bilaterally in the superior longitudinal fasciculus (left: r=0.280, p=0.051 FWER corrected; right: r=0.332, p=0.020 FWER corrected) as well as in the inferior longitudinal fasciculus (left: r=0.292, p=0.042 FWER corrected; right: r=0.372, p=0.008 FWER corrected). All reported ROIs were extracted using a mask of the significant voxels reported in Figure 1 within JHU WM atlas labels provided by FSL(Jenkinson et al., 2012; Oishi et al., 2008). No significant negative correlations with FA or positive associations with MD were observed. Note that data are presented using the 'tbss_fill' method provide by FSL, and inflated regions reflect areas significant at a multiple comparisons corrected $p<0.05$. As a follow-up analysis, we re-ran the above model after removing the subjects with MCI or AD. The overall pattern of results remained the same. The inferior longitudinal fasciculus MD(Left: r=-0.451(p=0.002); Right: r=-0.339(p=0.026)), superior longitudinal fasciculus MD (Right: r=-.305(p=0.047)), inferior longitudinal fasciculus FA(Left: r=0.292(p=0.057); Right: r=0.407(0.007)), and superior longitudinal fasciculus FA (Left: r=0.28(p=0.076); Right: r=0.370(p=0.015)) regions

remained significantly associated with episodic memory after correction for chronological age, site, and premorbid cognitive ability. The global regions (FA: r=0.201(p=0.196); MD: r=-0.376(p=0.013)) had trend-level associations with episodic memory after correcting for chronological age, site and premorbid cognitive ability. Thus, the inclusion of the MCI and AD participants did not appear to be driving findings.

Though voxelwise associations with FA did not survived at an $\alpha=0.05$ level, positive correlations between FA and EMCS were observed at $p<0.08$ corrected for chronological age, imaging site, and premorbid cognitive ability (See Figure 33A). We also tested the correlation between the composite measure and FA only covarying for imaging site and premorbid cognitive ability and observed diffuse regions of positive correlation of the composite score with FA at $p<0.05$ FWER corrected (See Figure 33B). The extent of these regions throughout the association tracts is quite similar to the extent observed for MD in Figure 32.

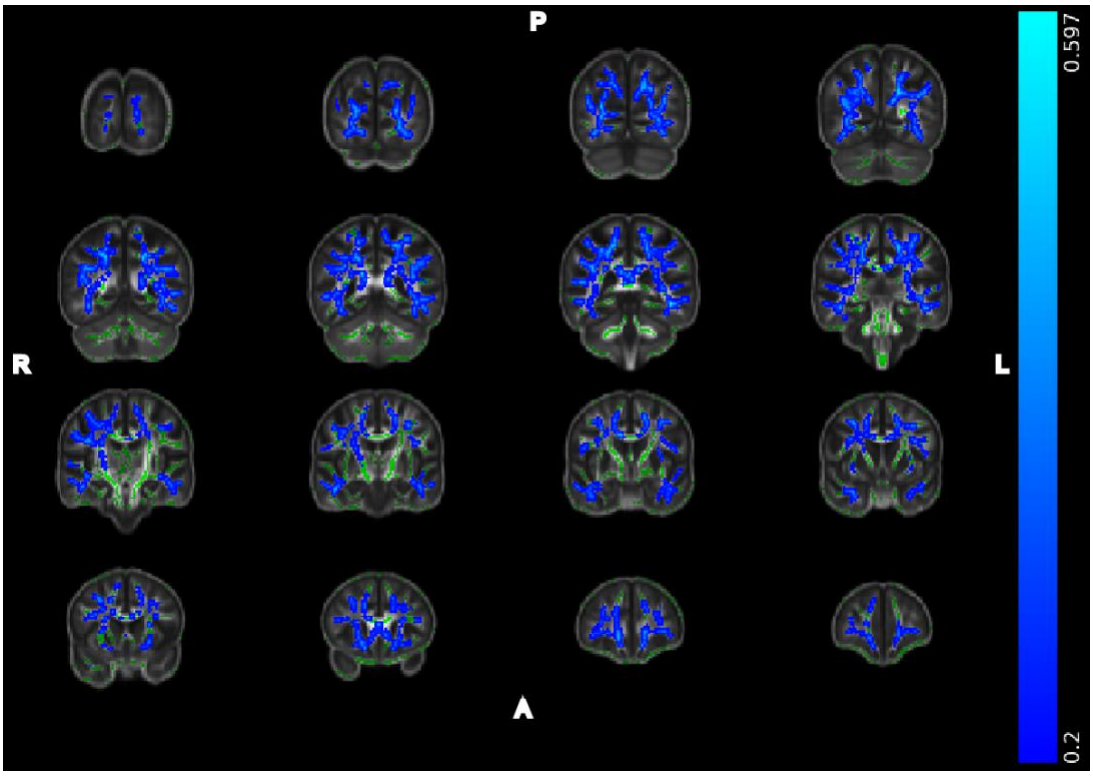

Figure 32: Regions of significant negative correlation between EMCS and MD. Images arranged in right to left (R-L) and posterior to anterior (P-A). Images overlaid on the population derived FA skeleton (green) and the population derived 2mm FA template. Regions shown reflect areas with Pearson's r less than -0.2. Data shown at a FWER corrected $p<0.05$ with covariates for premorbid cognitive ability, imaging site, and age.

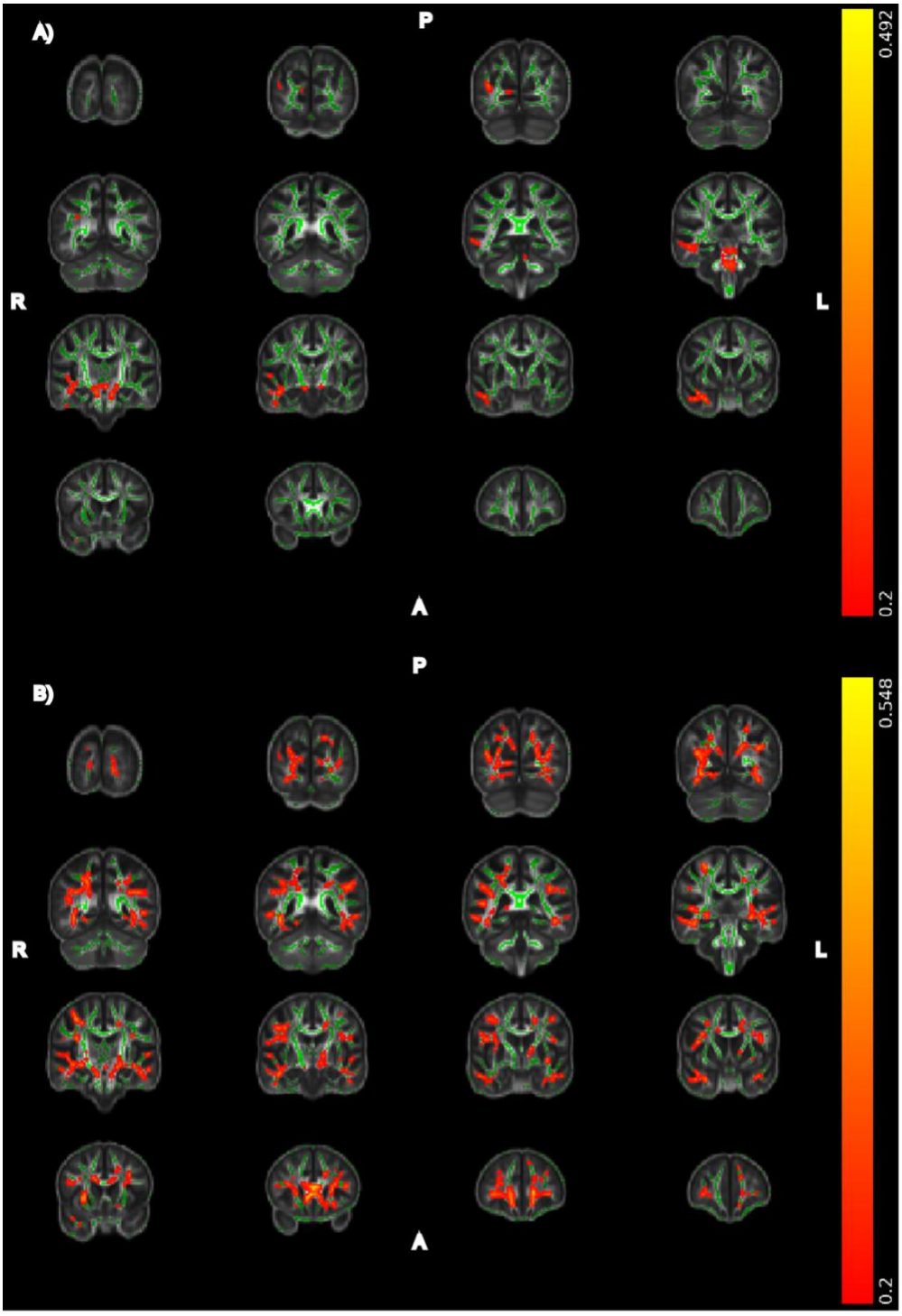

Figure 33: A) Regions of significant positive correlation between EMCS and FA at p<0.08 FWER corrected and controlling for chronological age, imaging site, and premorbid cognitive ability. B) Regions of significant positive correlation between EMCS and FA at p<0.05 FWER corrected and controlling for imaging site and premorbid cognitive ability. Images arranged in right to left (R-L) and posterior to anterior (P-A). Images overlaid on the population derived FA skeleton (green) and the population derived 2mm FA template. Regions shown reflect areas with Pearson's r less than -0.2. Data shown at a FWER corrected p<0.05 with covariates for premorbid cognitive ability, imaging site, and age

	Pearson's r (p-value*)	
Global FA and EMCS	0.341(0.017)	
Global MD and EMCS	-0.547(<0.001)	
	Left Hemisphere	**Right Hemisphere**
ILF FA and EMCS	0.292(0.042)	0.372(0.008)
SLF FA and EMCS	0.280(0.051)	0.332(0.020)
ILF MD and EMCS	-0.504(<0.001)	-0.452(0.001)
SLF MD and EMCS	-0.399(0.005)	-0.444(0.001)

*Table 2: JHU atlas ROI comparisons of DTI parameters and the episodic memory composite score (EMCS). *corrected for Family-wise error rate, imaging site, chronological age, and premorbid cognitive ability*

5.4. Discussion:

Adults with DS are genetically at-risk for AD with AD-related pathophysiology nearly universally present by age 40 years (Annus et al., 2016).There is a critical need within the DS field for imaging studies that can describe the natural history of early AD pathophysiology in DS and its link to cognitive decline in order to inform clinical trials. To our knowledge, the present study is the first to examine the association between DTI measured WM integrity and episodic memory in adults with DS.

Our findings revealed important associations between WM integrity and episodic memory in the DS population. FA was observed to be positively correlated with episodic memory while MD was negatively correlated with episodic memory. There were no significant negative associations between FA and episodic memory nor positive associations between MD and episodic memory. Associations between FA and MD (in positive and negative directions respectively) and worse performance on measures of cognitive ability

including episodic memory have been reported on extensively in the aging literature on non-DS populations (Lockhart et al., 2012; Metzler-Baddeley et al., 2011; Rémy et al., 2015). Further, decreased FA and/or increased MD have been reported in adults without DS who are exhibiting MCI and/or AD relative to healthy controls (Powell et al., 2014; Romano et al., 2018). Our findings serve as a bridge between the cognitive insights of bridge between the previous reports of the central role of episodic memory declines in AD in DS (Hartley et al., 2017; Hartley et al., 2020; Sigan L. Hartley et al., 2014) with the body of DS DTI literature (Neale et al., 2018; Powell et al., 2014; Romano et al., 2018) showing that disruptions of episodic memory in early cognitive decline may arise from the degeneration of association white matter pathways between regions of the brain, particularly frontal, medial-temporal, and parietal lobe areas. Further, our results highlight the clinical potential of DTI, particularly MD, as a non-invasive biomarker to detect early cytoarchitectural changes that may be associated with AD in adults with DS. . If DTI continues to emerge as a useful biomarker of AD-related cognitive change in future studies that are larger and longitudinal, this biomarker has the potential to be informative for participant selection and outcome tracking in AD clinical trials in DS. Indeed, efforts to launch large AD intervention trials in DS are already underway, yet currently involve a limited array of established AD biomarkers. DTI is already an established biomarker in pediatric populations and is used to detect both gray matter and white matter changes arising from neurodevelopmental conditions such as Gaucher's disease (Abdel Razek et al., 2009) and Crigler-Najjar Syndrome (Razek et al., 2020) , illustrating the promise of DTI as a clinically relevant biomarker in rare genetic disorders, such as DS.

There is a tight linkage between chronological age and DTI indices which may have impacted our results (Abe et al., 2002; Provenzale et al., 2010). Indeed, in the current sample, chronological age was correlated with FA in major tracts at $r = -0.482$ ($p<0.001$). However, the FA and MD associations with episodic memory remained even after controlling for chronological age. There is also a coupling of episodic memory performance with premorbid cognitive ability ($r=0.508$, $p<0.001$) and decline with chronological age ($r=-0.491$, $p<0.001$) in our sample. In controlling for chronological age and premorbid cognitive ability, our findings represent the episodic memory changes above and beyond these other effects. Our results suggest a coupling of white matter cytoarchitecture and episodic memory that is independent of chronological age. Further study is needed to understand other factors that may impact this relation.

5.5. Conclusion:

The present study had both strengths and limitations. To our knowledge, this is the largest study examining the association between DTI measures of WM integrity and cognitive functioning in the DS population and is the first to show that WM impairment may be implicated in early declines in episodic memory in DS. There were also limitations to the present study. First, adults with DS are a difficult population to image, due to increased subject motion in the scanner. Indeed, motion led to the rejection of several subjects due to imaging artifacts. Second, larger cohorts and longitudinal studies are needed to tease apart the time-ordered direction of effects of WM impairment and episodic memory with age, as this is not clear given the cross-sectional nature of the present study. Finally, future studies should include biomarkers of Aβ and tau in addition to WM integrity and evaluate whether

WM impairment influences cognitive function that is independent from these other aspects of AD pathophysiology.

6. Insights into young adult brain plasticity using diffusion weighted imaging and videogame training

6.1. Background

Neuroplasticity or plasticity refers to the ability of the brain to adapt and change in response to experiential and environmental factors. Mechanisms for these changes include the genesis of neurons and glial cells, as well as modification of existing connections via synapse formation and elimination, dendritic remodeling, and axonal sprouting between brain regions related to the planning or performance of a given task (Jill L. Kays et al., 2012). Long standing notions in the study of brain plasticity have been 1) the importance of the critical period from infancy to adolescence when the brain has been observed to be most plastic and 2) that brain plasticity largely stabilizes in late adolescences to adulthood (Voss et al., 2017). Recent studies have begun to dispute the latter notion, leading to the emerging view that the brain retains significant plasticity throughout the lifespan and that a variety of forms of behavioral training can induce clear neuroplastic changes (Voss et al., 2017).

While the growing body of plasticity literature has produced numerous interesting results, the periods of observation have been mostly on the order of hours and have focused largely on a single task. With the utility and controlled environment available with videogame training, we hoped to test the specificity of two videogame task designs to evoke task-specific WM microstructure changes both in the short and long term. For this study, two videogames were chosen: Guitar Hero (GH) ("Guitar Hero," 2009) and Need-for-Speed (NFS) ("Need for Speed: Shift," 2009), due to the difference of objectives between the two games. GH emulates playing an electric guitar and presents a series of color-coded notes and strum durations, which the player must match on a guitar shaped controller. The goal of GH is to synchronize ones playing with the

presented stimuli as accurately as possible. The objective for NFS is to complete a closed course as quickly as possible. The goal of this study was to provide a comprehensive, multimodal neuroimaging assessment of long-term microstructural brain changes as an indication of neuroplasticity and learning in a cohort of normally developing, college-aged subjects that have been rigorously trained on highly complex and active video games. We employ both conventional DTI and the more advanced NODDI measures in our assessment. It is further hypothesized that long-term learning will result in increased FA and neurite density index (NDI), as well as decreased MD in task-associated regions, indicative of more restricted diffusion and tighter axonal packing. It is believed that the two training groups, will exhibit measurable changes in regions associated with spatial map and motor learning, respectively. Spatial map learning is most largely associated with medial-temporal lobe areas, the hippocampus, cingulate cortex, and fornix (Libby et al., 2014; Schiller et al., 2015), while motor learning will impact regions associated with lateralized operation and motor planning of the left hand (Sampaio-Baptista et al., 2013; Wang et al., 2014).

6.2. Methods

A total of sixty (N=60) participants were recruited for study. There were 44 females and 16 males. Ages ranged from 18 to 24 years with an average age of 20.58 ± 3.02 years. Informed written consent was provided by each participant prior to study participation. This study was performed under the approval of the institutional review boards for human subjects research. Twenty (N=20) participants were assigned to each the Guitar Hero (GH), Need-for-Speed (NFS), and control groups, respectively. The sample sizes were based upon the study design described by Sagi et al. (2012) and subsequently a similar study by Keller and Just (2016). Participants in the GH group played *Guitar Hero ("Guitar Hero," 2009)*, which

simulated the playing of a guitar using a variety of popular songs across multiple musical genres. The goal of the game is to accurately match color coded notes and strumming in correct order, duration, and timing. GH participants used a proprietary guitar emulating controller. To maximize visuo-spatial working memory and motor planning, no song was repeated by a given participant over the training period. Participants in the NFS group played *Need for Speed: Shift ("Need for Speed: Shift," 2009)*. The goal of the NFS game is to complete as many laps on a course as quickly as possible. To maximize spatial route learning, participants completed the same track for 16 laps in each session. After every 4 laps, the participant was asked to sketch the course and arrange screen captures of the track in the proper order. NFS participants used an accessory controller that included steering wheel, clutch, and throttle apparatuses; although, the clutch was not used. Training group participants completed a total of ten hours of training over the course of four weeks. Training was completed using an Xbox 360 (Microsoft). Control participants completed all imaging and behavioral assessments with no video game training. Imaging was performed at three times for each participant: Time 1 (baseline), Time 2 (90 minutes after baseline, post training for NFS and GH groups), and Time 3 (~4 weeks after baseline with 15 hours of training for the NFS and GH groups).

All imaging was acquired using a 3T GE Discovery MR750 (GE, Waukesha, WI) at the Waisman Brain Imaging Laboratory using a 32-channel head RF coil. DWI acquisitions for use with the DTI and NODDI models were acquired at 2 mm isotropic resolution with b= 350, 800 and 2000 $s \bullet mm^{-2}$ with 9, 18, and 36 directions in each shell, respectively, for a total of 63 encoding directions and 6 non-diffusion weighted (b=0) images. Additional acquisition parameters included: TE/TR = 77/8575 ms; matrix size = 128 x 128, and number of slices = 70.

External B_0 fieldmaps were acquired to correct for main magnetic field inhomogeneity distortions.

Subjects received baseline MRI scan at Time 1 (T1). Active training participants then completed 90 minutes of training of their assigned games, after which they received a scan at Time 2 (T2). Active learning participants completed 15 total hours of training across ten 90-minute training sessions over 3-4 weeks, shortly after which they received a scan at Time 3 (T3). Control participants completed no videogame training but completed all imaging at the same time intervals.

Data were processed using an in-house processing pipeline built utilizing DiPy (Garyfallidis, Brett, Amirbekian, Rokem, van der Walt, Descoteaux, & Nimmo-Smith, 2014), FSL (Jenkinson et al., 2012), and MRTrix3 (Tournier et al., 2019). Skull stripping was performed using FSL's brain extraction tool (BET) (Smith, 2002). Correction for Rician noise was performed using the MRTrix3 dwidenoise tool (Cordero-Grande et al., 2019; Veraart et al., 2016), as well as correction for Gibbs ringing (Kellner et al., 2016). FSL's *eddy* command was used for eddy current and motion correction with outlier detection and replacement; volumes with more than 10% of volumes labelled as outliers were removed (Andersson et al., 2016; Andersson & Sotiropoulos, 2016). Susceptibility distortions were corrected for using a separately acquired fieldmap and warping the DWIs using the FSL *fugue* tool (Jenkinson et al., 2012). DTI maps were calculated using the DiPy processing toolkit using a weighted linear least squares estimation. NODDI maps were calculated using the DMIPY package's estimation of the NODDI model (Fick et al., 2019; Zhang, Schneider, et al., 2012). All preprocessing and modeling steps were implemented using the DiPy(Garyfallidis, Brett, Amirbekian, Rokem, van der Walt,

Descoteaux, & Nimmo-Smith, 2014) and DMIPY(Fick et al., 2019) software packages in Python.

Spatial normalization of the DWI images involved the generation of subject-specific templates using the Advanced Normalization Tools (ANTs) antsMultivariateTemplateConstruction2.sh script (Avants et al., 2011). A bivariate template constructed from each subject's MD and FA maps was determined as the optimal method since FA was found to provide good WM agreement and MD provided good alignment within gray matter. Next, a population template was derived from all 60 subject-specific FA and MD templates. The population FA template was then non-linearly registered to the IIT 1 mm^3 mean FA template (Qi & Arfanakis, 2021; Zhang & Arfanakis, 2018). Subject-to-population and population-to-IIT warps were applied to each subjects' DTI and NODDI maps to bring them into the atlas space. For ROI extraction, the inverse warps were applied to the atlas labels to bring them into the subjects' native spaces. Hippocampus ROIs were extracted using the Harvard-Oxford subcortical atlas labels (Desikan et al., 2006).

A general linear model (GLM) was used to compare T1 to T2 and T1 to T3 within each game group. Data were smoothed using a 5 mm FWHM Gaussian kernel. Voxelwise cross-subject statistical analysis was then performed using FSL's *randomise* (Winkler et al., 2014) with threshold-free cluster enhancement (TFCE) (Smith & Nichols, 2009) for family-wise error correction. Analyses were restricted to group-derived whole brain masks.

6.3. Results

Figs. 35-37 show the maps for the time effect on the DTI measures for the Guitar Hero (GH) group. Figs. 38 and 39 show the statistical maps for the time effect on DTI for the Need for

Speed (NFS) group. Figs 35-39 show the results from a whole-brain voxelwise analysis using TFCE with regions shown at $p<0.01$ uncorrected; all images are shown with (R-L) orientation.

Significant MD decreases were observed from T1 to T2 in much of the lateral occipital cortex and the left angular gyrus for GH (see Figure 35). Also, for GH, MD was found to increase from T1 to T3 in the right parietal and frontal lobe areas, largely in the premotor and supplementary motor areas, as well as the internal capsule and thalamus. NFS observed overlapping regions of MD decrease and NDI increase in the right hippocampus and inferior occipital lobe from T1 to T2. MD was also found to decrease in the superior division of the lateral occipital cortex from T1 to T2. It is important to note that some regions survived at $p<0.1$ FWER corrected and have been provided in Figures 39 and 40. Figure 39 shows similar T1 to T2 MD decreases in GH to Figure 35 but lateralized to the left occipital lobe. Figure 40 shows GH T1 to T3 ODI decreases constrained to the white matter abutting the supplementary motor cortex.

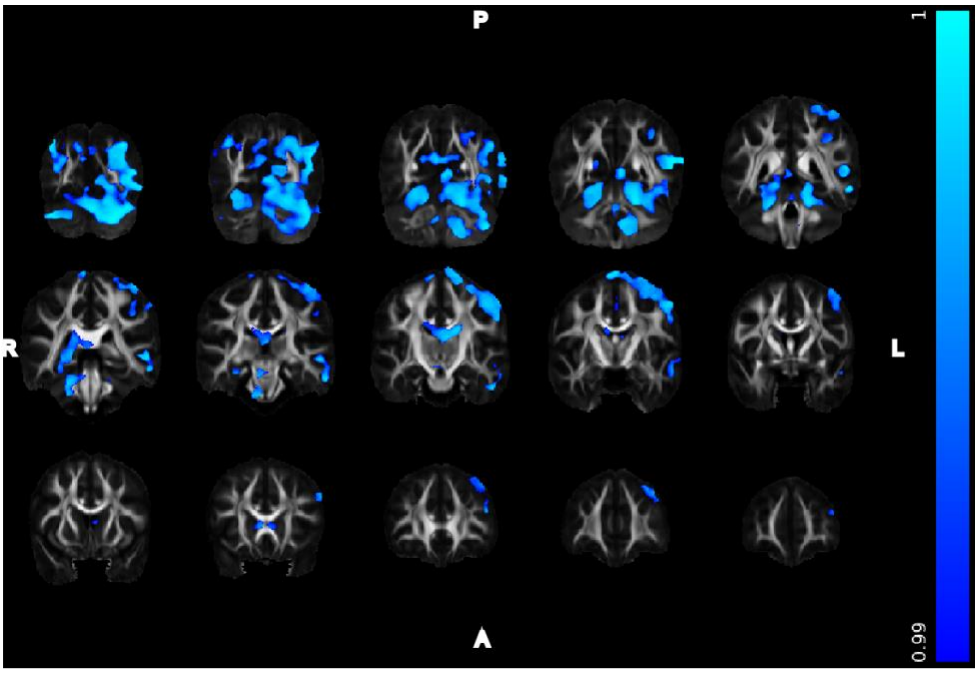

Figure 34: GH MD decreases from T1 to T2 overlaid on the 1 mm^3 IIT FA template. p<0.01 uncorrected.

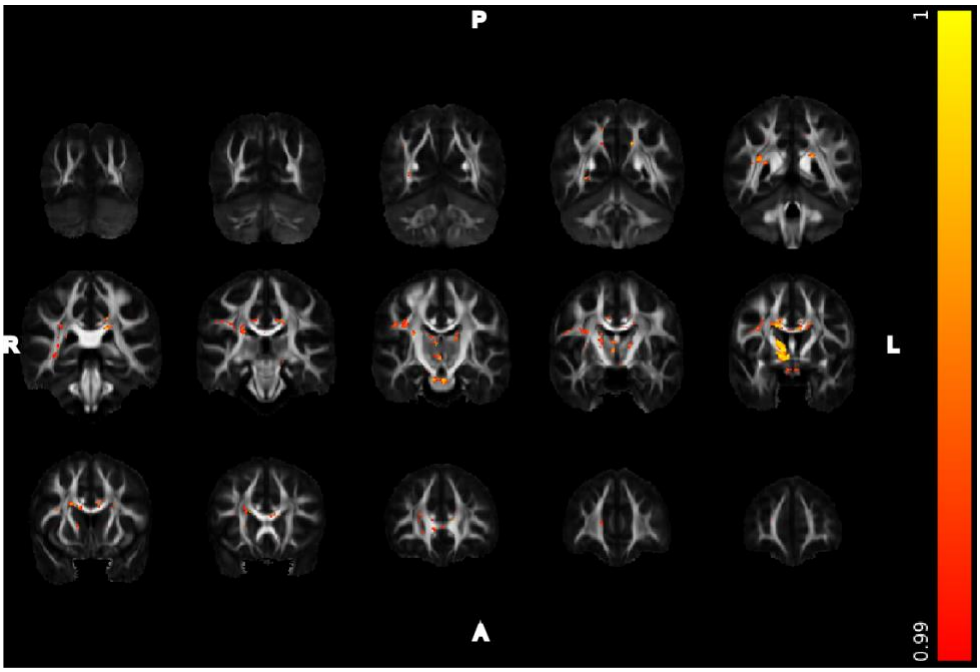

Figure 35: GH MD increases from T1 to T3 overlaid on the 1 mm^3 IIT FA template. p<0.01 uncorrected.

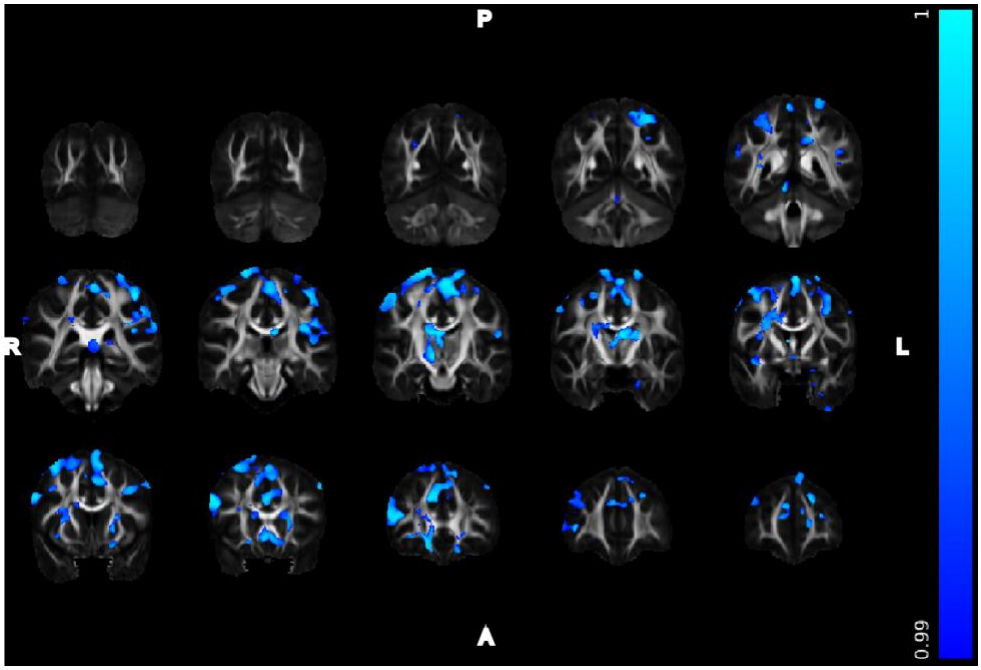

Figure 36: GH ODI decreases from T1 to TT3 overlaid on the 1 mm^3 IIT FA template. p<0.01 uncorrected.

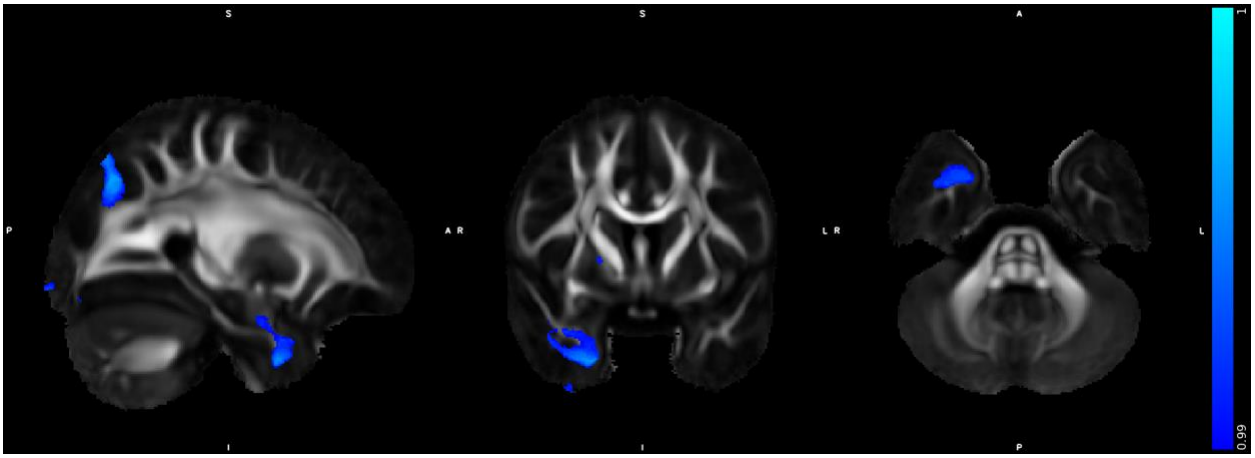

Figure 37: NFS MD decreases from T1 to T2 overlaid on the 1 mm^3 IIT FA template. Representative orthogonal slices p<0.01 uncorrected.

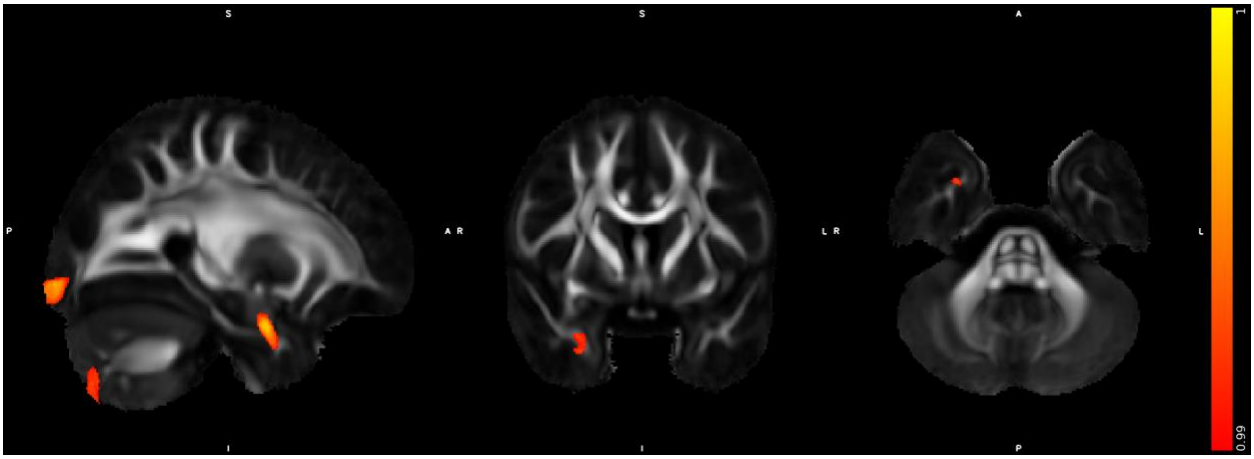

Figure 38: NFS NDI increases from T1 to T2 overlaid on the 1 mm^3 IIT FA template. p<0.01 uncorrected.

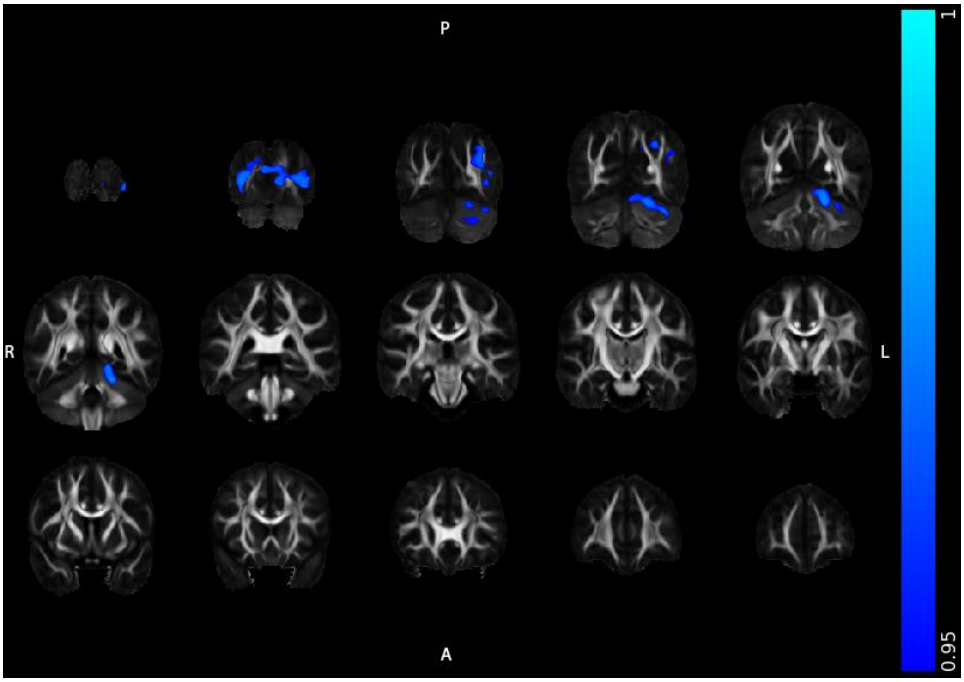

Figure 39: GH MD decreases from T1 to T2 overlaid on the 1mm IIT FA template. 1-p-values corrected for FWE rate using TFCE at a significance of 0.05.

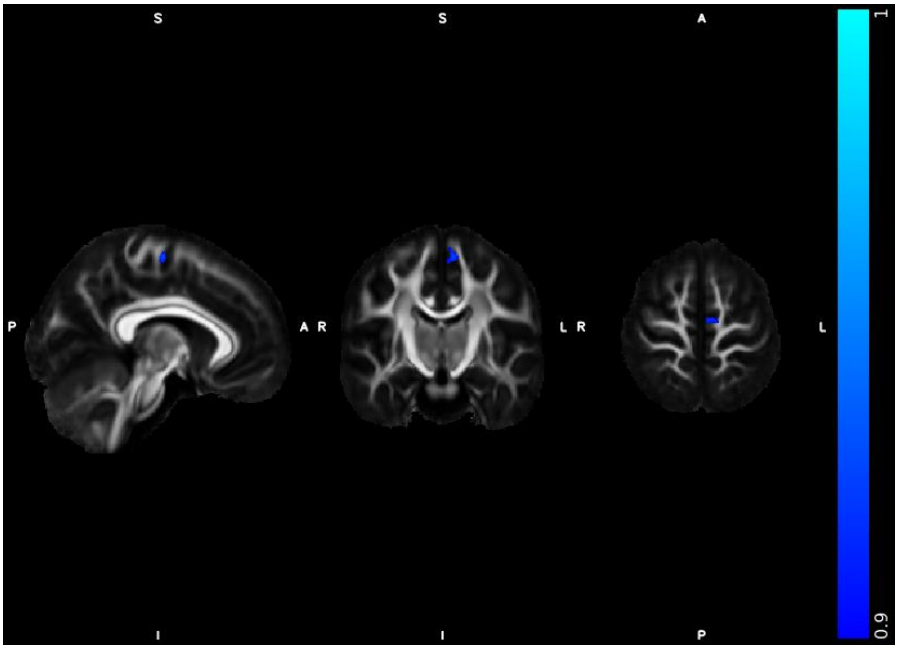

Figure 40: GH ODI decreases from T1 to T3 overlaid on the 1mm IIT FA template. 1-p-values corrected for FWE rate using TFCE at a significance of 0.1.

6.4. Discussion:

In this work, we have explored the utility of diffusion weighted imaging methods, particularly DTI and NODDI, to detect both short-term (~hours) and long-term (~weeks) microstructural changes in young adults. Further, we have explored the utility of targeted videogame training to evoke localized changes in areas related to task design, namely spatial route learning (Need-for-Speed) and motor planning and coordination (Guitar Hero).

The greatest extent of changes was observed in the GH cohort. The lateral occipital cortex is heavily involved in object recognition, retinotopy, and attention (Sayres & Grill-Spector, 2008). Further, the angular gyrus has been observed to play a role in multiple studies of real and imagined playing of musical instruments (Garza-Villarreal et al., 2015; Tanaka & Kirino, 2019). MD was found to increase from time 1 to time 3 in the right parietal and frontal lobe areas, largely in the premotor and supplementary motor areas, as well as the internal capsule

and thalamus, which play a part in the integration of movement and sensory information and motor coordination. The thalamus aids in relaying somatosensory afferents including proprioceptive information from the limbs to the cortex, as well as aiding in directing attention (Hirai et al., 1989; Tokoro et al., 2015). Further, the internal capsule is the subcortical extension of the corticospinal tract and aids in the operation of the limbs and contains somatosensory projections from the thalamus which terminate in the somatosensory cortex (Emos, 2020). Lastly, ODI was found to decrease longitudinally in the GH cohort in the supplementary motor area (SMA). The SMA is thought to play a role in motor planning and learning of complex motor tasks, as the threshold for SMA recruitment is higher than the primary motor cortex, although its exact function is still unknown (Kaas & Stepniewska, 2002).

Changes within the GH cohort suggest a complex integration of visual-motor pathways related to the task. Further, these findings are representative of areas observed in plasticity studies of musicians and those learning to play an instrument (Fields, 2011). In comparing musicians with non-musicians, Han et al. (2009) observed volumetric changes in the somatosensory areas and posterior limb of the internal capsule. Bengtsson et al. (2005) observed similar FA changes in the posterior internal capsule and corpus callosum. MD increase has been observed in improved task performance in a cohort of subjects undergoing white matter training (WMT) compared to controls in several brain regions (Takeuchi et al., 2015). We observed similar MD increases in our longitudinal GH cohort.

Results within the NFS cohort showed overlapping regions of effect from time 1 to time 2 near the hippocampus exhibiting decreased MD and increased NDI. Our results are similar to the findings of Sagi et al. (2012) and Keller and Just (2016) ; however, our findings were not observed at a $p<0.05$ FWER corrected significance. The overlapping weak effects between NDI

and MD suggests the need for greater sample size. A post-hoc analysis of the effect size within a hippocampal region of interest in the NFS cohort from T1 to T2 suggested that the needed sample size to resolve these effects at a significant level of α<0.05 and 80% power was 30 and 28 subjects per group for MD and NDI, respectively.

Neuroplastic changes in the adult brain are small and require neuroimaging techniques that are sensitive to changing tissue microstructure. In the present study, we highlight the sensitivity of diffusion imaging techniques, namely DTI and NODDI, to detecting short-term and prolonged neuroplastic changes in response to distinct spatial-route and motor learning tasks and within specific brain regions. We have shown the ability of diffusion weighted MRI to examine possible neuroplastic changes of the angular gyrus and lateral occipital cortex in just 90 minutes of training playing the Guitar Hero musical instrument simulator, as well as structural changes in the posterior limb of the internal capsule, thalamus, and the premotor cortex in 10 hours of training. Similarly, we observed reorganization near the hippocampus because of spatial route learning in just 90 minutes of training with the Need-for-Speed racing simulation game. Our findings show the utility of DTI and NODDI to examine task-specific neuroplastic responses to video game training.

6.5. Neuroplastic Changes Measured Using R1

6.5.1. Background

Previous studies have reported gray matter structural changes resulting from video game training using T1-weighted imaging (Kühn et al., 2014). R1 (1/T1) relaxometry provides useful microstructural information, particularly myelin content, although not exclusively as it is sensitive to iron content and axonal density (Alexander et al., 2011; Lazari & Lipp, 2021). Further, R1 has not been studied in tandem with videogame training. The state-of-the-art magnetization-prepared n-rapid acquisition gradient echoes (MPnRAGE)(Kecskemeti et al., 2016) sequence is to able produce hundreds of T1 contrasts and calculate accurate and reproducible T1 and R1 maps, which were used in this study. In this work, we analyzed neuroplastic changes of R1 observed as a result of long-term videogame training in a cohort of typically developing, college-age participants.

6.5.2. Data Acquisition and Preprocessing

All participants described in the DTI and NODDI section above were also imaged using the MPnRAGE sequence (Kecskemeti et al., 2016) during the same imaging sessions. Scanning was performed on a 3T scanner (Discovery MR 750, GE Healthcare, Waukesha, WI) using a 32-channel head RF coil. Spatial resolution = 1.0 mm × 1.0 mm × 1.0 mm, matrix size=256x256x256, TR = 4.6ms, TE = 1.7ms, nominal flip angle α_n=4° for the first 326 and α_n=6° for the remaining 112 views. Data were processed using an in-house retrospective motion correction pipeline and T1-weighted and quantitative T1 maps were generated (Kecskemeti et al., 2018). T1-weighted images were used for spatial normalization, cortical parcellation, and cortical surface inflation using the FreeSurfer image analysis pipeline and the Desikan et al. atlas labels (Collins et al., 1994; Dale et al., 1999; Desikan et al., 2006; Fischl, 2012; Fischl & Dale,

2000; Fischl, Sereno, & Dale, 1999; Fischl, Sereno, Tootell, et al., 1999). These transformations were then applied to the quantitative T1 maps and R1 values were calculated on the cortical midpoint. Means for several ROIs (n=10) were calculated, and paired t-tests were conducted to compare time 1 to time 3 differences. p-values were corrected for multiple comparisons by multiplying by the number of ROIs.

6.5.3. Results

Table 3 shows significant results in the NFS cohort, particularly bilateral increases in R1 in the inferior and superior parietal cortices and the right paracentral lobule. Note that a decrease in R1 was observed in the right parahippocampus. Though GH and control subjects were analyzed, no results survived multiple comparisons correction.

R1 Time 1 to Time 3			
Region	p-value	p-value*	T3-T1 mean R1 (s^{-1})
Entorhinal L	0.660	1	0.007+/- 0.071
Entorhinal R	0.404	1	0.016+/- 0.085
Inferior Parietal L	0.006	0.048	0.006 +/- 0.009
Inferior Parietal R	0.007	0.056	0.009 +/- 0.013
Parahippocampal L	0.159	1	-0.007 +/- 0.022
Parahippocampal R	0.008	0.064	-0.016 +/- 0.024
Paracentral L	0.161	1	0.003 +/- 0.011
Paracentral R	0.009	0.072	0.006 +/- 0.009
Superior Parietal L	0.006	0.060	0.007 +/- 0.010
Superior Parietal R	0.002	0.016	0.010 +/- 0.012

Table 3: Regional differences in mean R1 values from time 1 to time 3 in the NFS group. *corrected for multiple comparisons

6.5.4. Discussion

For participants that played the Need for Speed game, we observed significantly increased cortical R1 in the left and right inferior and superior parietal lobe, as well as the right paracentral lobule; these regions form the basis for understanding sensory and somatosensory association, as well as coordinating the control of the lower limbs (which were used to operate the gas and brake pedals in the NFS cohort)(Adair & Meador, 2003). Further, we observed evidence of a

neuroplastic response in the right parahippocampal gyrus, which is involved in memory, particularly the spatial location of objects (Bohbot et al., 2015). These changes may represent cortical myelination or other microstructural changes. Though we did not observe any significant changes in the GH cohort, we attribute the lack of findings to the difficulty of measuring the small changes induced by just a few weeks of training and the need for larger sample sizes.

7. Conclusions and Future Work

This work has outlined three chapters of original work that have expanded the neuroimaging and neuroscientific understanding of the evolution and decline of white matter. Particularly, this work has explored the impact of Aβ on white matter and its effect on episodic memory in the high AD-risk Down syndrome community. Further, this work has explored the utility of videogame training to evoke neuroplastic processes observable with MRI in both the short- and long-term.

The body of AD literature in DS is so small that nearly any finding constitutes a significant contribution to the field. This work is the largest DS MRI study to date. While this is an accomplishment in and of itself, it is important to note that this work does not merely confirm previous findings in a larger cohort – it significantly expands them. This work has increased the understanding of WM microstructure in aging DS and its relation to Aβ and cognitive ability. In this way, these findings serve as a bridge between the MRI, PET, and cognitive DS literature, which have been largely disjoint or limited by sample size in prior literature.

As the interest in imaging biomarkers of AD continues to grow rapidly, it is important to characterize how these measures correlate with anatomical changes *in-vivo*. The DS community has a near certain chance of developing AD in their lifetimes, likely attributable to the increased production of APP due to trisomy-21, which makes this population one of the best for pre-symptomatic study of MCI and AD. To this end, this work has shown a significant correlation between global Aβ measured using amyloid-load and white matter microstructure decline. Further, this association was found to accelerate with increasing age, as shown by a significant ABL*age interaction with MD and FA. These associations were observed throughout the association fibers and paint a troubling picture for the stability of inter and intralobular

connections with increasing Aβ, as might be expected. Further, it was observed that WM microstructure has a significant effect on episodic memory performance across the entire EM cognitive domain. It is plausible that the Aβ-mediated microstructural differences may play a role in the earliest cognitive deficits (episodic memory) observed in AD in the DS population.

Even the most well-designed imaging studies of DS have their challenges and limitations. Gross anatomical differences between the DS and typically developing brain, such as ventriculomegaly, brachycephaly, and hypoplasia, as well as a lack of DS-specific brain atlas can lead to misregistration when aligning to a standard space. Though the use of a population derived FA template may mitigate some of these misregistration effects and was employed here, the definition of a DS-specific template and atlas is one of the most pressing needs of continued work in the study of DS with MRI. Further, motion is a significant confound in DS imaging, particularly with diffusion methods, as motion can significantly affect findings. For example, in this work, over thirty subjects were removed from analyses due to significant motion artifacts. While inter-volume (and intra-volume to an extent) motion can be corrected, faster and more efficient scans with a greater number of volumes will be required to ensure data integrity and minimize the risk of subject censure due to artifacts. Longitudinal tracking of subjects is also necessary to track microstructural changes within subjects to develop disease trajectories for WM changes, as well as to characterize how microstructure relates to EM over time.

Lastly, this work has shown the utility of targeted videogame training to evoke microstructural and structural changes in task-related areas that may be detectable by MRI. These changes are likely attributable to neuroplastic processes; however, it would be an overstatement of the power of current MRI methods to declaratively ascribe these findings solely to neuroplastic responses. A unique contribution of the above work is it is the first study to

examine multiple videogames, with the tasks tailored to recruit neuroplastic processes in task-specific areas, i.e., spatial route learning and motor planning areas. It was shown that GH training was able to cause short and long-term changes in motor planning areas (M1, PM, and IC), while NFS showed both diffusion and R1-structural changes in the hippocampus and visual areas. This work also was able to reproduce the short-term hippocampal findings of earlier works by Sagi et al. (2012) and Keller and Just (2016).

The study of neuroplasticity *in-vivo* is particularly challenging. While recent studies, as well as this work, have shown that it is possible to detect structural and microstructural changes most likely attributable to synaptic plasticity, it is not without difficulty. While brain plasticity does decrease with age, the notion of a rigid brain in adulthood has largely been debased; however, the brain is not as plastic in adulthood as for a newborn. This may be by design, as an adult brain is quite complex (having shed much of its simpler connections in adolescence) and may already have connections within the brain that are useful for a new task. This leads to small effect sizes that can be challenging to resolve for small samples, as the sample size analysis in Chapter 6 illustrates.

References

Abdel Razek, A. A., Abd El-Gaber, N., Abdalla, A., Fathy, A., Azab, A., & Rahman, A. A. (2009, Nov). Apparent diffusion coefficient vale of the brain in patients with Gaucher's disease type II and type III. *Neuroradiology, 51*(11), 773-779. https://doi.org/10.1007/s00234-009-0548-1

Abe, O., Aoki, S., Hayashi, N., Yamada, H., Kunimatsu, A., Mori, H., Yoshikawa, T., Okubo, T., & Ohtomo, K. (2002, 2002/05/01/). Normal aging in the central nervous system: quantitative MR diffusion-tensor analysis. *Neurobiology of Aging, 23*(3), 433-441. https://doi.org/https://doi.org/10.1016/S0197-4580(01)00318-9

Abraham, W. C., Jones, O. D., & Glanzman, D. L. (2019, 2019/07/02). Is plasticity of synapses the mechanism of long-term memory storage? *npj Science of Learning, 4*(1), 9. https://doi.org/10.1038/s41539-019-0048-y

Acosta-Cabronero, J., & Nestor, P. J. (2014). Diffusion tensor imaging in Alzheimer's disease: insights into the limbic-diencephalic network and methodological considerations. *Front Aging Neurosci, 6*, 266. https://doi.org/10.3389/fnagi.2014.00266

Adair, J. C., & Meador, K. J. (2003). Parietal Lobe. In M. J. Aminoff & R. B. Daroff (Eds.), *Encyclopedia of the Neurological Sciences* (pp. 805-815). Academic Press. https://doi.org/https://doi.org/10.1016/B0-12-226870-9/01684-1

Akoudad, S., de Groot, M., Koudstaal, P. J., van der Lugt, A., Niessen, W. J., Hofman, A., Ikram, M. A., & Vernooij, M. W. (2013, Nov 26). Cerebral microbleeds are related to loss of white matter structural integrity. *Neurology, 81*(22), 1930-1937. https://doi.org/10.1212/01.wnl.0000436609.20587.65

Aldrich, F. K., & Wilson, B. (1991). Rivermead Behavioural Memory Test for Children (RBMT-C): A preliminary evaluation. *British Journal of Clinical Psychology, 30*(2), 161-168. https://doi.org/10.1111/j.2044-8260.1991.tb00931.x

Alexander, A. L., Hurley, S. A., Samsonov, A. A., Adluru, N., Hosseinbor, A. P., Mossahebi, P., Tromp, D. P. M., Zakszewski, E., & Field, A. S. (2011, 2011/12/01). Characterization of Cerebral White Matter Properties Using Quantitative Magnetic Resonance Imaging Stains. *Brain Connectivity, 1*(6), 423-446. https://doi.org/10.1089/brain.2011.0071

Alexander, A. L., Lee, J. E., Lazar, M., & Field, A. S. (2007, Jul). Diffusion tensor imaging of the brain. *Neurotherapeutics, 4*(3), 316-329. https://doi.org/10.1016/j.nurt.2007.05.011

Alves, G. S., Oertel Knöchel, V., Knöchel, C., Carvalho, A. F., Pantel, J., Engelhardt, E., & Laks, J. (2015, 2015/01/20). Integrating Retrogenesis Theory to Alzheimer's Disease Pathology: Insight from DTI-TBSS Investigation of the White Matter Microstructural Integrity. *BioMed Research International, 2015*, 291658. https://doi.org/10.1155/2015/291658

Andersson, J. L. R., Graham, M. S., Zsoldos, E., & Sotiropoulos, S. N. (2016, Nov 1). Incorporating outlier detection and replacement into a non-parametric framework for movement and distortion correction of diffusion MR images. *Neuroimage*, *141*, 556-572. https://doi.org/10.1016/j.neuroimage.2016.06.058

Andersson, J. L. R., & Sotiropoulos, S. N. (2016, Jan 15). An integrated approach to correction for off-resonance effects and subject movement in diffusion MR imaging. *Neuroimage*, *125*, 1063-1078. https://doi.org/10.1016/j.neuroimage.2015.10.019

Annus, T., Wilson, L. R., Acosta-Cabronero, J., Cardenas-Blanco, A., Hong, Y. T., Fryer, T. D., Coles, J. P., Menon, D. K., Zaman, S. H., Holland, A. J., & Nestor, P. J. (2017). The Down syndrome brain in the presence and absence of fibrillar β-amyloidosis. *Neurobiology of Aging*, *53*, 11-19. https://doi.org/10.1016/j.neurobiolaging.2017.01.009

Annus, T., Wilson, L. R., Hong, Y. T., Acosta-Cabronero, J., Fryer, T. D., Cardenas-Blanco, A., Smith, R., Boros, I., Coles, J. P., Aigbirhio, F. I., Menon, D. K., Zaman, S. H., Nestor, P. J., & Holland, A. J. (2016, May). The pattern of amyloid accumulation in the brains of adults with Down syndrome. *Alzheimers Dement*, *12*(5), 538-545. https://doi.org/10.1016/j.jalz.2015.07.490

Antonarakis, S. E., Skotko, B. G., Rafii, M. S., Strydom, A., Pape, S. E., Bianchi, D. W., Sherman, S. L., & Reeves, R. H. (2020, 2020/02/06). Down syndrome. *Nature Reviews Disease Primers*, *6*(1), 9. https://doi.org/10.1038/s41572-019-0143-7

Araque Caballero, M., Brendel, M., Delker, A., Ren, J., Rominger, A., Bartenstein, P., Dichgans, M., Weiner, M. W., & Ewers, M. (2015, Nov). Mapping 3-year changes in gray matter and metabolism in Aβ-positive nondemented subjects. *Neurobiol Aging*, *36*(11), 2913-2924. https://doi.org/10.1016/j.neurobiolaging.2015.08.007

Assaf, Y., & Basser, P. J. (2005, Aug 1). Composite hindered and restricted model of diffusion (CHARMED) MR imaging of the human brain. *Neuroimage*, *27*(1), 48-58. https://doi.org/10.1016/j.neuroimage.2005.03.042

Avants, B. B., Tustison, N. J., Song, G., Cook, P. A., Klein, A., & Gee, J. C. (2011, Feb 1). A reproducible evaluation of ANTs similarity metric performance in brain image registration. *Neuroimage*, *54*(3), 2033-2044. https://doi.org/10.1016/j.neuroimage.2010.09.025

Bachiller, S., Jiménez-Ferrer, I., Paulus, A., Yang, Y., Swanberg, M., Deierborg, T., & Boza-Serrano, A. (2018, 2018-December-18). Microglia in Neurological Diseases: A Road Map to Brain-Disease Dependent-Inflammatory Response [Review]. *Frontiers in Cellular Neuroscience*, *12*(488). https://doi.org/10.3389/fncel.2018.00488

Ballard, C., Gauthier, S., Corbett, A., Brayne, C., Aarsland, D., & Jones, E. (2011, Mar 19). Alzheimer's disease. *Lancet*, *377*(9770), 1019-1031. https://doi.org/10.1016/s0140-6736(10)61349-9

Barage, S. H., & Sonawane, K. D. (2015, 2015/08/01/). Amyloid cascade hypothesis: Pathogenesis and therapeutic strategies in Alzheimer's disease. *Neuropeptides, 52*, 1-18. https://doi.org/https://doi.org/10.1016/j.npep.2015.06.008

Basser, P. J., Mattiello, J., & Lebihan, D. (1994a, 1994/03/01/). Estimation of the Effective Self-Diffusion Tensor from the NMR Spin Echo. *Journal of Magnetic Resonance, Series B, 103*(3), 247-254. https://doi.org/https://doi.org/10.1006/jmrb.1994.1037

Basser, P. J., Mattiello, J., & LeBihan, D. (1994b, Jan). MR diffusion tensor spectroscopy and imaging. *Biophys J, 66*(1), 259-267. https://doi.org/10.1016/S0006-3495(94)80775-1

Basser, P. J., & Pierpaoli, C. (1996, Jun). Microstructural and physiological features of tissues elucidated by quantitative-diffusion-tensor MRI. *J Magn Reson B, 111*(3), 209-219. https://doi.org/10.1006/jmrb.1996.0086

Bastiani, M., Cottaar, M., Fitzgibbon, S. P., Suri, S., Alfaro-Almagro, F., Sotiropoulos, S. N., Jbabdi, S., & Andersson, J. L. R. (2019, 2019/01/01/). Automated quality control for within and between studies diffusion MRI data using a non-parametric framework for movement and distortion correction. *Neuroimage, 184*, 801-812. https://doi.org/https://doi.org/10.1016/j.neuroimage.2018.09.073

Bateman, R. J., Aisen, P. S., De Strooper, B., Fox, N. C., Lemere, C. A., Ringman, J. M., Salloway, S., Sperling, R. A., Windisch, M., & Xiong, C. (2011, 2011/01/06). Autosomal-dominant Alzheimer's disease: a review and proposal for the prevention of Alzheimer's disease. *Alzheimer's Research & Therapy, 3*(1), 1. https://doi.org/10.1186/alzrt59

Bazydlo, A., Zammit, M., Wu, M., Dean, D., Johnson, S., Tudorascu, D., Cohen, A., Cody, K., Ances, B., Laymon, C., Klunk, W., Zaman, S., Handen, B., Alexander, A., Christian, B., & Hartley, S. (2021, 2021/04/20). White matter microstructure associations with episodic memory in adults with Down syndrome: a tract-based spatial statistics study. *Journal of Neurodevelopmental Disorders, 13*(1), 17. https://doi.org/10.1186/s11689-021-09366-1

Beach, T. G., Walker, R., & McGeer, E. G. (1989). Patterns of gliosis in alzheimer's disease and aging cerebrum. *Glia, 2*(6), 420-436. https://doi.org/https://doi.org/10.1002/glia.440020605

Beckett, L. A., Donohue, M. C., Wang, C., Aisen, P., Harvey, D. J., & Saito, N. (2015, Jul). The Alzheimer's Disease Neuroimaging Initiative phase 2: Increasing the length, breadth, and depth of our understanding. *Alzheimers Dement, 11*(7), 823-831. https://doi.org/10.1016/j.jalz.2015.05.004

Beery, K. E. (2004). Beery VMI: The Beery-Buktenica developmental test of visual-motor integration. *Minneapolis, MN: Pearson*.

Bekris, L. M., Yu, C.-E., Bird, T. D., & Tsuang, D. W. (2010). Genetics of Alzheimer disease. *Journal of geriatric psychiatry and neurology*, *23*(4), 213-227. https://doi.org/10.1177/0891988710383571

Bendlin, B. B., Carlsson, C. M., Johnson, S. C., Zetterberg, H., Blennow, K., Willette, A. A., Okonkwo, O. C., Sodhi, A., Ries, M. L., Birdsill, A. C., Alexander, A. L., Rowley, H. A., Puglielli, L., Asthana, S., & Sager, M. A. (2012). CSF T-Tau/Abeta42 predicts white matter microstructure in healthy adults at risk for Alzheimer's disease. *PLoS One*, *7*(6), e37720. https://doi.org/10.1371/journal.pone.0037720

Bengtsson, S. L., Nagy, Z., Skare, S., Forsman, L., Forssberg, H., & Ullén, F. (2005, 2005/09/01). Extensive piano practicing has regionally specific effects on white matter development. *Nature neuroscience*, *8*(9), 1148-1150. https://doi.org/10.1038/nn1516

Bennett, I. J., Madden, D. J., Vaidya, C. J., Howard, D. V., & Howard, J. H., Jr. (2010). Age-related differences in multiple measures of white matter integrity: A diffusion tensor imaging study of healthy aging. *Human brain mapping*, *31*(3), 378-390. https://doi.org/10.1002/hbm.20872

Bloch, F. (1946, 10/01/). Nuclear Induction. *Physical Review*, *70*(7-8), 460-474. https://doi.org/10.1103/PhysRev.70.460

Bohbot, V. D., Allen, J. J. B., Dagher, A., Dumoulin, S. O., Evans, A. C., Petrides, M., Kalina, M., Stepankova, K., & Nadel, L. (2015, 2015-August-03). Role of the parahippocampal cortex in memory for the configuration but not the identity of objects: converging evidence from patients with selective thermal lesions and fMRI [Original Research]. *Frontiers in Human Neuroscience*, *9*(431). https://doi.org/10.3389/fnhum.2015.00431

Braak, H., Alafuzoff, I., Arzberger, T., Kretzschmar, H., & Del Tredici, K. (2006). Staging of Alzheimer disease-associated neurofibrillary pathology using paraffin sections and immunocytochemistry. *Acta neuropathologica*, *112*(4), 389-404. https://doi.org/10.1007/s00401-006-0127-z

Braak, H., & Braak, E. (1991). Neuropathological stageing of Alzheimer-related changes. *Acta Neuropathol*, *82*(4), 239-259. https://doi.org/10.1007/bf00308809

Bradl, M., & Lassmann, H. (2010). Oligodendrocytes: biology and pathology. *Acta neuropathologica*, *119*(1), 37-53. https://doi.org/10.1007/s00401-009-0601-5

Brooks, B. L., Sherman, E. M. S., & Strauss, E. (2009, 2009/12/21). NEPSY-II: A Developmental Neuropsychological Assessment, Second Edition. *Child Neuropsychology*, *16*(1), 80-101. https://doi.org/10.1080/09297040903146966

Brown, R. (1828, 1828/09/01). XXVII. A brief account of microscopical observations made in the months of June, July and August 1827, on the particles contained in the pollen of plants;

and on the general existence of active molecules in organic and inorganic bodies. *The Philosophical Magazine*, *4*(21), 161-173. https://doi.org/10.1080/14786442808674769

Bubb, E. J., Metzler-Baddeley, C., & Aggleton, J. P. (2018, 2018/09/01/). The cingulum bundle: Anatomy, function, and dysfunction. *Neuroscience & Biobehavioral Reviews, 92*, 104-127. https://doi.org/https://doi.org/10.1016/j.neubiorev.2018.05.008

Buschke, H. (1984, 1984/11/01). Cued recall in Amnesia. *Journal of Clinical Neuropsychology, 6*(4), 433-440. https://doi.org/10.1080/01688638408401233

Caballero, M. Á. A., Song, Z., Rubinski, A., Duering, M., Dichgans, M., Park, D. C., & Ewers, M. (2020). Age-dependent amyloid deposition is associated with white matter alterations in cognitively normal adults during the adult life span. *Alzheimer's & Dementia, 16*(4), 651-661. https://doi.org/10.1002/alz.12062

Campbell, S., Switzer, R., & Martin, T. (1987). Alzheimer's plaques and tangles: a controlled and enhanced silver staining method. Soc Neurosci Abstr,

Carr, H. Y., & Purcell, E. M. (1954, 05/01/). Effects of Diffusion on Free Precession in Nuclear Magnetic Resonance Experiments. *Physical Review, 94*(3), 630-638. https://doi.org/10.1103/PhysRev.94.630

Catani, M., & Thiebaut de Schotten, M. (2012). *Atlas of human brain connections*. Oxford University Press.

Cerciello, M., Isella, V., Proserpi, A., & Papagno, C. (2017, Jan). Assessment of free and cued recall in Alzheimer's disease and vascular and frontotemporal dementia with 24-item Grober and Buschke test. *Neurol Sci, 38*(1), 115-122. https://doi.org/10.1007/s10072-016-2722-7

Chang, L.-C., Walker, L., & Pierpaoli, C. (2012). Informed RESTORE: A method for robust estimation of diffusion tensor from low redundancy datasets in the presence of physiological noise artifacts. *Magnetic resonance in medicine, 68*(5), 1654-1663. https://doi.org/10.1002/mrm.24173

Chang, L. C., Jones, D. K., & Pierpaoli, C. (2005, May). RESTORE: robust estimation of tensors by outlier rejection. *Magn Reson Med, 53*(5), 1088-1095. https://doi.org/10.1002/mrm.20426

Chang, L. C., Walker, L., & Pierpaoli, C. (2012, Nov). Informed RESTORE: A method for robust estimation of diffusion tensor from low redundancy datasets in the presence of physiological noise artifacts. *Magn Reson Med, 68*(5), 1654-1663. https://doi.org/10.1002/mrm.24173

Chao, L. L., DeCarli, C., Kriger, S., Truran, D., Zhang, Y., Laxamana, J., Villeneuve, S., Jagust, W. J., Sanossian, N., Mack, W. J., Chui, H. C., & Weiner, M. W. (2013). Associations

between White Matter Hyperintensities and β Amyloid on Integrity of Projection, Association, and Limbic Fiber Tracts Measured with Diffusion Tensor MRI. *PLOS ONE, 8*(6), e65175. https://doi.org/10.1371/journal.pone.0065175

Chechik, G., Meilijson, I., & Ruppin, E. (1999). Neuronal Regulation: A Mechanism for Synaptic Pruning During Brain Maturation. *Neural Computation, 11*(8), 2061-2080. https://doi.org/10.1162/089976699300016089

Chen, S. Q., Kang, Z., Hu, X. Q., Hu, B., & Zou, Y. (2007, Apr). Diffusion tensor imaging of the brain in patients with Alzheimer's disease and cerebrovascular lesions. *J Zhejiang Univ Sci B, 8*(4), 242-247. https://doi.org/10.1631/jzus.2007.B0242

Chien, D. T., Bahri, S., Szardenings, A. K., Walsh, J. C., Mu, F., Su, M. Y., Shankle, W. R., Elizarov, A., & Kolb, H. C. (2013). Early clinical PET imaging results with the novel PHF-tau radioligand [F-18]-T807. *J Alzheimers Dis, 34*(2), 457-468. https://doi.org/10.3233/jad-122059

Chow, V. W., Mattson, M. P., Wong, P. C., & Gleichmann, M. (2010, Mar). An overview of APP processing enzymes and products. *Neuromolecular Med, 12*(1), 1-12. https://doi.org/10.1007/s12017-009-8104-z

Cole, J. H., Annus, T., Wilson, L. R., Remtulla, R., Hong, Y. T., Fryer, T. D., Acosta-Cabronero, J., Cardenas-Blanco, A., Smith, R., Menon, D. K., Zaman, S. H., Nestor, P. J., & Holland, A. J. (2017, Aug). Brain-predicted age in Down syndrome is associated with beta amyloid deposition and cognitive decline. *Neurobiol Aging, 56*, 41-49. https://doi.org/10.1016/j.neurobiolaging.2017.04.006

Collins, D. L., Neelin, P., Peters, T. M., & Evans, A. C. (1994, Mar-Apr). Automatic 3D intersubject registration of MR volumetric data in standardized Talairach space. *J Comput Assist Tomogr, 18*(2), 192-205.

Cordero-Grande, L., Christiaens, D., Hutter, J., Price, A. N., & Hajnal, J. V. (2019, 2019/10/15/). Complex diffusion-weighted image estimation via matrix recovery under general noise models. *Neuroimage, 200*, 391-404. https://doi.org/https://doi.org/10.1016/j.neuroimage.2019.06.039

Dale, A. M., Fischl, B., & Sereno, M. I. (1999, Feb). Cortical surface-based analysis. I. Segmentation and surface reconstruction. *Neuroimage, 9*(2), 179-194. https://doi.org/10.1006/nimg.1998.0395

De Simone, T., Regna-Gladin, C., Carriero, M. R., Farina, L., & Savoiardo, M. (2005). Wallerian Degeneration of the Pontocerebellar Fibers. *American Journal of Neuroradiology, 26*(5), 1062-1065. http://www.ajnr.org/content/ajnr/26/5/1062.full.pdf

Desikan, R. S., Ségonne, F., Fischl, B., Quinn, B. T., Dickerson, B. C., Blacker, D., Buckner, R. L., Dale, A. M., Maguire, R. P., Hyman, B. T., Albert, M. S., & Killiany, R. J. (2006, Jul

1). An automated labeling system for subdividing the human cerebral cortex on MRI scans into gyral based regions of interest. *Neuroimage, 31*(3), 968-980. https://doi.org/10.1016/j.neuroimage.2006.01.021

Diciotti, S., Ginestroni, A., Bessi, V., Giannelli, M., Tessa, C., Bracco, L., Mascalchi, M., & Toschi, N. (2012, 28 Aug.-1 Sept. 2012). Identification of Mild Alzheimer's Disease through automated classification of structural MRI features. 2012 Annual International Conference of the IEEE Engineering in Medicine and Biology Society,

Dona, O., Thompson, J., & Druchok, C. (2016). Comprehensive Review on Magnetic Resonance Imaging in Alzheimer's Disease. *Crit Rev Biomed Eng, 44*(3), 213-225. https://doi.org/10.1615/CritRevBiomedEng.2016019544

Down Syndrome: Condition Information. (2012). NIH. https://www.nichd.nih.gov/health/topics/down/conditioninfo

Driemeyer, J., Boyke, J., Gaser, C., Büchel, C., & May, A. (2008, Jul 23). Changes in gray matter induced by learning--revisited. *PLOS ONE, 3*(7), e2669. https://doi.org/10.1371/journal.pone.0002669

Dunn, L. M. (2007). *PPVT-4 : Peabody picture vocabulary test* (4th ed. ed.). Pearson Assessments.

Edgar, J. M., & Griffiths, I. R. (2014). Chapter 7 - White Matter Structure: A Microscopist's View. In H. Johansen-Berg & T. E. J. Behrens (Eds.), *Diffusion MRI (Second Edition)* (pp. 127-153). Academic Press. https://doi.org/https://doi.org/10.1016/B978-0-12-396460-1.00007-X

Einstein, A. (1905). Über die von der molekularkinetischen Theorie der Wärme geforderte Bewegung von in ruhenden Flüssigkeiten suspendierten Teilchen. *Annalen der Physik, 322*(8), 549-560. https://doi.org/https://doi.org/10.1002/andp.19053220806

Einstein, A., F¸rth, R., Cowper, A. D., & Dover, P. (2006). *Investigations on the theory of the Brownian movement*. Dover Publications, Inc.

Emos, M. A., S. (2020). *Neuroanatomy, Internal Capsule*. StatPearls Publishing.

Evenhuis, H. M. (2018). The Dementia Questionnaire for People with Learning Disabilities. In V. P. Prasher (Ed.), *Neuropsychological Assessments of Dementia in Down Syndrome and Intellectual Disabilities* (pp. 43-56). Springer International Publishing. https://doi.org/10.1007/978-3-319-61720-6_3

Fenoll, R., Pujol, J., Esteba-Castillo, S., de Sola, S., Ribas-Vidal, N., Garcia-Alba, J., Sanchez-Benavides, G., Martinez-Vilavella, G., Deus, J., Dierssen, M., Novell-Alsina, R., & de la Torre, R. (2017). Anomalous White Matter Structure and the Effect of Age in Down Syndrome Patients. *J Alzheimers Dis, 57*(1), 61-70. https://doi.org/10.3233/jad-161112

Ferencz, B., & Gerritsen, L. (2015, 2015/03/01). Genetics and Underlying Pathology of Dementia. *Neuropsychology Review*, *25*(1), 113-124. https://doi.org/10.1007/s11065-014-9276-3

Ferris, S. H., de Leon, M. J., Wolf, A. P., Farkas, T., Christman, D. R., Reisberg, B., Fowler, J. S., MacGregor, R., Goldman, A., George, A. E., & Rampal, S. (1980, 1980/12/01/). Positron Emission Tomography in the Study of Aging and Senile Dementia. *Neurobiology of Aging*, *1*(2), 127-131. https://doi.org/https://doi.org/10.1016/0197-4580(80)90005-6

Fick, R. H. J., Wassermann, D., & Deriche, R. (2019, 2019-October-15). The Dmipy Toolbox: Diffusion MRI Multi-Compartment Modeling and Microstructure Recovery Made Easy [Original Research]. *Frontiers in Neuroinformatics*, *13*(64). https://doi.org/10.3389/fninf.2019.00064

Fields, R. D. (2011, 2011/04/01). Imaging Learning: The Search for a Memory Trace. *The Neuroscientist*, *17*(2), 185-196. https://doi.org/10.1177/1073858410383696

Fields, R. D., Araque, A., Johansen-Berg, H., Lim, S.-S., Lynch, G., Nave, K.-A., Nedergaard, M., Perez, R., Sejnowski, T., & Wake, H. (2013, 2014/10/01). Glial Biology in Learning and Cognition. *The Neuroscientist*, *20*(5), 426-431. https://doi.org/10.1177/1073858413504465

Fischl, B. (2012, Aug 15). FreeSurfer. *Neuroimage*, *62*(2), 774-781. https://doi.org/10.1016/j.neuroimage.2012.01.021

Fischl, B., & Dale, A. M. (2000, Sep 26). Measuring the thickness of the human cerebral cortex from magnetic resonance images. *Proc Natl Acad Sci U S A*, *97*(20), 11050-11055. https://doi.org/10.1073/pnas.200033797

Fischl, B., Sereno, M. I., & Dale, A. M. (1999, Feb). Cortical surface-based analysis. II: Inflation, flattening, and a surface-based coordinate system. *Neuroimage*, *9*(2), 195-207. https://doi.org/10.1006/nimg.1998.0396

Fischl, B., Sereno, M. I., Tootell, R. B., & Dale, A. M. (1999). High-resolution intersubject averaging and a coordinate system for the cortical surface. *Hum Brain Mapp*, *8*(4), 272-284. https://doi.org/10.1002/(sici)1097-0193(1999)8:4<272::aid-hbm10>3.0.co;2-4

Fox, N. C., Crum, W. R., Scahill, R. I., Stevens, J. M., Janssen, J. C., & Rossor, M. N. (2001, Jul 21). Imaging of onset and progression of Alzheimer's disease with voxel-compression mapping of serial magnetic resonance images. *Lancet*, *358*(9277), 201-205. https://doi.org/10.1016/s0140-6736(01)05408-3

Fox, N. C., Warrington, E. K., Freeborough, P. A., Hartikainen, P., Kennedy, A. M., Stevens, J. M., & Rossor, M. N. (1996, Dec). Presymptomatic hippocampal atrophy in Alzheimer's disease. A longitudinal MRI study. *Brain*, *119 (Pt 6)*, 2001-2007. https://doi.org/10.1093/brain/119.6.2001

Fox, N. C., Warrington, E. K., & Rossor, M. N. (1999, Jun 19). Serial magnetic resonance imaging of cerebral atrophy in preclinical Alzheimer's disease. *Lancet, 353*(9170), 2125. https://doi.org/10.1016/s0140-6736(99)00496-1

Gallagher, T. A., Alexander, A. L., & Field, A. S. (2012). Diffusion Tensor Magnetic Resonance Imaging: Physical Principles. In S. H. Faro, F. B. Mohamed, M. Law, & J. T. Ulmer (Eds.), *Functional Neuroradiology: Principles and Clinical Applications* (pp. 709-729). Springer US. https://doi.org/10.1007/978-1-4419-0345-7_35

Gärtner, H., Minnerop, M., Pieperhoff, P., Schleicher, A., Zilles, K., Altenmüller, E., & Amunts, K. (2013, 09/23). Brain morphometry shows effects of long-term musical practice in middle-aged keyboard players. *Frontiers in psychology, 4*, 636. https://doi.org/10.3389/fpsyg.2013.00636

Garyfallidis, E., Brett, M., Amirbekian, B., Rokem, A., van der Walt, S., Descoteaux, M., & Nimmo-Smith, I. (2014). Dipy, a library for the analysis of diffusion MRI data. *Front Neuroinform, 8*, 8. https://doi.org/10.3389/fninf.2014.00008

Garyfallidis, E., Brett, M., Amirbekian, B., Rokem, A., van der Walt, S., Descoteaux, M., Nimmo-Smith, I., & Dipy, C. (2014). Dipy, a library for the analysis of diffusion MRI data. *Front Neuroinform, 8*, 8. https://doi.org/10.3389/fninf.2014.00008

Garza-Villarreal, E., Jiang, Z., Vuust, P., Alcauter, S., Vase, L., Pasaye, E., Cavazos-Rodriguez, R., Brattico, E., Jensen, T., & Barrios, F. (2015, 2015-July-22). Music reduces pain and increases resting state fMRI BOLD signal amplitude in the left angular gyrus in fibromyalgia patients [Original Research]. *Frontiers in psychology, 6*(1051). https://doi.org/10.3389/fpsyg.2015.01051

Gauthier, S., Reisberg, B., Zaudig, M., Petersen, R. C., Ritchie, K., Broich, K., Belleville, S., Brodaty, H., Bennett, D., Chertkow, H., Cummings, J. L., de Leon, M., Feldman, H., Ganguli, M., Hampel, H., Scheltens, P., Tierney, M. C., Whitehouse, P., & Winblad, B. (2006, 2006/04/15/). Mild cognitive impairment. *The Lancet, 367*(9518), 1262-1270. https://doi.org/https://doi.org/10.1016/S0140-6736(06)68542-5

George, K., & J, M. D. (2021). Neuroanatomy, Thalamocortical Radiations. In *StatPearls*. StatPearls Publishing
Copyright © 2021, StatPearls Publishing LLC.

Graham, M. S., Drobnjak, I., & Zhang, H. (2016, 2016/01/15/). Realistic simulation of artefacts in diffusion MRI for validating post-processing correction techniques. *Neuroimage, 125*, 1079-1094. https://doi.org/https://doi.org/10.1016/j.neuroimage.2015.11.006

[Record #65 is using a reference type undefined in this output style.]

Gupta, D. (2017). Chapter 1 - Neuroanatomy. In H. Prabhakar (Ed.), *Essentials of Neuroanesthesia* (pp. 3-40). Academic Press. https://doi.org/https://doi.org/10.1016/B978-0-12-805299-0.00001-4

Haass, C., & Selkoe, D. J. (2007). Soluble protein oligomers in neurodegeneration: lessons from the Alzheimer's amyloid β-peptide. *Nature reviews Molecular cell biology*, *8*(2), 101-112.

Hahn, E. L. (1950, 11/15/). Spin Echoes. *Physical Review*, *80*(4), 580-594. https://doi.org/10.1103/PhysRev.80.580

Han, Y., Yang, H., Lv, Y.-T., Zhu, C.-Z., He, Y., Tang, H.-H., Gong, Q.-Y., Luo, Y.-J., Zang, Y.-F., & Dong, Q. (2009, 2009/07/31/). Gray matter density and white matter integrity in pianists' brain: A combined structural and diffusion tensor MRI study. *Neuroscience letters*, *459*(1), 3-6. https://doi.org/https://doi.org/10.1016/j.neulet.2008.07.056

Handen, B. L., Cohen, A. D., Channamalappa, U., Bulova, P., Cannon, S. A., Cohen, W. I., Mathis, C. A., Price, J. C., & Klunk, W. E. (2012). Imaging brain amyloid in nondemented young adults with Down syndrome using Pittsburgh compound B. *Alzheimer's & Dementia*, *8*(6), 496-501. https://doi.org/https://doi.org/10.1016/j.jalz.2011.09.229

Hardy, J. A., & Higgins, G. A. (1992, Apr 10). Alzheimer's disease: the amyloid cascade hypothesis. *Science*, *256*(5054), 184-185. https://doi.org/10.1126/science.1566067

Hartley, S. L., Handen, B. L., Devenny, D., Mihaila, I., Hardison, R., Lao, P. J., Klunk, W. E., Bulova, P., Johnson, S. C., & Christian, B. T. (2017). Cognitive decline and brain amyloid-β accumulation across 3 years in adults with Down syndrome. *Neurobiology of Aging*, *58*, 68-76. https://doi.org/10.1016/j.neurobiolaging.2017.05.019

Hartley, S. L., Handen, B. L., Devenny, D., Tudorascu, D., Piro-Gambetti, B., Zammit, M. D., Laymon, C. M., Klunk, W. E., Zaman, S., Cohen, A., & Christian, B. T. (2020). Cognitive indicators of transition to preclinical and prodromal stages of Alzheimer's disease in Down syndrome. *Alzheimer's & Dementia: Diagnosis, Assessment & Disease Monitoring*, *12*(1), e12096. https://doi.org/10.1002/dad2.12096

Hartley, S. L., Handen, B. L., Devenny, D. A., Hardison, R., Mihaila, I., Price, J. C., Cohen, A. D., Klunk, W. E., Mailick, M. R., Johnson, S. C., & Christian, B. T. (2014, Sep). Cognitive functioning in relation to brain amyloid-beta in healthy adults with Down syndrome. *Brain*, *137*(Pt 9), 2556-2563. https://doi.org/10.1093/brain/awu173

Hartley, S. L., Handen, B. L., Devenny, D. A., Hardison, R., Mihaila, I., Price, J. C., Cohen, A. D., Klunk, W. E., Mailick, M. R., Johnson, S. C., & Christian, B. T. (2014). Cognitive functioning in relation to brain amyloid-β in healthy adults with Down syndrome. *Brain : a journal of neurology*, *137*(Pt 9), 2556-2563. https://doi.org/10.1093/brain/awu173

Haxby, J. V. (1989, Jun). Neuropsychological evaluation of adults with Down's syndrome: patterns of selective impairment in non-demented old adults. *J Ment Defic Res, 33 (Pt 3)*, 193-210. https://doi.org/10.1111/j.1365-2788.1989.tb01467.x

Haxby, J. V. (1989). Neuropsychological evaluation of adults with Down's syndrome: patterns of selective impairment in non-demented old adults. *Journal of Intellectual Disability Research, 33*(3), 193-210.

Head, E., Phelan, M. J., Doran, E., Kim, R. C., Poon, W. W., Schmitt, F. A., & Lott, I. T. (2017, Dec 1). Cerebrovascular pathology in Down syndrome and Alzheimer disease. *Acta Neuropathol Commun, 5*(1), 93. https://doi.org/10.1186/s40478-017-0499-4

Helman, A. M., Siever, M., McCarty, K. L., Lott, I. T., Doran, E., Abner, E. L., Schmitt, F. A., & Head, E. (2019). Microbleeds and Cerebral Amyloid Angiopathy in the Brains of People with Down Syndrome with Alzheimer's Disease. *J Alzheimers Dis, 67*(1), 103-112. https://doi.org/10.3233/jad-180589

Herbet, G., Zemmoura, I., & Duffau, H. (2018, 2018-September-19). Functional Anatomy of the Inferior Longitudinal Fasciculus: From Historical Reports to Current Hypotheses [Review]. *Frontiers in Neuroanatomy, 12*(77). https://doi.org/10.3389/fnana.2018.00077

Hippius, H., & Neundörfer, G. (2003). The discovery of Alzheimer's disease. *Dialogues in clinical neuroscience, 5*(1), 101-108. https://doi.org/10.31887/DCNS.2003.5.1/hhippius

Hirai, T., Ohye, C., Nagaseki, Y., & Matsumura, M. (1989). Cytometric analysis of the thalamic ventralis intermedius nucleus in humans. *Journal of Neurophysiology, 61*(3), 478-487. https://doi.org/10.1152/jn.1989.61.3.478

Hofstetter, S., Tavor, I., Tzur Moryosef, S., & Assaf, Y. (2013, Jul 31). Short-term learning induces white matter plasticity in the fornix. *J Neurosci, 33*(31), 12844-12850. https://doi.org/10.1523/jneurosci.4520-12.2013

Hosoda, C., Tanaka, K., Nariai, T., Honda, M., & Hanakawa, T. (2013). Dynamic Neural Network Reorganization Associated with Second Language Vocabulary Acquisition: A Multimodal Imaging Study. *The Journal of Neuroscience, 33*(34), 13663-13672. https://doi.org/10.1523/jneurosci.0410-13.2013

Hsu, J. L., Leemans, A., Bai, C. H., Lee, C. H., Tsai, Y. F., Chiu, H. C., & Chen, W. H. (2008, Jan 15). Gender differences and age-related white matter changes of the human brain: a diffusion tensor imaging study. *Neuroimage, 39*(2), 566-577. https://doi.org/10.1016/j.neuroimage.2007.09.017

Hughes, C. P., Berg, L., Danziger, W., Coben, L. A., & Martin, R. L. (1982). A New Clinical Scale for the Staging of Dementia. *British Journal of Psychiatry, 140*(6), 566-572. https://doi.org/10.1192/bjp.140.6.566

Innes, S., Pariante, C. M., & Borsini, A. (2019, Apr). Microglial-driven changes in synaptic plasticity: A possible role in major depressive disorder. *Psychoneuroendocrinology, 102*, 236-247. https://doi.org/10.1016/j.psyneuen.2018.12.233

Itagaki, S., McGeer, P. L., Akiyama, H., Zhu, S., & Selkoe, D. (1989, 1989/10/01/). Relationship of microglia and astrocytes to amyloid deposits of Alzheimer disease. *Journal of Neuroimmunology, 24*(3), 173-182. https://doi.org/https://doi.org/10.1016/0165-5728(89)90115-X

Jack, C. R. (2011, 2011/12/01/). Alliance for Aging Research AD Biomarkers Work Group: structural MRI. *Neurobiology of Aging, 32*, S48-S57. https://doi.org/https://doi.org/10.1016/j.neurobiolaging.2011.09.011

Jack, C. R., Jr., Barnes, J., Bernstein, M. A., Borowski, B. J., Brewer, J., Clegg, S., Dale, A. M., Carmichael, O., Ching, C., DeCarli, C., Desikan, R. S., Fennema-Notestine, C., Fjell, A. M., Fletcher, E., Fox, N. C., Gunter, J., Gutman, B. A., Holland, D., Hua, X., Insel, P., Kantarci, K., Killiany, R. J., Krueger, G., Leung, K. K., Mackin, S., Maillard, P., Malone, I. B., Mattsson, N., McEvoy, L., Modat, M., Mueller, S., Nosheny, R., Ourselin, S., Schuff, N., Senjem, M. L., Simonson, A., Thompson, P. M., Rettmann, D., Vemuri, P., Walhovd, K., Zhao, Y., Zuk, S., & Weiner, M. (2015, Jul). Magnetic resonance imaging in Alzheimer's Disease Neuroimaging Initiative 2. *Alzheimers Dement, 11*(7), 740-756. https://doi.org/10.1016/j.jalz.2015.05.002

Jack, C. R., Jr., Bennett, D. A., Blennow, K., Carrillo, M. C., Dunn, B., Haeberlein, S. B., Holtzman, D. M., Jagust, W., Jessen, F., Karlawish, J., Liu, E., Molinuevo, J. L., Montine, T., Phelps, C., Rankin, K. P., Rowe, C. C., Scheltens, P., Siemers, E., Snyder, H. M., Sperling, R., & Contributors. (2018, Apr). NIA-AA Research Framework: Toward a biological definition of Alzheimer's disease. *Alzheimers Dement, 14*(4), 535-562. https://doi.org/10.1016/j.jalz.2018.02.018

Jack, C. R., Jr., Knopman, D. S., Jagust, W. J., Shaw, L. M., Aisen, P. S., Weiner, M. W., Petersen, R. C., & Trojanowski, J. Q. (2010). Hypothetical model of dynamic biomarkers of the Alzheimer's pathological cascade. *The Lancet. Neurology, 9*(1), 119-128. https://doi.org/10.1016/S1474-4422(09)70299-6

Jack, C. R., Jr., Petersen, R. C., Xu, Y. C., Waring, S. C., O'Brien, P. C., Tangalos, E. G., Smith, G. E., Ivnik, R. J., & Kokmen, E. (1997, Sep). Medial temporal atrophy on MRI in normal aging and very mild Alzheimer's disease. *Neurology, 49*(3), 786-794. https://doi.org/10.1212/wnl.49.3.786

Jenkinson, M., Beckmann, C. F., Behrens, T. E., Woolrich, M. W., & Smith, S. M. (2012, Aug 15). Fsl. *Neuroimage, 62*(2), 782-790. https://doi.org/10.1016/j.neuroimage.2011.09.015

Jezzard, P., & Balaban, R. S. (1995, Jul). Correction for geometric distortion in echo planar images from B0 field variations. *Magn Reson Med, 34*(1), 65-73. https://doi.org/10.1002/mrm.1910340111

Jill L. Kays, Psy.D. ,, Robin A. Hurley, M.D. , and, & Katherine H. Taber, Ph.D. (2012). The Dynamic Brain: Neuroplasticity and Mental Health. *The Journal of Neuropsychiatry and Clinical Neurosciences, 24*(2), 118-124. https://doi.org/10.1176/appi.neuropsych.12050109

Jo, Y., Kim, J., Park, C. H., Lee, J. W., Hur, J. H., Yang, D. H., Lee, B. Y., Im, D. J., Hong, S. J., Kim, E. Y., Park, E.-A., Kim, P. K., & Yong, H. S. (2019, 9/). Guideline for Cardiovascular Magnetic Resonance Imaging from the Korean Society of Cardiovascular Imaging—Part 1: Standardized Protocol. *Korean J Radiol, 20*(9), 1313-1333. https://doi.org/10.3348/kjr.2019.0398

Jozsvai, E., Hewitt, S., & Gedye, A. (2018). Gedye Dementia Scale for Down Syndrome. In V. P. Prasher (Ed.), *Neuropsychological Assessments of Dementia in Down Syndrome and Intellectual Disabilities* (pp. 57-71). Springer International Publishing. https://doi.org/10.1007/978-3-319-61720-6_4

Kaas, J. H., & Stepniewska, I. (2002). Motor Cortex. In V. S. Ramachandran (Ed.), *Encyclopedia of the Human Brain* (pp. 159-169). Academic Press. https://doi.org/https://doi.org/10.1016/B0-12-227210-2/00217-X

Kanda, H., Ling, J., Tonomura, S., Noguchi, K., Matalon, S., & Gu, J. G. (2019, 2019/12/04/). TREK-1 and TRAAK Are Principal K+ Channels at the Nodes of Ranvier for Rapid Action Potential Conduction on Mammalian Myelinated Afferent Nerves. *Neuron, 104*(5), 960-971.e967. https://doi.org/https://doi.org/10.1016/j.neuron.2019.08.042

Kantarci, K., Murray, M. E., Schwarz, C. G., Reid, R. I., Przybelski, S. A., Lesnick, T., Zuk, S. M., Raman, M. R., Senjem, M. L., Gunter, J. L., Boeve, B. F., Knopman, D. S., Parisi, J. E., Petersen, R. C., Jack, C. R., & Dickson, D. W. (2017, 2017/08/01/). White-matter integrity on DTI and the pathologic staging of Alzheimer's disease. *Neurobiology of Aging, 56*, 172-179. https://doi.org/https://doi.org/10.1016/j.neurobiolaging.2017.04.024

Kecskemeti, S., Samsonov, A., Hurley, S. A., Dean, D. C., Field, A., & Alexander, A. L. (2016, Mar). MPnRAGE: A technique to simultaneously acquire hundreds of differently contrasted MPRAGE images with applications to quantitative T1 mapping. *Magn Reson Med, 75*(3), 1040-1053. https://doi.org/10.1002/mrm.25674

Kecskemeti, S., Samsonov, A., Velikina, J., Field, A. S., Turski, P., Rowley, H., Lainhart, J. E., & Alexander, A. L. (2018, Nov). Robust Motion Correction Strategy for Structural MRI in Unsedated Children Demonstrated with Three-dimensional Radial MPnRAGE. *Radiology, 289*(2), 509-516. https://doi.org/10.1148/radiol.2018180180

Keller, T. A., & Just, M. A. (2016, Jan 15). Structural and functional neuroplasticity in human learning of spatial routes. *Neuroimage, 125*, 256-266. https://doi.org/10.1016/j.neuroimage.2015.10.015

Kellner, E., Dhital, B., Kiselev, V. G., & Reisert, M. (2016, Nov). Gibbs-ringing artifact removal based on local subvoxel-shifts. *Magn Reson Med, 76*(5), 1574-1581. https://doi.org/10.1002/mrm.26054

Kerbler, G. M., Fripp, J., Rowe, C. C., Villemagne, V. L., Salvado, O., Rose, S., & Coulson, E. J. (2015). Basal forebrain atrophy correlates with amyloid β burden in Alzheimer's disease. *Neuroimage Clin, 7*, 105-113. https://doi.org/10.1016/j.nicl.2014.11.015

Kingsley, P. B. (2006). Introduction to diffusion tensor imaging mathematics: Part III. Tensor calculation, noise, simulations, and optimization. *Concepts in Magnetic Resonance Part A, 28A*(2), 155-179. https://doi.org/https://doi.org/10.1002/cmr.a.20050

Kishore, P., Usha Kumari, C., Kumar, M. N. V. S. S., & Pavani, T. (2020, 2020/09/10/). Detection and analysis of Alzheimer's disease using various machine learning algorithms. *Materials Today: Proceedings*. https://doi.org/https://doi.org/10.1016/j.matpr.2020.07.645

Klunk, W. E., Engler, H., Nordberg, A., Wang, Y., Blomqvist, G., Holt, D. P., Bergstrom, M., Savitcheva, I., Huang, G. F., Estrada, S., Ausen, B., Debnath, M. L., Barletta, J., Price, J. C., Sandell, J., Lopresti, B. J., Wall, A., Koivisto, P., Antoni, G., Mathis, C. A., & Langstrom, B. (2004, Mar). Imaging brain amyloid in Alzheimer's disease with Pittsburgh Compound-B. *Ann Neurol, 55*(3), 306-319. https://doi.org/10.1002/ana.20009

Korkman, M., Kirk, U., & Kemp, S. (2007). *NEPSY II: Clinical and interpretive manual*. Harcourt Assessment, PsychCorp.

Kühn, S., Gleich, T., Lorenz, R. C., Lindenberger, U., & Gallinat, J. (2014, 2014/02/01). Playing Super Mario induces structural brain plasticity: gray matter changes resulting from training with a commercial video game. *Molecular Psychiatry, 19*(2), 265-271. https://doi.org/10.1038/mp.2013.120

Lao, P. J., Betthauser, T. J., Hillmer, A. T., Price, J. C., Klunk, W. E., Mihaila, I., Higgins, A. T., Bulova, P. D., Hartley, S. L., Hardison, R., Tumuluru, R. V., Murali, D., Mathis, C. A., Cohen, A. D., Barnhart, T. E., Devenny, D. A., Mailick, M. R., Johnson, S. C., Handen, B. L., & Christian, B. T. (2016, Apr). The effects of normal aging on amyloid-beta deposition in nondemented adults with Down syndrome as imaged by carbon 11-labeled Pittsburgh compound B. *Alzheimers Dement, 12*(4), 380-390. https://doi.org/10.1016/j.jalz.2015.05.013

Lao, P. J., Handen, B. L., Betthauser, T. J., Cody, K. A., Cohen, A. D., Tudorascu, D. L., Stone, C. K., Price, J. C., Johnson, S. C., Klunk, W. E., & Christian, B. T. (2019, 2019/04/01). Imaging neurodegeneration in Down syndrome: brain templates for amyloid burden and tissue segmentation. *Brain Imaging and Behavior, 13*(2), 345-353. https://doi.org/10.1007/s11682-018-9888-y

Lao, P. J., Handen, B. L., Betthauser, T. J., Mihaila, I., Hartley, S. L., Cohen, A. D., Tudorascu, D. L., Bulova, P. D., Lopresti, B. J., Tumuluru, R. V., Murali, D., Mathis, C. A., Barnhart,

T. E., Stone, C. K., Price, J. C., Devenny, D. A., Johnson, S. C., Klunk, W. E., & Christian, B. T. (2018). Alzheimer-Like Pattern of Hypometabolism Emerges with Elevated Amyloid-beta Burden in Down Syndrome. *J Alzheimers Dis, 61*(2), 631-644. https://doi.org/10.3233/JAD-170720

Lazari, A., & Lipp, I. (2021, 2021/04/15/). Can MRI measure myelin? Systematic review, qualitative assessment, and meta-analysis of studies validating microstructural imaging with myelin histology. *Neuroimage, 230*, 117744. https://doi.org/https://doi.org/10.1016/j.neuroimage.2021.117744

Lehéricy, S., Baulac, M., Chiras, J., Piérot, L., Martin, N., Pillon, B., Deweer, B., Dubois, B., & Marsault, C. (1994, May). Amygdalohippocampal MR volume measurements in the early stages of Alzheimer disease. *AJNR Am J Neuroradiol, 15*(5), 929-937.

Leys, D., Soetaert, G., Petit, H., Fauquette, A., Pruvo, J.-P., & Steinling, M. (1990). Periventricular and white matter magnetic resonance imaging hyperintensities do not differ between Alzheimer's disease and normal aging. *Archives of Neurology, 47*(5), 524-527.

Libby, L. A., Hannula, D. E., & Ranganath, C. (2014). Medial temporal lobe coding of item and spatial information during relational binding in working memory. *The Journal of neuroscience : the official journal of the Society for Neuroscience, 34*(43), 14233-14242. https://doi.org/10.1523/JNEUROSCI.0655-14.2014

Lockhart, S. N., Mayda, A. B., Roach, A. E., Fletcher, E., Carmichael, O., Maillard, P., Schwarz, C. G., Yonelinas, A. P., Ranganath, C., & Decarli, C. (2012). Episodic memory function is associated with multiple measures of white matter integrity in cognitive aging. *Front Hum Neurosci, 6*, 56. https://doi.org/10.3389/fnhum.2012.00056

Lopresti, B. J., Klunk, W. E., Mathis, C. A., Hoge, J. A., Ziolko, S. K., Lu, X., Meltzer, C. C., Schimmel, K., Tsopelas, N. D., DeKosky, S. T., & Price, J. C. (2005, Dec). Simplified quantification of Pittsburgh Compound B amyloid imaging PET studies: a comparative analysis. *J Nucl Med, 46*(12), 1959-1972.

Lott, I. T. (2012). Neurological phenotypes for Down syndrome across the life span. *Prog Brain Res, 197*, 101-121. https://doi.org/10.1016/B978-0-444-54299-1.00006-6

Lövdén, M., Bodammer, N. C., Kühn, S., Kaufmann, J., Schütze, H., Tempelmann, C., Heinze, H. J., Düzel, E., Schmiedek, F., & Lindenberger, U. (2010, Nov). Experience-dependent plasticity of white-matter microstructure extends into old age. *Neuropsychologia, 48*(13), 3878-3883. https://doi.org/10.1016/j.neuropsychologia.2010.08.026

Magnetic Resonance Imaging. (2014). In *Magnetic Resonance Imaging* (pp. 1-17). https://doi.org/https://doi.org/10.1002/9781118633953.ch1

Maguire, E. A., Gadian, D. G., Johnsrude, I. S., Good, C. D., Ashburner, J., Frackowiak, R. S. J., & Frith, C. D. (2000). Navigation-related structural change in the hippocampi of taxi

drivers. *Proceedings of the National Academy of Sciences, 97*(8), 4398-4403. https://doi.org/10.1073/pnas.070039597

Mah, A., Geeraert, B., & Lebel, C. (2017). Detailing neuroanatomical development in late childhood and early adolescence using NODDI. *PLoS One, 12*(8), e0182340. https://doi.org/10.1371/journal.pone.0182340

Marguet, D., Lenne, P.-F., Rigneault, H., & He, H.-T. (2006). Dynamics in the plasma membrane: how to combine fluidity and order. *The EMBO Journal, 25*(15), 3446-3457. https://doi.org/https://doi.org/10.1038/sj.emboj.7601204

Matthews, D. C., Lukic, A. S., Andrews, R. D., Marendic, B., Brewer, J., Rissman, R. A., Mosconi, L., Strother, S. C., Wernick, M. N., Mobley, W. C., Ness, S., Schmidt, M. E., & Rafii, M. S. (2016, 2016/06//). Dissociation of Down syndrome and Alzheimer's disease effects with imaging. *Alzheimer's & Dementia: Translational Research & Clinical Interventions, 2*(2), 69-81. https://doi.org/10.1016/j.trci.2016.02.004

Mayo, C. D., Garcia-Barrera, M. A., Mazerolle, E. L., Ritchie, L. J., Fisk, J. D., Gawryluk, J. R., & Alzheimer's Disease Neuroimaging, I. (2018). Relationship Between DTI Metrics and Cognitive Function in Alzheimer's Disease. *Front Aging Neurosci, 10*, 436. https://doi.org/10.3389/fnagi.2018.00436

Mayo, C. D., Mazerolle, E. L., Ritchie, L., Fisk, J. D., Gawryluk, J. R., & Alzheimer's Disease Neuroimaging, I. (2017). Longitudinal changes in microstructural white matter metrics in Alzheimer's disease. *Neuroimage Clin, 13*, 330-338. https://doi.org/10.1016/j.nicl.2016.12.012

McCarron, M., McCallion, P., Reilly, E., & Mulryan, N. (2014, Jan). A prospective 14-year longitudinal follow-up of dementia in persons with Down syndrome. *J Intellect Disabil Res, 58*(1), 61-70. https://doi.org/10.1111/jir.12074

McGeer, P., Kamo, H., Harrop, R., McGeer, E., Martin, W., Pate, B., & Li, D. (1986). Comparison of PET, MRI, and CT with pathology in a proven case of Alzheimer's disease. *Neurology, 36*(12), 1569-1569.

McGeer, P. L. (1986). Brain imaging in Alzheimer's disease. *British medical bulletin, 42*(1), 24-28.

McNamee, R. L., Yee, S.-H., Price, J. C., Klunk, W. E., Rosario, B., Weissfeld, L., Ziolko, S., Berginc, M., Lopresti, B., DeKosky, S., & Mathis, C. A. (2009, March 1, 2009). Consideration of Optimal Time Window for Pittsburgh Compound B PET Summed Uptake Measurements. *Journal of Nuclear Medicine, 50*(3), 348-355. https://doi.org/10.2967/jnumed.108.057612

Meriney, S. D., & Fanselow, E. E. (2019). Chapter 14 - Synaptic Plasticity. In S. D. Meriney & E. E. Fanselow (Eds.), *Synaptic Transmission* (pp. 287-329). Academic Press. https://doi.org/https://doi.org/10.1016/B978-0-12-815320-8.00014-4

Metzler-Baddeley, C., Jones, D. K., Belaroussi, B., Aggleton, J. P., & O'Sullivan, M. J. (2011, Sep 14). Frontotemporal connections in episodic memory and aging: a diffusion MRI tractography study. *J Neurosci, 31*(37), 13236-13245. https://doi.org/10.1523/jneurosci.2317-11.2011

Moore, E., Schaefer, R. S., Bastin, M. E., Roberts, N., & Overy, K. (2014). Can musical training influence brain connectivity? Evidence from diffusion tensor MRI. *Brain sciences, 4*(2), 405-427. https://doi.org/10.3390/brainsci4020405

Nakajima, R., Kinoshita, M., Shinohara, H., & Nakada, M. (2020, 2020/12/01). The superior longitudinal fascicle: reconsidering the fronto-parietal neural network based on anatomy and function. *Brain Imaging and Behavior, 14*(6), 2817-2830. https://doi.org/10.1007/s11682-019-00187-4

Nasrabady, S. E., Rizvi, B., Goldman, J. E., & Brickman, A. M. (2018, 2018/03/02). White matter changes in Alzheimer's disease: a focus on myelin and oligodendrocytes. *Acta Neuropathologica Communications, 6*(1), 22. https://doi.org/10.1186/s40478-018-0515-3

Neale, N., Padilla, C., Fonseca, L. M., Holland, T., & Zaman, S. (2018). Neuroimaging and other modalities to assess Alzheimer's disease in Down syndrome. *Neuroimage Clin, 17*, 263-271. https://doi.org/10.1016/j.nicl.2017.10.022

[Record #64 is using a reference type undefined in this output style.]

Nicolas, R., Hiba, B., Dilharreguy, B., Barse, E., Baillet, M., Edde, M., Pelletier, A., Periot, O., Helmer, C., Allard, M., Dartigues, J. F., Amieva, H., Pérès, K., Fernandez, P., & Catheline, G. (2020). Changes Over Time of Diffusion MRI in the White Matter of Aging Brain, a Good Predictor of Verbal Recall. *Front Aging Neurosci, 12*, 218. https://doi.org/10.3389/fnagi.2020.00218

Nir, T. M., Jahanshad, N., Villalon-Reina, J. E., Toga, A. W., Jack, C. R., Weiner, M. W., & Thompson, P. M. (2013, 2013/01/01/). Effectiveness of regional DTI measures in distinguishing Alzheimer's disease, MCI, and normal aging. *NeuroImage: Clinical, 3*, 180-195. https://doi.org/https://doi.org/10.1016/j.nicl.2013.07.006

Noguchi-Shinohara, M., Komatsu, J., Samuraki, M., Matsunari, I., Ikeda, T., Sakai, K., Hamaguchi, T., Ono, K., Nakamura, H., & Yamada, M. (2017). Cerebral Amyloid Angiopathy-Related Microbleeds and Cerebrospinal Fluid Biomarkers in Alzheimer's Disease. *J Alzheimers Dis, 55*(3), 905-913. https://doi.org/10.3233/jad-160651

Nowrangi, M. A., Lyketsos, C. G., Leoutsakos, J. M., Oishi, K., Albert, M., Mori, S., & Mielke, M. M. (2013, Sep). Longitudinal, region-specific course of diffusion tensor imaging

measures in mild cognitive impairment and Alzheimer's disease. *Alzheimers Dement, 9*(5), 519-528. https://doi.org/10.1016/j.jalz.2012.05.2186

Nowrangi, M. A., Okonkwo, O., Lyketsos, C., Oishi, K., Mori, S., Albert, M., & Mielke, M. M. (2015). Atlas-based diffusion tensor imaging correlates of executive function. *J Alzheimers Dis, 44*(2), 585-598. https://doi.org/10.3233/JAD-141937

O'Dwyer, L., Lamberton, F., Bokde, A. L., Ewers, M., Faluyi, Y. O., Tanner, C., Mazoyer, B., O'Neill, D., Bartley, M., Collins, D. R., Coughlan, T., Prvulovic, D., & Hampel, H. (2011). Multiple indices of diffusion identifies white matter damage in mild cognitive impairment and Alzheimer's disease. *PLoS One, 6*(6), e21745. https://doi.org/10.1371/journal.pone.0021745

Oishi, K., Zilles, K., Amunts, K., Faria, A., Jiang, H., Li, X., Akhter, K., Hua, K., Woods, R., Toga, A. W., Pike, G. B., Rosa-Neto, P., Evans, A., Zhang, J., Huang, H., Miller, M. I., van Zijl, P. C., Mazziotta, J., & Mori, S. (2008, Nov 15). Human brain white matter atlas: identification and assignment of common anatomical structures in superficial white matter. *Neuroimage, 43*(3), 447-457. https://doi.org/10.1016/j.neuroimage.2008.07.009

Patrick, A., Wu, M., Lao, P. J., Dean III, D. C., Zammit, M. D., Johnson, S. C., Tudorascu, D. L., Cohen, A., Cody, K. A., Laymon, C. M., Klunk, W. E., Zaman, S., Handen, B. L., Alexander, A. L., & Christian, B. T. (2019a). Amyloid- β Associations with White Matter Integrity in Down Syndrome Assessed Using Diffusion Tensor Imaging and 11C-PiB Positron Emission Tomography. ISMRM 27th Annual Meeting, Montreal, QC, Canada.

Patrick, A., Wu, M., Lao, P. J., Dean III, D. C., Zammit, M. D., Johnson, S. C., Tudorascu, D. L., Cohen, A., Cody, K. A., Laymon, C. M., Klunk, W. E., Zaman, S., Handen, B. L., Alexander, A. L., & Christian, B. T. (2019b). P3-325: AMYLOID- β ASSOCIATIONS WITH WHITE MATTER IN DOWN SYNDROME ASSESSED USING TRACT-BASED SPATIAL STATISTICS (TBSS) AND 11C-PIB POSITRON EMISSION TOMOGRAPHY. *Alzheimer's & Dementia, 15*(7S_Part_20), P1063-P1063. https://doi.org/https://doi.org/10.1016/j.jalz.2019.06.3357

Phillips, B. A., Loveall, S. J., Channell, M. M., & Conners, F. A. (2014, Feb). Matching variables for research involving youth with Down syndrome: Leiter-R versus PPVT-4. *Res Dev Disabil, 35*(2), 429-438. https://doi.org/10.1016/j.ridd.2013.11.016

Pierpaoli, C., & Basser, P. J. (1996, Dec). Toward a quantitative assessment of diffusion anisotropy. *Magn Reson Med, 36*(6), 893-906. https://doi.org/10.1002/mrm.1910360612

Popkin, B. M., D'Anci, K. E., & Rosenberg, I. H. (2010). Water, hydration, and health. *Nutrition reviews, 68*(8), 439-458. https://doi.org/10.1111/j.1753-4887.2010.00304.x

Powell, D., Caban-Holt, A., Jicha, G., Robertson, W., Davis, R., Gold, B. T., Schmitt, F. A., & Head, E. (2014, Jul). Frontal white matter integrity in adults with Down syndrome with

and without dementia. *Neurobiol Aging, 35*(7), 1562-1569. https://doi.org/10.1016/j.neurobiolaging.2014.01.137

Price, J. C., Klunk, W. E., Lopresti, B. J., Lu, X., Hoge, J. A., Ziolko, S. K., Holt, D. P., Meltzer, C. C., DeKosky, S. T., & Mathis, C. A. (2005, Nov). Kinetic modeling of amyloid binding in humans using PET imaging and Pittsburgh Compound-B. *J Cereb Blood Flow Metab, 25*(11), 1528-1547. https://doi.org/10.1038/sj.jcbfm.9600146

Prince, M., Bryce, R., Albanese, E., Wimo, A., Ribeiro, W., & Ferri, C. P. (2013, Jan). The global prevalence of dementia: a systematic review and metaanalysis. *Alzheimers Dement, 9*(1), 63-75.e62. https://doi.org/10.1016/j.jalz.2012.11.007

Provenzale, J. M., Isaacson, J., Chen, S., Stinnett, S., & Liu, C. (2010, Dec). Correlation of apparent diffusion coefficient and fractional anisotropy values in the developing infant brain. *AJR Am J Roentgenol, 195*(6), W456-462. https://doi.org/10.2214/ajr.10.4886

Qi, X., & Arfanakis, K. (2021, Jan 15). Regionconnect: Rapidly extracting standardized brain connectivity information in voxel-wise neuroimaging studies. *Neuroimage, 225*, 117462. https://doi.org/10.1016/j.neuroimage.2020.117462

Qiu, C., Kivipelto, M., & von Strauss, E. (2009). Epidemiology of Alzheimer's disease: occurrence, determinants, and strategies toward intervention. *Dialogues in clinical neuroscience, 11*(2), 111-128. https://doi.org/10.31887/DCNS.2009.11.2/cqiu

Racine, A. M., Adluru, N., Alexander, A. L., Christian, B. T., Okonkwo, O. C., Oh, J., Cleary, C. A., Birdsill, A., Hillmer, A. T., Murali, D., Barnhart, T. E., Gallagher, C. L., Carlsson, C. M., Rowley, H. A., Dowling, N. M., Asthana, S., Sager, M. A., Bendlin, B. B., & Johnson, S. C. (2014). Associations between white matter microstructure and amyloid burden in preclinical Alzheimer's disease: A multimodal imaging investigation. *Neuroimage Clin, 4*, 604-614. https://doi.org/10.1016/j.nicl.2014.02.001

Rafii, M. S., Wishnek, H., Brewer, J. B., Donohue, M. C., Ness, S., Mobley, W. C., Aisen, P. S., & Rissman, R. A. (2015). The down syndrome biomarker initiative (DSBI) pilot: proof of concept for deep phenotyping of Alzheimer's disease biomarkers in down syndrome. *Front Behav Neurosci, 9*, 239. https://doi.org/10.3389/fnbeh.2015.00239

Ramos-Fresnedo, A., Segura-Duran, I., Chaichana, K. L., & Pillai, J. J. (2019). Chapter 2 - Supratentorial White Matter Tracts. In K. Chaichana & A. Quiñones-Hinojosa (Eds.), *Comprehensive Overview of Modern Surgical Approaches to Intrinsic Brain Tumors* (pp. 23-35). Academic Press. https://doi.org/https://doi.org/10.1016/B978-0-12-811783-5.00002-1

Razek, A., Taman, S. E., El Regal, M. E., Megahed, A., Elzeny, S., & El Tantawi, N. (2020, May/Jun). Diffusion Tensor Imaging of Microstructural Changes in the Gray and White Matter in Patients With Crigler-Najjar Syndrome Type I. *J Comput Assist Tomogr, 44*(3), 393-398. https://doi.org/10.1097/rct.0000000000001008

Reeder, S. B., Atalar, E., Bolster, B. D., Jr., & McVeigh, E. R. (1997, Sep). Quantification and reduction of ghosting artifacts in interleaved echo-planar imaging. *Magn Reson Med, 38*(3), 429-439. https://doi.org/10.1002/mrm.1910380312

Reisberg, B., Ferris, S. H., de Leon, M. J., & Crook, T. (1982). The Global Deterioration Scale for assessment of primary degenerative dementia. *The American Journal of Psychiatry, 139*(9), 1136-1139. https://doi.org/10.1176/ajp.139.9.1136

Reivich, M., Kuhl, D., Wolf, A., Greenberg, J., Phelps, M., Ido, T., Casella, V., Fowler, J., Hoffman, E., Alavi, A., Som, P., & Sokoloff, L. (1979, Jan). The [18F]fluorodeoxyglucose method for the measurement of local cerebral glucose utilization in man. *Circ Res, 44*(1), 127-137. https://doi.org/10.1161/01.res.44.1.127

Rémy, F., Vayssière, N., Saint-Aubert, L., Barbeau, E., & Pariente, J. (2015). White matter disruption at the prodromal stage of Alzheimer's disease: relationships with hippocampal atrophy and episodic memory performance. *Neuroimage Clin, 7*, 482-492. https://doi.org/10.1016/j.nicl.2015.01.014

Romano, A., Moraschi, M., Cornia, R., Bozzao, A., Rossi-Espagnet, M. C., Giove, F., Albertini, G., & Pierallini, A. (2018, Dec). White matter involvement in young non-demented Down's syndrome subjects: a tract-based spatial statistic analysis. *Neuroradiology, 60*(12), 1335-1341. https://doi.org/10.1007/s00234-018-2102-5

Rose, S. E., Chen, F., Chalk, J. B., Zelaya, F. O., Strugnell, W. E., Benson, M., Semple, J., & Doddrell, D. M. (2000). Loss of connectivity in Alzheimer's disease: an evaluation of white matter tract integrity with colour coded MR diffusion tensor imaging. *Journal of Neurology, Neurosurgery & Psychiatry, 69*(4), 528-530. https://doi.org/10.1136/jnnp.69.4.528

Rubenstein, E., Hartley, S., & Bishop, L. (2020). Epidemiology of Dementia and Alzheimer Disease in Individuals With Down Syndrome. *JAMA Neurology, 77*(2), 262-264. https://doi.org/10.1001/jamaneurol.2019.3666

Sabri, O., Sabbagh, M. N., Seibyl, J., Barthel, H., Akatsu, H., Ouchi, Y., Senda, K., Murayama, S., Ishii, K., Takao, M., Beach, T. G., Rowe, C. C., Leverenz, J. B., Ghetti, B., Ironside, J. W., Catafau, A. M., Stephens, A. W., Mueller, A., Koglin, N., Hoffmann, A., Roth, K., Reininger, C., & Schulz-Schaeffer, W. J. (2015, Aug). Florbetaben PET imaging to detect amyloid beta plaques in Alzheimer's disease: phase 3 study. *Alzheimers Dement, 11*(8), 964-974. https://doi.org/10.1016/j.jalz.2015.02.004

Sagi, Y., Tavor, I., Hofstetter, S., Tzur-Moryosef, S., Blumenfeld-Katzir, T., & Assaf, Y. (2012, Mar 22). Learning in the fast lane: new insights into neuroplasticity. *Neuron, 73*(6), 1195-1203. https://doi.org/10.1016/j.neuron.2012.01.025

Sampaio-Baptista, C., Khrapitchev, A. A., Foxley, S., Schlagheck, T., Scholz, J., Jbabdi, S., DeLuca, G. C., Miller, K. L., Taylor, A., Thomas, N., Kleim, J., Sibson, N. R., Bannerman, D., & Johansen-Berg, H. (2013). Motor Skill Learning Induces Changes in White Matter Microstructure and Myelination. *The Journal of Neuroscience, 33*(50), 19499-19503. https://doi.org/10.1523/jneurosci.3048-13.2013

Sayres, R., & Grill-Spector, K. (2008). Relating Retinotopic and Object-Selective Responses in Human Lateral Occipital Cortex. *Journal of Neurophysiology, 100*(1), 249-267. https://doi.org/10.1152/jn.01383.2007

Scahill, R. I., Schott, J. M., Stevens, J. M., Rossor, M. N., & Fox, N. C. (2002). Mapping the evolution of regional atrophy in Alzheimer's disease: unbiased analysis of fluid-registered serial MRI. *Proceedings of the National Academy of Sciences of the United States of America, 99*(7), 4703-4707. https://doi.org/10.1073/pnas.052587399

Schiller, D., Eichenbaum, H., Buffalo, E. A., Davachi, L., Foster, D. J., Leutgeb, S., & Ranganath, C. (2015). Memory and Space: Towards an Understanding of the Cognitive Map. *The Journal of Neuroscience, 35*(41), 13904-13911. https://doi.org/10.1523/jneurosci.2618-15.2015

Scholz, J., Klein, M. C., Behrens, T. E. J., & Johansen-Berg, H. (2009). Training induces changes in white-matter architecture. *Nature neuroscience, 12*(11), 1370-1371. https://doi.org/10.1038/nn.2412

Siracusa, R., Fusco, R., & Cuzzocrea, S. (2019, 2019-September-27). Astrocytes: Role and Functions in Brain Pathologies [Mini Review]. *Frontiers in Pharmacology, 10*(1114). https://doi.org/10.3389/fphar.2019.01114

Smith, S. M. (2002, Nov). Fast robust automated brain extraction. *Hum Brain Mapp, 17*(3), 143-155. https://doi.org/10.1002/hbm.10062

Smith, S. M., Jenkinson, M., Johansen-Berg, H., Rueckert, D., Nichols, T. E., Mackay, C. E., Watkins, K. E., Ciccarelli, O., Cader, M. Z., Matthews, P. M., & Behrens, T. E. (2006, Jul 15). Tract-based spatial statistics: voxelwise analysis of multi-subject diffusion data. *Neuroimage, 31*(4), 1487-1505. https://doi.org/10.1016/j.neuroimage.2006.02.024

Smith, S. M., Jenkinson, M., Woolrich, M. W., Beckmann, C. F., Behrens, T. E., Johansen-Berg, H., Bannister, P. R., De Luca, M., Drobnjak, I., Flitney, D. E., Niazy, R. K., Saunders, J., Vickers, J., Zhang, Y., De Stefano, N., Brady, J. M., & Matthews, P. M. (2004). Advances in functional and structural MR image analysis and implementation as FSL. *Neuroimage, 23 Suppl 1*, S208-219. https://doi.org/10.1016/j.neuroimage.2004.07.051

Smith, S. M., & Nichols, T. E. (2009, Jan 1). Threshold-free cluster enhancement: addressing problems of smoothing, threshold dependence and localisation in cluster inference. *Neuroimage, 44*(1), 83-98. https://doi.org/10.1016/j.neuroimage.2008.03.061

Sokolowski, J. D., & Mandell, J. W. (2011, Apr). Phagocytic clearance in neurodegeneration. *Am J Pathol, 178*(4), 1416-1428. https://doi.org/10.1016/j.ajpath.2010.12.051

Sparrow, S. S., Balla, D. A., Cicchetti, D. V., & Harrison, P. L. (1984). Vineland adaptive behavior scales.

Spees, W. M., Buhl, N., Sun, P., Ackerman, J. J., Neil, J. J., & Garbow, J. R. (2011, Sep). Quantification and compensation of eddy-current-induced magnetic-field gradients. *Journal of magnetic resonance (San Diego, Calif. : 1997), 212*(1), 116-123. https://doi.org/10.1016/j.jmr.2011.06.016

Stejskal, E. O., & Tanner, J. E. (1965, 1965/01/01). Spin Diffusion Measurements: Spin Echoes in the Presence of a Time-Dependent Field Gradient. *The Journal of Chemical Physics, 42*(1), 288-292. https://doi.org/10.1063/1.1695690

Takeuchi, H., Taki, Y., Nouchi, R., Hashizume, H., Sekiguchi, A., Kotozaki, Y., Nakagawa, S., Miyauchi, C. M., Sassa, Y., & Kawashima, R. (2015, 2015/11/01). Working memory training impacts the mean diffusivity in the dopaminergic system. *Brain Structure and Function, 220*(6), 3101-3111. https://doi.org/10.1007/s00429-014-0845-2

Tanaka, S., & Kirino, E. (2019, 2019-March-18). Increased Functional Connectivity of the Angular Gyrus During Imagined Music Performance [Original Research]. *Frontiers in Human Neuroscience, 13*(92). https://doi.org/10.3389/fnhum.2019.00092

Taubert, M., Draganski, B., Anwander, A., Müller, K., Horstmann, A., Villringer, A., & Ragert, P. (2010). Dynamic Properties of Human Brain Structure: Learning-Related Changes in Cortical Areas and Associated Fiber Connections. *The Journal of Neuroscience, 30*(35), 11670-11677. https://doi.org/10.1523/jneurosci.2567-10.2010

Tavor, I., Hofstetter, S., & Assaf, Y. (2013, Nov 1). Micro-structural assessment of short term plasticity dynamics. *Neuroimage, 81*, 1-7. https://doi.org/10.1016/j.neuroimage.2013.05.050

Teipel, S., Heinsen, H., Amaro, E., Jr., Grinberg, L. T., Krause, B., & Grothe, M. (2014, Mar). Cholinergic basal forebrain atrophy predicts amyloid burden in Alzheimer's disease. *Neurobiol Aging, 35*(3), 482-491. https://doi.org/10.1016/j.neurobiolaging.2013.09.029

Thal, D. R., Rub, U., Orantes, M., & Braak, H. (2002, Jun 25). Phases of A beta-deposition in the human brain and its relevance for the development of AD. *Neurology, 58*(12), 1791-1800. https://doi.org/10.1212/wnl.58.12.1791

Tokoro, K., Sato, H., Yamamoto, M., & Nagai, Y. (2015, Dec). [Thalamus and Attention]. *Brain Nerve, 67*(12), 1471-1480. https://doi.org/10.11477/mf.1416200324

Tournier, J. D., Smith, R., Raffelt, D., Tabbara, R., Dhollander, T., Pietsch, M., Christiaens, D., Jeurissen, B., Yeh, C. H., & Connelly, A. (2019, Nov 15). MRtrix3: A fast, flexible and

open software framework for medical image processing and visualisation. *Neuroimage, 202*, 116137. https://doi.org/10.1016/j.neuroimage.2019.116137

United Nations, N. Y., Ny. Department of Economic, & Affairs, S. (2002). *World population ageing, 1950-2050*. United Nations Publications.

Veraart, J., Novikov, D. S., Christiaens, D., Ades-Aron, B., Sijbers, J., & Fieremans, E. (2016, Nov 15). Denoising of diffusion MRI using random matrix theory. *Neuroimage, 142*, 394-406. https://doi.org/10.1016/j.neuroimage.2016.08.016

Vlassenko, A. G., Benzinger, T. L., & Morris, J. C. (2012, Mar). PET amyloid-beta imaging in preclinical Alzheimer's disease. *Biochim Biophys Acta, 1822*(3), 370-379. https://doi.org/10.1016/j.bbadis.2011.11.005

Von Der Heide, R. J., Skipper, L. M., Klobusicky, E., & Olson, I. R. (2013). Dissecting the uncinate fasciculus: disorders, controversies and a hypothesis. *Brain : a journal of neurology, 136*(Pt 6), 1692-1707. https://doi.org/10.1093/brain/awt094

Voss, P., Thomas, M. E., Cisneros-Franco, J. M., & de Villers-Sidani, É. (2017). Dynamic Brains and the Changing Rules of Neuroplasticity: Implications for Learning and Recovery. *Frontiers in psychology, 8*, 1657-1657. https://doi.org/10.3389/fpsyg.2017.01657

Wagner, M., Wolf, S., Reischies, F. M., Daerr, M., Wolfsgruber, S., Jessen, F., Popp, J., Maier, W., Hüll, M., Frölich, L., Hampel, H., Perneczky, R., Peters, O., Jahn, H., Luckhaus, C., Gertz, H. J., Schröder, J., Pantel, J., Lewczuk, P., Kornhuber, J., & Wiltfang, J. (2012, Feb 7). Biomarker validation of a cued recall memory deficit in prodromal Alzheimer disease. *Neurology, 78*(6), 379-386. https://doi.org/10.1212/WNL.0b013e318245f447

Wang, W.-Y., Tan, M.-S., Yu, J.-T., & Tan, L. (2015). Role of pro-inflammatory cytokines released from microglia in Alzheimer's disease. *Annals of translational medicine, 3*(10), 136-136. https://doi.org/10.3978/j.issn.2305-5839.2015.03.49

Wang, X., Casadio, M., Weber, K. A., 2nd, Mussa-Ivaldi, F. A., & Parrish, T. B. (2014, Mar). White matter microstructure changes induced by motor skill learning utilizing a body machine interface. *Neuroimage, 88*, 32-40. https://doi.org/10.1016/j.neuroimage.2013.10.066

Wechsler, D. (1945). Wechsler memory scale.

Weiner, M. W., Veitch, D. P., Aisen, P. S., Beckett, L. A., Cairns, N. J., Green, R. C., Harvey, D., Jack, C. R., Jr., Jagust, W., Morris, J. C., Petersen, R. C., Salazar, J., Saykin, A. J., Shaw, L. M., Toga, A. W., & Trojanowski, J. Q. (2017, May). The Alzheimer's Disease Neuroimaging Initiative 3: Continued innovation for clinical trial improvement. *Alzheimers Dement, 13*(5), 561-571. https://doi.org/10.1016/j.jalz.2016.10.006

Winkler, A. M., Ridgway, G. R., Webster, M. A., Smith, S. M., & Nichols, T. E. (2014, 2014/05/15/). Permutation inference for the general linear model. *Neuroimage, 92*, 381-397. https://doi.org/https://doi.org/10.1016/j.neuroimage.2014.01.060

Wiseman, F. K., Al-Janabi, T., Hardy, J., Karmiloff-Smith, A., Nizetic, D., Tybulewicz, V. L. J., Fisher, E. M. C., & Strydom, A. (2015, 2015/09/01). A genetic cause of Alzheimer disease: mechanistic insights from Down syndrome. *Nature Reviews Neuroscience, 16*(9), 564-574. https://doi.org/10.1038/nrn3983

Wolf, D., Fischer, F. U., Scheurich, A., Fellgiebel, A., & Alzheimer's Disease Neuroimaging, I. (2015). Non-Linear Association between Cerebral Amyloid Deposition and White Matter Microstructure in Cognitively Healthy Older Adults. *J Alzheimers Dis, 47*(1), 117-127. https://doi.org/10.3233/JAD-150049

Wong, D. F., Rosenberg, P. B., Zhou, Y., Kumar, A., Raymont, V., Ravert, H. T., Dannals, R. F., Nandi, A., Brasić, J. R., Ye, W., Hilton, J., Lyketsos, C., Kung, H. F., Joshi, A. D., Skovronsky, D. M., & Pontecorvo, M. J. (2010, Jun). In vivo imaging of amyloid deposition in Alzheimer disease using the radioligand 18F-AV-45 (florbetapir [corrected] F 18). *J Nucl Med, 51*(6), 913-920. https://doi.org/10.2967/jnumed.109.069088

Woods, R. P., Grafton, S. T., Holmes, C. J., Cherry, S. R., & Mazziotta, J. C. (1998). Automated Image Registration: I. General Methods and Intrasubject, Intramodality Validation. *Journal of Computer Assisted Tomography, 22*(1), 139-152. https://journals.lww.com/jcat/Fulltext/1998/01000/Automated_Image_Registration__I__General_Methods.27.aspx

Wu, Y., Dissing-Olesen, L., MacVicar, B. A., & Stevens, B. (2015). Microglia: Dynamic Mediators of Synapse Development and Plasticity. *Trends in immunology, 36*(10), 605-613. https://doi.org/10.1016/j.it.2015.08.008

Wyman, B. T., Harvey, D. J., Crawford, K., Bernstein, M. A., Carmichael, O., Cole, P. E., Crane, P. K., DeCarli, C., Fox, N. C., Gunter, J. L., Hill, D., Killiany, R. J., Pachai, C., Schwarz, A. J., Schuff, N., Senjem, M. L., Suhy, J., Thompson, P. M., Weiner, M., & Jack, C. R., Jr. (2013, May). Standardization of analysis sets for reporting results from ADNI MRI data. *Alzheimers Dement, 9*(3), 332-337. https://doi.org/10.1016/j.jalz.2012.06.004

Young, A. L., Oxtoby, N. P., Daga, P., Cash, D. M., Fox, N. C., Ourselin, S., Schott, J. M., & Alexander, D. C. (2014, Sep). A data-driven model of biomarker changes in sporadic Alzheimer's disease. *Brain, 137*(Pt 9), 2564-2577. https://doi.org/10.1093/brain/awu176

Zammit, M. D., Laymon, C. M., Betthauser, T. J., Cody, K. A., Tudorascu, D. L., Minhas, D. S., Sabbagh, M. N., Johnson, S. C., Zaman, S. H., Mathis, C. A., Klunk, W. E., Handen, B. L., Cohen, A. D., & Christian, B. T. (2020). Amyloid accumulation in Down syndrome measured with amyloid load. *Alzheimers Dement (Amst), 12*(1), e12020. https://doi.org/10.1002/dad2.12020

Zammit, M. D., Laymon, C. M., Tudorascu, D. L., Hartley, S. L., Piro-Gambetti, B., Johnson, S. C., Stone, C. K., Mathis, C. A., Zaman, S. H., Klunk, W. E., Handen, B. L., Cohen, A. D., & Christian, B. T. (2020). Patterns of glucose hypometabolism in Down syndrome resemble sporadic Alzheimer's disease except for the putamen. *Alzheimer's & Dementia: Diagnosis, Assessment & Disease Monitoring*, *12*(1), e12138. https://doi.org/https://doi.org/10.1002/dad2.12138

Zhang, H., Ma, Q., Zhang, Y. W., & Xu, H. (2012, Jan). Proteolytic processing of Alzheimer's beta-amyloid precursor protein. *J Neurochem*, *120 Suppl 1*, 9-21. https://doi.org/10.1111/j.1471-4159.2011.07519.x

Zhang, H., Schneider, T., Wheeler-Kingshott, C. A., & Alexander, D. C. (2012, Jul 16). NODDI: practical in vivo neurite orientation dispersion and density imaging of the human brain. *Neuroimage*, *61*(4), 1000-1016. https://doi.org/10.1016/j.neuroimage.2012.03.072

Zhang, J., Zhang, N., Du, S., He, H., Xu, Y., Cai, H., Guo, X., & Ma, G. (2018). The Effects of Hydration Status on Cognitive Performances among Young Adults in Hebei, China: A Randomized Controlled Trial (RCT). *International journal of environmental research and public health*, *15*(7), 1477. https://doi.org/10.3390/ijerph15071477

Zhang, S., & Arfanakis, K. (2018, May 15). Evaluation of standardized and study-specific diffusion tensor imaging templates of the adult human brain: Template characteristics, spatial normalization accuracy, and detection of small inter-group FA differences. *Neuroimage*, *172*, 40-50. https://doi.org/10.1016/j.neuroimage.2018.01.046

Zhang, T., Chen, D., & Lee, T. H. (2020). Phosphorylation Signaling in APP Processing in Alzheimer's Disease. *International Journal of Molecular Sciences*, *21*(1), 209. https://www.mdpi.com/1422-0067/21/1/209

Zigman, W. B., Devenny, D. A., Krinsky-McHale, S. J., Jenkins, E. C., Urv, T. K., Wegiel, J., Schupf, N., & Silverman, W. (2008). Chapter 4 Alzheimer's Disease in Adults with Down Syndrome. In *International Review of Research in Mental Retardation* (Vol. 36, pp. 103-145). Academic Press. https://doi.org/https://doi.org/10.1016/S0074-7750(08)00004-9